جامعة الجوف
Jouf University

ISSN: 1658 - 6670
Open Access Journal
Electronic ISSN:1658-9173
(1443/5074)

Jouf University Science and Engineering Journal

(JUSEJ)

Peer-Reviewed International Journal

No. 02

Vol. 10 http://vrgs.ju.edu.sa/jer.aspx Dec. 2023

https://www.ju.edu.sa/en/jouf-university-science-and-engineering-journal-jusej/home/

JUSEJ ISSN: 1658-6670
Electronic ISSN:1658-9173

Jouf University Science and Engineering Journal

Peer-reviewed International Journal

Vol. 10(2)
December 2023

Designed and Edited by Prof. Abdelazim M. Mebed

IN THE NAME OF ALLAH, THE MOST GRACIOUS, THE MOST MERCIFUL

Dear professional colleagues, researchers and fellow students:

We are pleased to present the second issue of Volume VIII of the Journal of Science and Engineering (JUSEJ). JUSEJ was established under the generous sponsorship of the former rector of Jouf University, Prof. Ismail Muhammad Al-Bishri, since 2014, and the continuous support of the current president of the University, Prof. Muhammad Al-Shaya. Its maturity is an outcome of the consistent support of high-performing authors, a supportive and professional dedicated reviewers, many vigorous and conscientious editorial boards and collective input from the editorial board members. Various researchers who are active in the above field have been enrolled for providing the necessary impetus for the new journal. We are quite hopeful and shall be grateful to the service that these eminent scientists shall provide to the growth of JUSEJ. We are certain that the renowned scientists and academicians both from the industry and academic institutions all over the world will be enriched by sharing their research experiences through JUSEJ. We are happy to invite you to submit your valuable research works in URP journals. We strongly believe that our journal will help to develop your own professional career.

Thanks
Editors

Editorial Board

Focus and Scope

With its vision to promote science and scientific knowledge to everybody, Jouf Science and Engineering Journal (JUSEJ) is an international peer-reviewed journal owned by Jouf University with a focused aim of promoting and publishing original high quality research papers dealing with basic and engineering science. JUSEJ publishes rigorous and original contributions in the Science disciplines of

Physics	Engineering, All Fields	Applied Biology
Chemistry	Mathematics & Statistics	Physiology
Biochemistry	Computer Science	Plant Biology
Biological Sciences	Genomics	Population Biology
Biophysics	Geology	Food & Food Technology
Petroleum & Gas	Environment	Robotics
Cell Biology	Solid State Technology	Signal Transduction
Parasitological Science	Communication & IT	Space Science
Developmental Biology	Microbiology	Energy
Genetics	Zoology	Textile Industry & Fabrics
Construction	Nanotechnology	Toxicology

The papers published in Jouf Science and Engineering Journal (JUSEJ) should present novel results and have either theoretical significance or practical utility or both. They may be presented in the form of full articles, short communications or state-of-the-art reviews.

All contributions will be rigorously reviewed to ensure both scientific quality and technical relevance. Revisions of manuscripts may thus be required.

Manuscripts must be submitted in the English language and authors must ensure that the article has not been published or submitted for publication elsewhere in any format, and that there are no ethical concerns with the contents or data collection. The authors warrant that the information submitted is not redundant and respects general guidelines of ethics in publishing. All papers are evaluated by at least two international referees, who are known scholars in their fields.

Objectives

The main objective of JUSEJ is to provide an international forum for academics, researchers, industry leaders, and policy makers to investigate and exchange novel ideas and disseminate knowledge and information covering the broad range of natural science and industrial activities. In addition, it aims to establish an effective channel of communication between policy makers, government agencies, academic and research institutions and persons concerned with basic science and its applications. It also aims to promote and coordinate developments in the fields of natural science, engineering science and other related fields. The international dimension is emphasized in order to overcome cultural and national barriers and to meet the needs of accelerating ecological and technological advances in all industries and the global society and economy.

Open Access Policy

This journal provides immediate open access to its content on the principle that making research freely available to the public supports a greater global exchange of knowledge.

All published manuscripts will be available on the Journals website **http://vrgs.ju.edu.sa/#**. We strongly believe that our journal will help to develop your own professional career. You can communicate with us at any time, throughout the publishing process.

EDITORIAL OFFICE & COMMUNICATION

Jouf Science and Engineering Journal (JUSEJ)

Jouf University, Sakaka, 2014, Aljouf, Saudi Arabia

Email: ajbse@*ju.edu.sa*

TABLE OF CONTENTS

GUIDE FOR AUTHOR

TYPES OF CONTRIBUTIONS

Original research papers and occasional reviews, short communications, letters, letters to the editor and news items. Please ensure that you indicate clearly the appropriate article type when making your submission.

BEFORE YOU BEGIN

Ethical guidelines

Confidentiality

All material submitted to Science Journal of Jouf University (SJJU), accordingly to Jouf Science, Engineering Journal (JUSEJ) remains confidential, and the Editor operates a peer review system in which the identity of the referees is protected.

Duplicate publication

Duplicate publication is the publication of the same paper or substantially similar papers in more than one journal. Authors must explain in the submission letter any prior publication of the same or a substantially similar paper, and should explain any circumstances that might lead the Editor or reviewers to believe that the paper may have been published elsewhere (for example, when the title of a submitted paper is the same as or similar to the title of a previously published article).

If work that makes up more than 10% of the manuscript submitted to JUSEJ has been published elsewhere, please provide a copy of the published article in order that the Editor can make a judgment on the amount of overlap without delay. If a member of the editorial board learns that work under consideration has previously been published in whole or in part, the Editor may return the paper without review, reject the paper, announce the duplication publicly in an editorial and/or contact the authors' employers.

Submission of manuscripts to more than one journal

Authors may not send the same manuscript to more than one journal concurrently. If this occurs, the Editor may return the paper without review, reject the paper, contact the Editor of the other journal(s) in question and/or contact the authors' employers.

Plagiarism and scientific misconduct

Plagiarism is the use of others' published and unpublished ideas or words (or other intellectual property) without due reference or permission and/or their presentation as new and original points. Plagiarism is serious scientific misconduct and will be dealt with accordingly. All papers submitted to the journal is cheched with *iThenticate* program for plagiarism. We define plagiarism as a case in which a paper reproduces another work with at least 15% similarity and without citation.

If evidence of plagiarism is found before or after acceptance or after publication of the paper, the author will be offered a chance to defend his/her paper. If the arguments are found to be unsatisfactory, the manuscript will be retracted and authors found to have been guilty of plagiarism will no longer have papers accepted for publication by JUSEJ.

iThenticate compares submitted documents to extensive data repositories to create a

comprehensive Similarity Report, which highlights and provides links to any significant text matches, helping to ensure that you are submitting an original and well-attributed document.

Data auditing

The journal reserves the right to view original figures and data and may make periodic requests to see these.

Conflict of interest

All authors are requested to disclose any actual or potential conflict of interest including any financial, personal or other relationships with other people or organizations within three years of beginning the submitted work that could inappropriately influence, or be perceived to influence, their work.

Submission declaration

Submission of an article implies that the work described has not been published previously (except in the form of an abstract or as part of a published lecture or academic thesis or as an electronic preprint, that it is not under consideration for publication elsewhere, that its publication is approved by all authors and tacitly or explicitly by the responsible authorities where the work was carried out, and that, if accepted, it will not be published elsewhere including electronically in the same form, in English or in any other language, without the written consent of the copyright-holder.

Changes in authorship

Requests to add or remove an author, or to rearrange the author names, must be sent to the Journal Manager from the corresponding author of the accepted manuscript *before the accepted manuscript is published* and must include: (a) the reason for the addition, removal, or rearrangement of the authors' names and (b) written confirmation (e-mail, fax, letter) from all authors that they agree with the addition, removal or rearrangement. In the case of addition or removal of authors, this includes confirmation from the author being added or removed. Requests that are not sent by the corresponding author will be forwarded by the Journal Manager to the corresponding author, who must follow the procedure as described above. Note that: (1) Journal Managers will inform the Journal Editors of any such requests and (2) publication of the accepted manuscript is suspended until authorship has been agreed.

Copyright

Upon acceptance of an article, authors will be asked to complete a 'Journal Publishing Agreement' An e-mail will be sent to the corresponding author confirming receipt of the manuscript together with a 'Journal Publishing Agreement'.

Subscribers may reproduce tables of contents or prepare lists of articles, including abstracts for internal circulation within their institutions. Permission of the Publisher is required for resale or distribution outside the institution and for all other derivative works, including compilations and translations.

If excerpts from other copyrighted works are included, the author(s) must obtain written permission from the copyright owners and credit the source(s) in the article.

Retained author rights

As an author you (or your employer or institution) have the right to use your articles for a wide range of scholarly purposes.

Role of the funding source

You are requested to identify who provided financial support for the conduct of the research and/or preparation of the article and to briefly describe the role of the sponsor(s), if any, in study design; in the collection, analysis and interpretation of data; in the writing of the report; and in the decision to submit the article

for publication. If the funding source(s) had no such involvement then this should be stated

Subscription

Articles are made available to subscribers as well as developing countries and patient groups

Language (usage and editing services)

Please write your text in good English (American or British usage is accepted, but not a mixture of these). If the English language is used, extra abstract in Arabic should be provided.

Submission

To submit your paper, please send your manuscripts by e-mail to the Editor (AJBSE@ju.edu.sa). You must submit the manuscript in a single electronic file. The manuscript should be edited using Microsoft (MS) Word (2003 up to 2010, with .doc or .docx extension)

Referees

Please submit, with the manuscript, the names, addresses and e-mail addresses of three potential referees. Note that the Editor retains the only one who has the right to decide whether or not the suggested reviewers are used.

PREPARATION

Use of word processing software

Manuscripts must be in an electronic format that meets the following specifications:

- Do not submit a manuscript file as a PDF file. Remove line numbering.
- The manuscript file—with tables and figures placed at the end of the file, each on a separate page—should be in Microsoft Word (2003 up to 2010, with .doc or .docx extension).
- Do not use the Microsoft Word "Styles and Formatting" or "Track Changes" features in the file.
- Tables should be in MS Word (.doc or .docx), one table to a page using hard page breaks.
- Figures (graphics of any kind) should be placed at the end of the Word document as images, one figure to a page using hard page breaks.
- Equations may be created and inserted as part of the text, or they may be submitted as images embedded within the text.

ARTICLE STRUCTURE

Manuscript Page setup

- Margins: 25.4 mm (1 in.) top, 25.4 mm (1 in.) left; adjust the settings for bottom and right margins so that the text area is not more than 165.1 mm by 228.6 mm (6.5 in. by 9 in.)
- Font (typeface): Times New Roman, no smaller than 10 points.
- Numbering: Insert page numbers at upper right of each page; insert name(s) of author(s) at upper left of each page
- Text: Single-spaced.
- Paragraphs: Indent first line 12.7 mm (0.5 in.); do not use an extra line space between paragraphs; do not indent first line after a subhead.

Subheads: All subheads should be flush with the left margin, with one line space above. Subsections should be numbered 1.1 (then 1.1.1, 1.1.2, ...), 1.2, etc. (the abstract is not included in section numbering).

FIRST-LEVEL SUBHEAD
(all capitals, boldface, on separate line)
Second-Level Subhead
(initial capitals, boldface, on separate line)
Third-Level Subhead
(initial capitals, italic, on separate line)

Fourth-Level Subhead (initial capitals, boldface, on same line as text, with extra letter space between the subhead and text)

Fifth-Level Subhead (initial capitals, italic, on same line as text, with extra letter space between the subhead and text)

• Bulleted and numbered lists: Indent first line 12.7 mm (0.5 in.); do not indent for text runovers.

Table Titles and Figure Captions:

TABLE 5 Effects of All Factors

(Insert title above the table; "Table" is all capitals; title is initial capitals; all types are boldfaced;

Extra space, but no punctuation after number; no punctuation at end of title.)

FIGURE 3 Example of results.

(Insert caption below the figure; "Figure" is all capitals; caption is sentence case; all type is boldface; extra space but no punctuation after number; period at end of caption.)

Body of the manuscript

Introduction

State the objectives of the work and provide an adequate background, avoiding a detailed literature survey or a summary of the results.

Materials and methods

Provide sufficient detail to allow the work to be reproduced. Methods already published should be indicated by a reference: only relevant modifications should be described.

Theory/calculation

A Theory section should extend, not repeat, the background to the article already dealt with in the Introduction and lay the foundation for further work. In contrast, a Calculation section represents a practical development from a theoretical basis.

Results

Results should be clear and concise.

Discussion

This should explore the significance of the results of the work, not repeat them. A combined Results and Discussion section is often appropriate. Avoid extensive citations and discussion of published literature.

Conclusions

The main conclusions of the study may be presented in a short Conclusions section, which may stand alone or form a subsection of a Discussion or Results and Discussion section.

Appendices

If there is more than one appendix, they should be identified as A, B, etc. Formulae and equations in appendices should be given separate numbering: Eq. (A.1), Eq. (A.2), etc.; in a subsequent appendix, Eq. (B.1) and so on. Similarly for tables and figures: Table A.1; Fig. A.1, etc.

Essential title page information

• ***Title.*** Concise and informative. Titles are often used in information-retrieval systems. Avoid

abbreviations and formulae where possible. The title should be all capitals.

• ***Author names and affiliations.*** Where the family name may be ambiguous (e.g., a double name), please indicate this clearly. Present the authors' affiliation addresses (where the actual work was done) below the names. Indicate all affiliations with a lower-case superscript letter immediately after the author's name and in front of the appropriate address. Provide the full postal address of each affiliation, including the

country name, and, if available, the e-mail address of each author.

• ***Corresponding author.*** Clearly indicate who will handle correspondence at all stages of refereeing and publication, also post-publication. **Ensure that phone numbers (with country and area code) are provided in addition to the e-mail address and the complete postal address. Contact details must be kept up to date by the corresponding author.**

• ***Present/permanent address.*** If an author has moved since the work described in the article was done, or was visiting at the time, a 'Present address' (or 'Permanent address') may be indicated as a footnote to that author's name. The address at which the author actually did the work must be retained as the main, affiliation address. Superscript Arabic numerals are used for such footnotes.

Abstract

A concise and factual abstract is required. The abstract should state briefly the purpose of the research, the principal results and major conclusions. An abstract is often presented separately from the article, so it must be able to stand alone. For this reason, References should be avoided, but if essential, then cite the author(s) and year(s). Also, non-standard or uncommon abbreviations should be avoided, but if essential they must be defined at their first mention in the abstract itself.

Keywords

Immediately after the abstract, provide a maximum of 6 keywords, using American spelling and

avoiding general and plural terms and multiple concepts (avoid, for example, 'and', 'of'). Be sparing with abbreviations: only abbreviations firmly established in the field may be eligible. These keywords will be used for indexing purposes.

Abbreviations

Define abbreviations that are not standard in this field in a footnote to be placed on the first page of the article. Such abbreviations that are unavoidable in the abstract must be defined at their first mention there, as well as in the footnote. Ensure consistency of abbreviations throughout the article.

Acknowledgements

Collate acknowledgements in a separate section at the end of the article before the references and do not, therefore, include them on the title page, as a footnote to the title or otherwise. List here those individuals who provided help during the research (e.g., providing language help, writing assistance or proof reading the article, etc.).

Nomenclature and units

Follow internationally accepted rules and conventions: use the international system of units (SI).

If other quantities are mentioned, give their equivalent in SI.

Math formulae

Present simple formulae in the line of normal text where possible and use the solidus (/) instead of a horizontal line for small fractional terms, e.g., X/Y. In principle, variables are to be presented in italics. Powers of e are often more conveniently denoted by exp. Number consecutively any equations that have to be displayed separately from the text (if referred to explicitly in the text).

Footnotes

Footnotes should be used sparingly. Number them consecutively throughout the article, using superscript Arabic numbers. Many word processors build footnotes into the text, and this feature may be used. Should this not be the case, indicate the position of footnotes in the text and present the footnotes themselves separately at

the end of the article. Do not include footnotes in the Reference list.

Table footnotes

Indicate each footnote in a table with a superscript lowercase letter.

Tables

Number tables consecutively in accordance with their appearance in the text. Place footnotes to tables below the table body and indicate them with superscript lowercase letters. Avoid vertical rules. Be sparing in the use of tables and ensure that the data presented in tables do not duplicate results described elsewhere in the article.

References

Citation in text

Please ensure that every reference cited in the text is also present in the reference list (and *vice versa*). Any references cited in the abstract must be given in full. Unpublished results and personal communications are not recommended in the reference list, but may be mentioned in the text. If these references are included in the reference list they should follow the standard reference style of the journal and should include a substitution of the publication date with either 'Unpublished results' or 'Personal communication'. Citation of a reference as 'in press' implies that the item has been accepted for publication.

Web references

As a minimum, the full URL should be given and the date when the reference was last accessed. Any further information, if known (DOI, author names, dates, reference to a source publication, etc.), should also be given. Web references can be listed separately (e.g., after the reference list) under a different heading if desired, or can be included in the reference list.

References in a special issue

Please ensure that the words 'this issue' are added to any references in the list (and any citations in the text) to other articles in the same Special Issue.

Reference style

Text: Indicate references by number(s) in square brackets in line with the text. The actual authors can be referred to, but the reference number(s) must always be given. Example: '..... as demonstrated [3,6]. Barnaby and Jones [8] obtained a different result ....'

List: Number the references (numbers in square brackets) in the list in the order in which they appear in the text.

Examples:

Reference to a journal publication:

[1] J. van der Geer, J.A.J. Hanraads, R.A. Lupton, The art of writing a scientific article, J. Sci. Commun. 163 (2010) 51–59.

Reference to a book:

[2] W. Strunk Jr., E.B. White, The Elements of Style, fourth ed., Longman, New York, 2000.

Reference to a chapter in an edited book:

[3] G.R. Mettam, L.B. Adams, How to prepare an electronic version of your article, In: B.S. Jones, R.Z. Smith (Eds.), Introduction to the Electronic Age, E-Publishing Inc., New York, 2009, pp. 281–304.

Journal abbreviations source

Journal names should be abbreviated according to the List of title word abbreviations http://www.sciencemag.org/site/feature/contribinfo/prep/res/journal_abbrevs.xhtml

Submission checklist

The following list will be useful during the final checking of an article prior to sending it to the journal for review. Please consult this Guide for Authors for further details of any item.

Ensure that the following items are present:

One author has been designated as the corresponding author with contact details:

• E-mail address

• Full postal address
• Phone numbers
• Keywords

Further considerations

• Manuscript has been 'spell-checked' and 'grammar-checked'
• References are in the correct format for this journal
• All references mentioned in the Reference list are cited in the text, and *vice versa*
• Permission has been obtained for use of copyrighted material from other sources (including the Web)
• Color figures are clearly marked as being intended for color reproduction

AFTER ACCEPTANCE

Proofs

One set of page proofs (as PDF files) will be sent by e-mail to the corresponding author (if we do not have an e-mail address then paper proofs will be sent by post). If there is any correction, please list your corrections quoting line number. If, for any reason, this is not possible, then mark the corrections and any other comments on a printout of your proof and return by fax, or scan the pages and e-mail, or by post. Please use this proof only for checking the typesetting, editing, completeness and correctness of the text, tables and figures. Significant changes to the article as accepted for publication will only be considered at this stage with permission from the Editor. We will do everything possible to get your article published quickly and accurately – please let us have all your corrections within 48 hours. It is important to ensure that all corrections are sent back to us in one communication: please check carefully before replying, as inclusion of any subsequent corrections cannot be guaranteed. Proofreading is solely your responsibility.

Offprint

The corresponding author, at no cost, will be provided with a PDF file of the article *via* email (the PDF file is a watermarked version of the published article and includes a cover sheet with the journal cover image and a disclaimer outlining the terms and conditions of use). For an extra charge, paper offprints can be ordered via the offprint order form which is sent once the article is accepted for publication. Both corresponding and co-authors may order offprints at any time *via* e-mail (ajbse@ju.edu.sa)

AUTHOR INQUIRIES

For inquiries relating to the submission of articles (including electronic submission) please visit this journal's homepage. Contact details for questions arising after acceptance of an article, especially those relating to proofs, will be provided by the publisher.

DISCLAIMER

Jouf Science and Engineering Journal shall not take any responsibility for the contents of articles published in the journal and all such responsibility shall lie with the author/s. The opinions expressed in the articles are solely of the author/s and **JUSEJ** may not agree with such opinions in part or in full.

Jouf University Science and Engineering Journal (JUSEJ) 2023; 10(2): 01- 09
Published online: Dec. 2023 (https://www.ju.edu.sa/en/jouf-university-science-and-engineering-journal-jusej/home/)
Print ISSN: 1658-6670 ***Electronic ISSN:1658-9173 (1443/5074)***

Synthesis and characterization of perovskite magnesium titanate for solar cells applications

Mohammad Ashraf Ali [1*]

[1] Department of Chemical Engineering, College of Engineering, Jazan University, Jazan 45142, Saudi Arabia

***Corresponding author**

Mohammad Ashraf Ali
Email address:

maali8000@gmail.com

Submission Date: *June 10, 2023*
Accepted Date: *Sept. 03, 2023*

Perovskite magnesium titanate ($MgTiO_3$) nanoparticles with varying percentages of magnesium were synthesized through sol-gel method using titanium tetrachloride and magnesium nitrate as precursors. The optimum synthesis conditions to achieve sol were a pH of 4 and 70°C temperature with constant stirring. The powdered composite samples prepared were characterized by X-ray diffraction analysis (XRD), UV-visible spectroscopy and scanning electron microscopy (SEM). The XRD analysis shows that for the samples, $0.2MgTiO_3$, $0.4MgTiO_3$ and $0.6MgTiO_3$, the reference file matched was JCDPS 01-079-0831, and their empirical formula was found to be $MgTiO_3$. In case of $0.8MgTiO_3$ sample, it was observed that two reference files matched the values with JCDPS (00-025-1157 and 00-009-0016) and the empirical formulae was found to be Mg_2TiO_4 and $MgTi_2O_5$. The average crystallite sizes of synthesized perovskite magnesium titanate having different amounts of magnesium ranged from 17 to 30 nm. The optical band gaps of $0.2MgTiO_3$, $0.4MgTiO_3$ and $0.6MgTiO_3$ NPs samples were observed as 3.33, 3.40 and 3.48 eV respectively. The bandgap of $MgTiO_3$ NPs samples was found increasing with higher concentration of Mg. The SEM pictures of $MgTiO_3$ samples show the presence of nanoparticles with an average size of 25-30 nm.

Keywords: *perovskite, $MgTiO_3$, nanoparticles, magnesium titanate; sol-gel method; solar cell*

1. INTRODUCTION

A perovskite is a material having the crystal structure similar to the calcium titanium oxide or calcium titanate ($CaTiO_3$) which is the first time revealed perovskite crystal. Generally, perovskite compound has a chemical formula ABX_3, where 'A' and 'B' represent different cations and X as an anion. Perovskite material is a semiconductor that can transport the electric charge upon light irradiation. The scientist in the United Kingdom have found that the perovskite materials are better replacement for next-generation thin-film solar cells. Perovskites materials are replacing silicon due of its easier manufacturing process, lower cost, and greater flexibility [Bati, et al. (2023)]. A number of metals have been doped in TiO_2 for utilization in solar cells to enhance its optical performance during light irradiation [Kim et al. (2021); Karuppasamy et al. (2021); Nwankwo et al. (2020); Amalathas et al. (2019); Zhang et al. (2016)] and in dye sensitized solar cells [Shakir et al. (2018); Athira et al. (2020); Razali and Othman (2021)]. Magnesium metal has also been utilized in several studies as a dopant for TiO2 to prepare perovskite materials using different salts of titanium and magnesium. Some of the studies are described here. Arshad et al. (2021) synthesized TiO_2 with variable percent (1 to 3 wt% Mg) as a dopant using sol-gel route. The characterization results revealed that Mg doped mesoporous TiO_2 improved the morphology of TiO_2 based ETL film which provided an interface for the growth of absorber layer. Zahra et al. (2022) synthesized

magnesium doped titania with by varying Mg contents (1–5 wt%) through sol-gel method, which offer a very simple and economical route. Razali et al. (2021) utilized Titanium (IV) isopropoxide in ethanol and magnesium chloride to synthesize Mg doped titania. Athira et al. (2020) synthesized Mg-doped TiO_2 nanoparticles by the sol–gel technique. Giahi et al. (2019) reported a sol-gel method to synthesize Mg-doped TiO_2 nanoparticles from titanium tetraisopropoxide and magnesium sulfate. Ujwala et al. (2019) synthesized magnesium titanate by the sonochemical method using TiO_2 (P25) and magnesium nitrate hexahydrate as precursors. Shivaraju et al. (2017) synthesized Mg-doped TiO_2 using mild sol-gel method using titanium tetraisopropoxide and magnesium sulfate. Wang et al. (2015) reported perovskite solar cells with Mg-doped TiO_2 that performed excellent compared to TiO_2 and showed better optical transmission properties, better hole-blocking effect, and higher electron lifetime. Parthasarathy and Manorama (2007) have synthesized nanocrystalline $MgTiO_3$ by co-precipitation method involving titanium hydroxide and magnesium nitrate.

This study is about the synthesis of $MgTiO_3$ perovskite NPs samples having different loading of magnesium using a simple, economical and environment-friendly sol-gel synthesis method. The method adopted resulted in quite small crystallite size of perovskite NPs. A number of techniques including XRD, UV-DRS and SEM were used to characterize $MgTiO_3$ NPs samples for crystal structures, bandgap and morphology.

2. MATERIALS USED AND PEROVSKITE SYNTHESIS METHOD

2.1 MATERIALS AND CHEMICALS

The reagents used were titanium tetrachloride ($TiCl_4$), magnesium nitrate ($Mg(NO_3)_2$, isopropyl alcohol (C_3H_8O) and ethyl alcohol (C_2H_6O) and were of analytical grade from Aldrich. All chemicals and materials were used without any purification. The deionized water was prepared in the laboratory.

2.2 PREPARATION OF PEROVSKITE MGTIO$_3$ NPS

Perovskite magnesium titanate NPs with variable percent of magnesium were synthesized by an aqueous route of sol-gel process. The sols were prepared by dissolving titanium tetrachloride in isopropyl alcohol in stoichiometric ratio, diluting the sol with ethyl alcohol and deionized water taken in 1:2 weight ratio. A known quantity of magnesium nitrate solution prepared in water was added dropwise to the mixture at 70°C and pH 4 with constant stirring for three hours. The sol thus obtained was dried at 70°C for 4 hours and after grinding, the samples were calcined at 450°C for four hours. Four loadings of magnesium (0.2, 0.4, 0.6, and 0.8 wt%) were achieved over the titania to produce magnesium titanate NPs samples which were named as $0.2MgTiO_3$, $0.4MgTiO_3$, $0.6MgTiO_3$ and $0.8MgTiO_3$. The synthesis procedure is given in Figure 1.

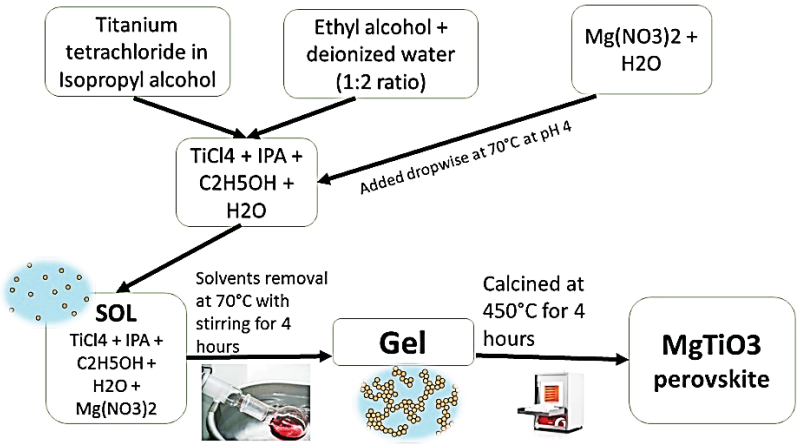

Figure 1. Synthesis procedure of $MgTiO_3$ NPs samples.

2.3. CHARACTERIZATION OF PEROVSKITE MGTIO3 NPS

The $MgTiO_3$ synthesized NPs samples were characterized by XRD, SEM and UV-visible spectroscopy. The XRD characterization was performed by X-ray diffractometer using monochromatised CuKα1 radiation having wavelength of 1.54060Å. The surface morphology of the samples was performed using scanning electron microscope S-3700N Hitachi Japan. The UV-visible diffused reflectance spectroscopy was performed using JASCO spectrophotometer model V-670 to investigate absorption characteristics and determining the band gap of the synthesized materials using Tauc plot.

3. RESULTS AND DISCUSSION

3.1 X-RAYS DIFFRACTION ANALYSIS OF MGTIO3 SAMPLES

The XRD pattern of $0.2MgTiO_3$ is shown in **Figure 2**. The XRD diffraction pattern shows peaks at 25.6, 33.0, 35.6, 40.7, 44.1, 49.2, 53.6, 56.9, 62.2, 63.8, and 67.0, which correspond to hkl values (012), (104), (110), (113), (024), (018), (124), (300), (215) respectively. Its crystal system determined was trigonal and the lattice system is rhombohedral. In this sample, a is 5.0548 Å, b is 5.0548 Å, and c is 13.8992 Å, and the value of Alpha (°): 90.0000, Beta (°): 90.0000 and Gamma (°): 120.0000. Besides, the calculated density was 3.89 g/cm, its cell volume was 3.0756×10^{-22} cm^3 ($307.56x10^6$ pm^3): and value of Z (number of chemical formula units in a unit cell) was 6.00. The data was extracted from the XRD pattern and is given in **Table 1.** The data was used to calculate the crystallite size of the synthesized sample and the texture coefficients. The average crystallite size calculated was 21.1 nm.

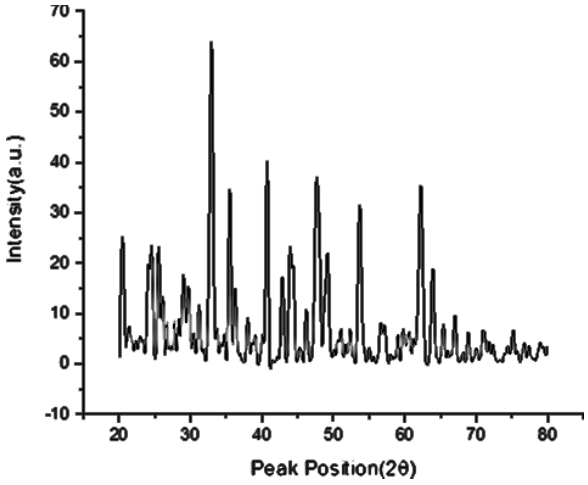

Figure 2. XRD pattern of $0.2MgTiO_3$ NPs sample.

Table 1. Crystalline parameters obtained from XRD pattern of $0.2MgTiO_3$ nanostructured sample.

2θ	d-spacing (nm)	Hkl	CS(nm)*	(FWHM)**	TC(hkl)***
25.6	0.336	012	24.34	0.3542	**0.237559**
33.0	0.295	104	23.93	0.3542	**0.196777**
35.6	0.286	110	23.76	0.3542	**0.211140**
40.7	0.277	113	35.09	0.2362	**0.302783**
44.1	0.251	202	11.56	0.7085	**6.391328**
49.2	0.223	024	45.38	0.1771	**0.349528**
53.6	0.186	116	19.09	0.4133	**1.084486**
56.9	0.182	018	08.23	0.9446	**0.061547**
62.2	0.174	124	16.02	0.4723	**1.524029**
63.8	0.168	300	15.89	0.4723	**0.182102**
67.0	0.160	303	08.53	0.8640	**1.458719**
				Average Crystallite Size 21.1 nm	

***CS** = crystallite size is inversely proportional to FWHM. Smaller the FWHM, sharper the peak and more the crystallite size. ****FWHM** =full width at half maximum of XRD profiles, FWHM=$\sqrt{(b^2/2 - 2ac)} / |a|$. *****TC**=texture coefficient

The XRD pattern of 0.4MgTiO3 is shown in **Figure 3**. The XRD diffraction method shows match peaks 21.4, 33.0, 35.5, 40.7, 51.5, 53.7, 57.1, 62.2, 63.8, 71.0, and 78.6. Crystalline plan of matching values of hkl values (101), (104), (110), (11-3), (107), (21-2), (12-4), (300), (1010), (1111). Its crystal system is trigonal and the lattice system is rhombohedral. In this sample, a: was 5.0548Å, b was 5.0548Å and c was 13.8992Å and the value of Alpha (°): 90.0000, Beta (°): 90.0000 and Gamma (°): 120.0000. The

density calculated was 3.89 g/cm^3, its cell volume was (307.56 x 10^6 pm^3): and Z (number of chemical formula units in a unit cell) was 6. The data extracted from the XRD pattern is given in **Table 2** and was used to calculate the crystallite size of the sample. The average crystallite size calculated was 30.6 nm.

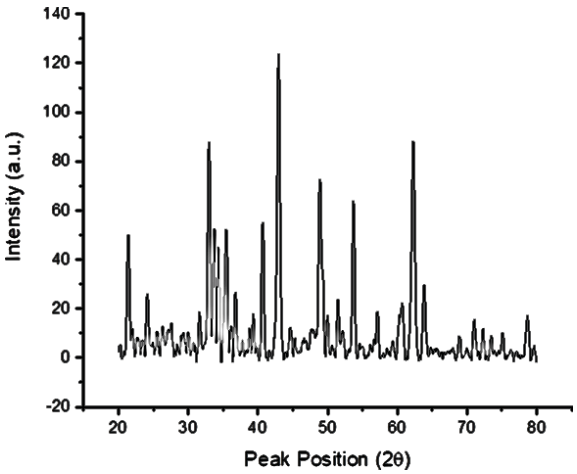

Fig. 3. XRD pattern of 0.4MgTiO$_3$ NPS sample.

Table 2. Different crystalline parameters obtained from XRD pattern of 0.4MgTiO$_3$ sample.

2θ	d-spacing (nm)	hkl	CS(nm)	FWHM	TC(hkl)
21.4	0.336	101	24.52	0.3542	**0.319869**
33.0	0.295	104	35.88	0.2362	**0.204210**
35.5	0.286	110	47.54	0.1771	**0.210735**
40.7	0.277	11-3	28.08	0.2952	**0.193983**
51.5	0.251	107	44.96	0.1771	**2.741939**
53.7	0.236	11-6	33.39	0.2362	**0.274680**
57.1	0.223	21-2	21.92	0.3542	**0.861108**
62.2	0.186	12-4	21.37	0.3542	**0.667742**
63.8	0.182	300	42.37	0.1771	**0.215849**
71.0	0.174	1010	20.32	0.3542	**0.246868**
78.6	0.168	1111	15.83	0.432	**6.063016**
		Average Crystallite Size = 30.6 nm			

The XRD pattern of 0.6MgTiO3 is shown in **Figure 4**. The XRD diffraction pattern shows match peaks 32.9, 40.5, 48.7, 51.6, 53.5, 62.2, and 74.9. Crystalline plan of matching values of hkl values were (104), (113), (024), (107), (116), (124), (127). In this sample, a: was 8.4409Å, b: was 8.4409Å and c: was 8.4409Å and the value of Alpha (°): 90.0000, Beta (°): 90.0000 and Gamma (°): 90.000. The calculated density was 3.89 g/cm^3, its cell volume (601.40 x 10^6 pm^3) and Z (number of chemical formula units in a unit cell) was 8.00. The data extracted from the XRD pattern is given in **Table 3** and it was used to calculate the crystallite size of the sample. The average crystallite size calculated was 25.2 nm.

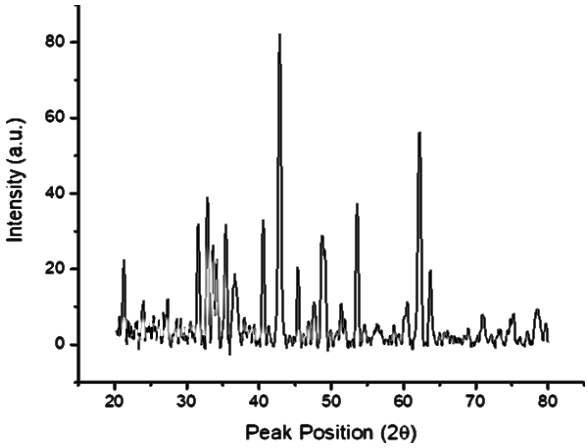

Fig. 4. XRD pattern of 0.6MgTiO$_3$ NPs sample.

Table 3. Crystalline parameters obtained from XRD pattern of 0.6MgTiO$_3$ NPs sample.

2θ	d-spacing (nm)	Hkl	Crystallite Size (nm)	FWHM	TC(hkl)
32.9	0.336	104	47.71	0.1777	**0.491641**
40.5	0.295	113	28.09	0.2952	**0.533150**
48.7	0.286	24	45.47	0.1771	**0.949175**
51.6	0.277	107	08.42	0.9446	**3.032222**
53.5	0.251	116	22.28	0.3542	**0.558437**
62.2	0.236	124	18.31	0.4133	**1.873446**
74.9	0.223	127	06.09	1.1520	**4.561930**
		Average Crystallite Size is 25.20			

The XRD pattern of 0.8MgTiO3 is shown in **Figure 5**. The XRD diffraction pattern shows matching peaks at 36.9, 43.0, 46.1, 56.3, 62.2, 65.5, 75.1 and 78.7. The crystalline plan of matching values of hkl values (222), (400), (331), (333), (440), (531), and (622). In this sample a: was 8.4409Å, b: was 8.4409Å and c: was 8.4409Å and the value of Alpha (°): 90.0000, Beta (°): 90.0000 and Gamma (°): 90.000. The density calculated was 3.89 g/cm^3, its cell volume (601.40 x 10^6 pm^3): and Z was 8.00. The data was extracted from the XRD pattern is given in **Table 4**, and was used to calculate the crystallite size of the sample. The average crystallite size calculated

was 16.9 nm. Other parameters calculated were crystalline structure and texture coefficients (**Thamaphat et al., 2008**).

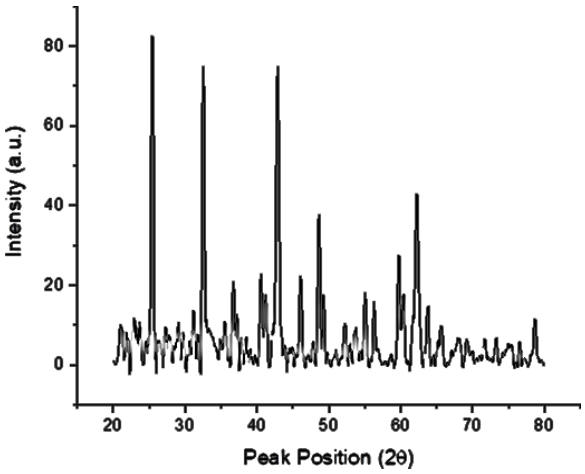

Fig. 5. XRD pattern of $0.8MgTiO_3$ NPs sample.

Table 4. *Different crystalline parameters obtained from XRD pattern of $0.8MgTiO_3$ NPs sample.*

2θ	d-spacing (nm)	hkl	CS(nm)	FWHM	TC(hkl)
36.9	0.336	222	11.84	0.7085	**1.891627**
43.0	0.295	400	19.90	0.4133	**0.322666**
46.1	0.286	331	22.97	0.3542	**6.362139**
56.3	0.277	333	33.00	0.2362	**0.191387**
62.2	0.251	440	25.64	0.2952	**0.276972**
65.5	0.236	531	10.49	0.7085	**0.937473**
75.1	0.223	622	07.42	0.9446	**1.247740**
78.7	0.186	444	15.82	0.4320	**0.769996**
			e Crystallite Size = 16.90 nm		

3.2 *3.2 COMPARATIVE ANALYSIS OF XRD PATTERNS*

Figure 6 shows the XRD pattern of $0.2MgTiO_3$, $0.4MgTiO_3$, $0.6MgTiO_3$ and $0.8MgTiO_3$ recorded at room temperature. The peak positions for $0.2MgTiO_3$, $0.4MgTiO_3$, $0.6MgTiO_3$ samples observed at 2θ values are 32.5°, 35.3°, 40.5°, 42.8°, 48.7°, 53.5°, 62.1° and 63.5° which correspond to the crystalline planes (indicated with stars) (104), (110), (021), (024), (116), (124) and (027) respectively. In these samples, the reference file matched was JCDPS 01-079-0831, and the empirical formula of these samples is $MgTiO_3$.

The peak position for $0.2MgTiO_3$ sample were observed at 2θ values (25.3, ° 32.5°, 35.5°, 36.6°, 40.4°, 42.8°, 46.0°, 48.4°, 54.9°, 56.2°, 59.6°, and 62.9°) correspond to crystalline planes show with rhombus is (022), (023), (311), (222), (024), (400), (331), (142), (006), (333), (062) and (333) respectively. In this sample, we observed two reference files matched the values with JCDPS (00-025-1157 and 00-009-0016) and the ICSD name is magnesium titanium oxide having empirical formulae Mg_2TiO_4 and $MgTi_2O_5$. The ionic radii of Ti^{2+} is 0.61Å and the ionic radii of Mg^{2+} is 0.72Å. The average crystallite sizes of $0.2MgTiO_3$, $0.4MgTiO_3$, $0.6MgTiO_3$ and $0.8MgTiO_3$ were 21.1 nm, 30.6 nm, 25.2 nm and 16.9 nm respectively. **Parthasarathy and Manorama (2007)** have reported synthesis of nanocrystalline MgTiO3, and described crystallite size of 20–40 nm. The average dislocation density calculated was $1.24x10^{15}$ lines/m^2, $5.1x10^{15}$ lines/m^2, $5.9x10^{15}$ lines/m^2 and $4.11x10^{15}$ lines/m^2 of the synthesized $MgTiO_3$ NPs samples. **Table 5** shows comparative analytical data extracted from XRD patterns of four samples, $0.2MgTiO_3$, $0.4MgTiO_3$, $0.6MgTiO_3$ and $0.8MgTiO_3$.

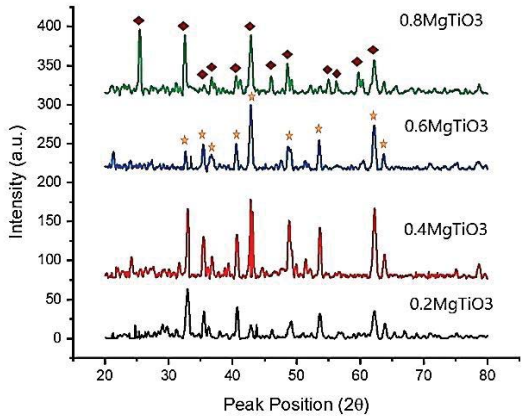

Fig. 6. XRD patterns overlay of $MgTiO_3$ NPs perovskite samples.

Table 5. *Comparative data extracted from XRD patterns of $0.2MgTiO_3$, $0.4MgTiO_3$, $0.6MgTiO_3$ and $0.8MgTiO_3$.*

Sample	Lattice parameters (nm)		Average Crystallite size (nm)	Dislocation density (lines/m^2)	Strain
	a	c			
$0.2MgTiO_3$	0.5820	0.7802	21.1	$1.24*10^{15}$	0.043
$0.4MgTiO_3$	0.6305	0.4575	30.6	$5.10*10^{15}$	0.028
$0.6MgTiO_3$	0.6700	0.6792	25.2	$5.90*10^{15}$	0.027
$0.8MgTiO_3$	0.7181	0.7181	16.9	$4.11*10^{15}$	0.112

3.3 UV-VISIBLE SPECTROSCOPY OF PEROVSKITE MGTIO3 NPS

The absorption peak edges observed at 214, 218, 220 and 221 nm for 0.2$MgTiO_3$, 0.4$MgTiO_3$, 0.6$MgTiO_3$ and 0.8$MgTiO_3$ NPs samples are shown in **Figures 7**. The optical properties are varying by the substitution of Mg ion in the TiO2 matrix as absorption peak edge values increased with increasing the concentration of Mg ions, which is indicated that Mg ions were substituted into TiO2 lattice sites. The optical band gap (Eg) was calculated by the following relation: $(\alpha hv)2=A(hv-Eg)2$, Where the optical band gap denoted by Eg, A is the constant and the exponent n depends on the type of transition. The n = 1/2 for permitted direct transition, 2 for allowed indirect transition 3/2, and 3 for forbidden direct and indirect transitions respectively (**Hagfeldt and Graetzel, 1995**). The $(\alpha hv)2$ plot as a function of hv are shown in **Figures 8**. The optical band gaps of 0.2$MgTiO_3$, 0.4$MgTiO_3$ and 0.6$MgTiO_3$ NPs samples were observed as 3.33, 3.40 and 3.48 eV respectively. The bandgap of MgTiO3 NPs samples was found increased with higher concentration of Mg. The band gap energy of MgO is 4.2eV and TiO2 3.2 eV.

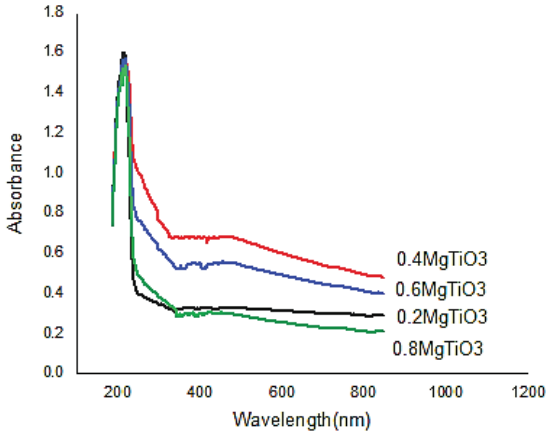

Fig. 7. Overlay of UV-Visible spectra of MgTiO3 NPs samples.

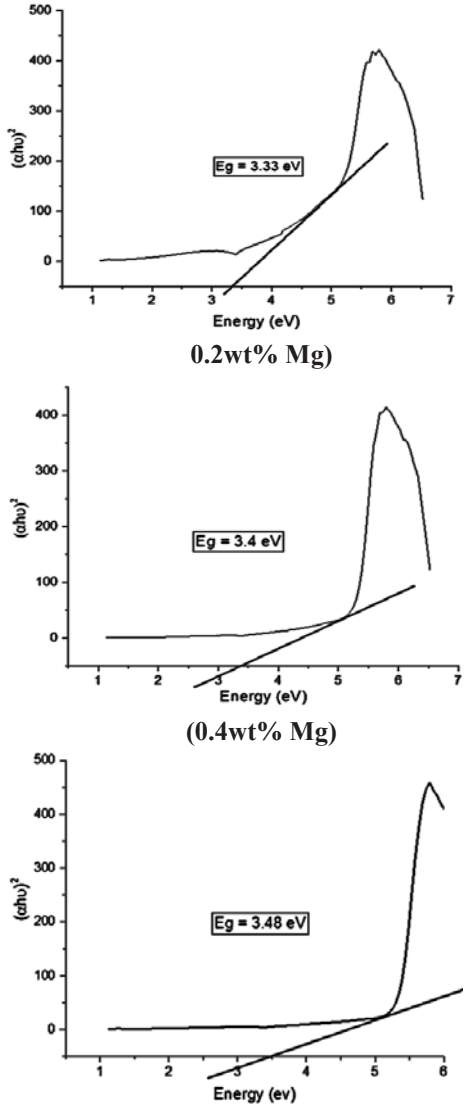

Fig. 8. Plot of $(\alpha hv)^2$ as a function of hv for 0.2$MgTiO_3$, 0.4$MgTiO_3$, and 0.6$MgTiO_3$ NPs perovskite samples.

3.4 SEM ANALYSIS OF MGTIO3 NPS

Figure 9 shows the SEM images of 0.2MgTiO3 and 0.4MgTiO3 NPs samples at 5.0 and 0.5µm magnifications. The SEM images shows that the nanosize particles have formed into micron size softly bound agglomerates of uneven shapes. The SEM pictures of $MgTiO_3$ samples show the presence of nanoparticles with an average size of 25-30 nm. Solgi et al. (2021) have reported 18-60 nm particle size of synthesized $MgTiO_3$ from $MgSO_4.7H_2O$ salt.

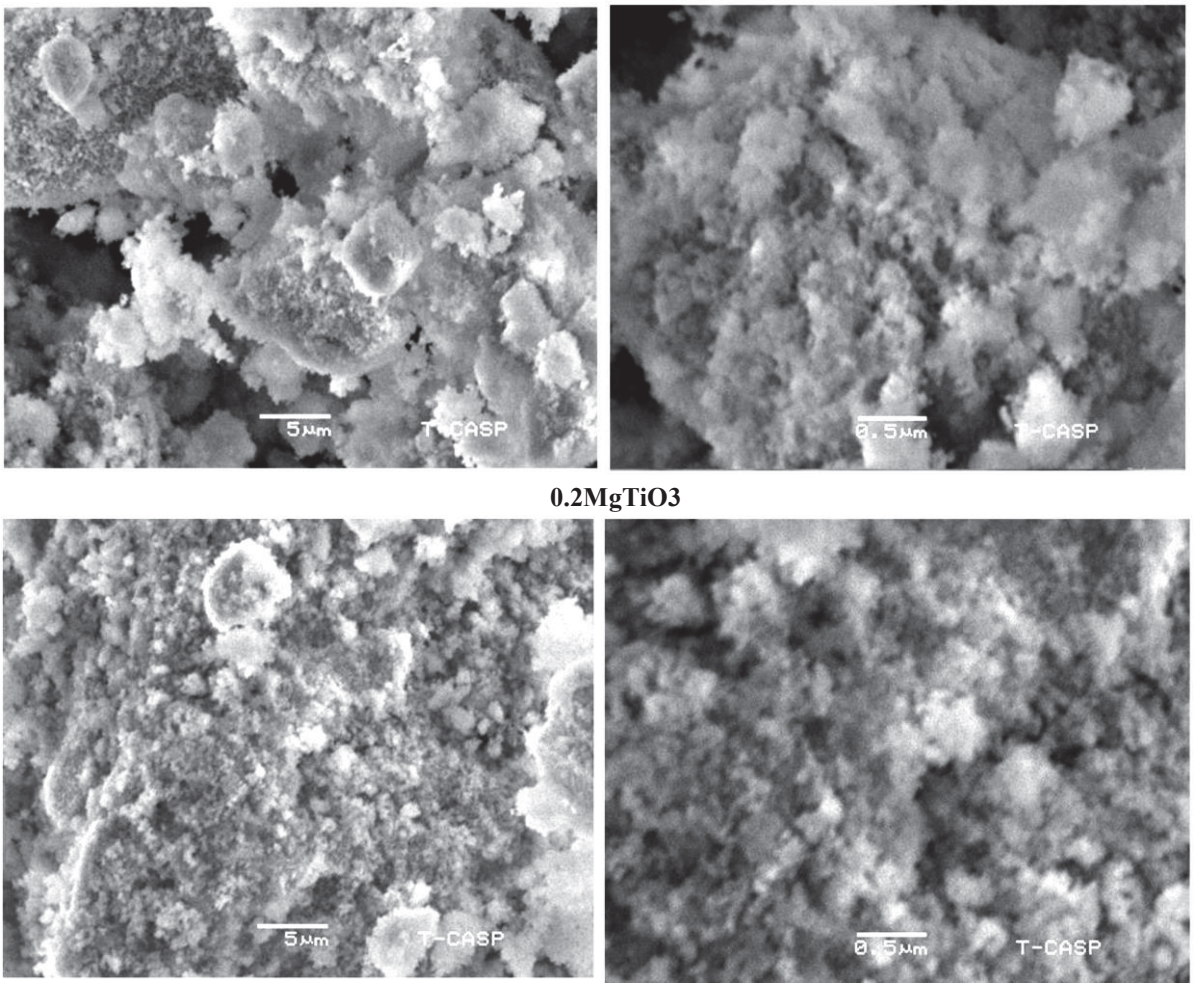

Fig. 9. SEM images of 0.2MgTiO3 and 0.4MgTiO3 NPs samples at 5.0 and 0.5µm magnifications.

4. CONCLUSIONS

Perovskite magnesium titanate NP samples with variable percentages of magnesium were synthesized at optimum conditions of pH of 4 and 70°C temperature and then the gel obtained was calcined at 500°C. The crystal structure system was found to be trigonal and the lattice system was rhombohedral while in other cases, the crystal structure was cubic based on the reference XRD patterns. For $0.2MgTiO_3$, $0.4MgTiO_3$, $0.6MgTiO_3$ and $0.8MgTiO_3$ NPs samples, the average crystalline sizes were 21.1 nm, 30.6 nm, 25.20 nm and 16.9 nm and the average dislocation density calculated was 1.24×10^{15} lines/m^2, 5.1×10^{15} lines/m^2, 5.9×10^{15} lines/m^2 and 4.11×10^{15} lines/m^2 respectively. The absorption peak edges observed were 214, 218, 220 and 221 nm for $0.2MgTiO_3$, $0.4MgTiO_3$, $0.6MgTiO_3$ and $0.8MgTiO_3$ NPs samples. The optical band gaps of $0.2MgTiO_3$, $0.4MgTiO_3$ and $0.6MgTiO_3$ NPs samples determined were 3.33, 3.40 and 3.48 eV respectively. The powdered composite samples were characterized by X-ray diffraction analysis (XRD), UV-visible spectroscopy and scanning electron microscopy (SEM). The SEM pictures of $MgTiO_3$ samples show the presence of nanoparticles with an average size of 25-30 nm.

FUNDING STATEMENT: No research funding was used for this study.

CONFLICTS OF INTEREST: The author declares No conflict of interest.

ACKNOWLEDGMENT: The author would like to appreciate the support of Jazan University for this publication.

5 REFERENCES

[1] Amalathas A. P., L. Landov´, B. Conrad, J. Holovský, Concentration-dependent impact of alkali Li metal doped mesoporous TiO2 electron transport layer on the performance of CH3NH3PbI3 perovskite solar cells, J. Phys. Chem. C 123 (32) (2019) 19376–19384. https://doi.10.1021/ACS.JPCC.9B05355.

[2] Arshad Z., Asif Hussain Khoja, Sehar Shakir, Asif Afzal, M.A. Mujtaba, Manzoore Elahi M. Soudagar, H. Fayaz, Ahamed Saleel C, Sarah Farukh, Mudassar Saeed, Magnesium doped TiO2 as an efficient electron transport layer in perovskite solar cells, Case Studies in Thermal Engineering, Volume 26, 2021, 101101. https://doi.org/10.1016/j.csite.2021.101101.

[3] Athira K., K.T. Merin, T. Raguram, K.S. Rajni, Synthesis and characterization of Mg doped TiO2 nanoparticles for photocatalytic applications, Materials Today: Proceedings, Volume 33, Part 5, 2020, 2321-2327. https://doi.org/10.1016/j.matpr.2020.04.580.

[4] Bati, A.S.R., Zhong, Y.L., Burn, P.L. et al. Next-generation applications for integrated perovskite solar cells. Commun Mater **4**, 2 (2023). https://doi.org/10.1038/s43246-022-00325-4.

[5] Giahi, Masoud and Pathania, Deepak and Agarwal, Shilpi and Ali, Gomaa A. M. and K. F., Chong and Gupta, Vinod Kumar (2019). Preparation of Mg-doped TiO2 nanoparticles for photocatalytic degradation of some organic pollutants. Studia Universitatis Babes-Bolyai, Chemia, 64 (1). pp. 7-18. https://doi.10.24193/subbchem.2019.1.01.

[6] Hagfeldt A. and Graetzel M., Light-Induced Redox Reactions in Nanocrystalline Systems, Chem. Rev. 1995, 95, 1, 49–68. https://doi.org/10.1021/cr00033a003.

[7] Karuppasamy P., Nagoorkani Ramzan Nilofar Nisha, Arivalagan Pugazhendhi, Sabariswaran Kandasamy, Sakthivel Pitchaimuthu, An investigation of transition metal doped TiO2 photocatalysts for the enhanced photocatalytic decoloration of methylene blue dye under visible light irradiation, J. Environ. Chem. Eng. 9(4), 2021, 105254. https://doi.org/10.1016/j.jece.2021.105254.

[8] Kim M., I.W. Choi, S.J. Choi, J.W. Song, S.I. Mo, J.H. An, D.S. Kim, Enhanced electrical properties of Li-salts doped mesoporous TiO2 in perovskite solar cells, Joule 5 (3) (2021) 659–672. https://doi.10.1016/j.joule.2021.02.007.

[9] Nwankwo U., S. Ngqoloda, A.C. Nkele, C.J. Arendse, K.I. Ozoemena, A.B.C. Ekwealor, F.I. Ezema, Effects of alkali and transition metal-doped TiO2 hole blocking layers on the perovskite solar cells obtained by a two-step sequential deposition method in air and under vacuum, RSC Adv. 10 (22) (2020) 13139–13148. https://doi.10.1039/d0ra01532f

[10] Parthasarathy G.; and S. V. Manorama, A novel method for synthesizing nano-crystalline MgTiO3 geikielite, Bull. Mater. Sci., Vol. 30, No. 1, February 2007, pp. 19–21. https://doi.org/10.1007/s12034-007-0004-y

[11] Razali N.A., Othman S.A., Study of photocatalytic performance of doping titanium dioxide (TiO2), Journal of Science and Mathematics Letters 9 (2021) 72–79. https://doi.org/10.37134/jsml.vol9.sp.9.2021.

[12] Razali, N., Aliaa, & Othman, S. A. (2021). Study of Photocatalytic Performance of Doping Titanium Dioxide (TiO2).Journal of Science and Mathematics Letters, 9, 72-79. https://doi.org/10.37134/jsml.vol9.sp.9.2021

[13] Shakir S., H.M. Abd-ur-Rehman, K. Yunus, M. Iwamoto, V. Periasamy, Fabrication of un-doped and magnesium doped TiO2 films by aerosol assisted chemical vapor deposition for dye sensitized solar cells, J. Alloys Compd. 737 (2018) 740–747. https://doi.10.1016/J.JALLCOM.2017.12.165

[14] Shivaraju H.P., Midhun G., Anil Kumar, K.M. et al. Degradation of selected industrial dyes using Mg-doped TiO2 polyscales under natural sun light as an alternative driving energy. Appl Water Sci 7, 3937–3948 (2017). https://doi.org/10.1007/s13201-017-0546-0.

[15] Solgi, S., Seyed Dorraji, M., Hosseini, S.F. et al. Improvement of microwave absorption properties of polyester coatings using NiFe2O4, X-doped g-C3N4 (X = S, P, and O), and MTiO3 (M = Fe, Mg, and Zn) nanofillers. Sci Rep 11, 19339 (2021). https://doi.org/10.1038/s41598-021-98666-6

[16] Thamaphat, K., Pichet Limsuwan, and Boonlaer Ngotawornchai. 2008. "Phase Characterization of TiO2 Powder by XRD and TEM". Agriculture and Natural Resources 42 (5). Bangkok, Thailand: 357-61. https://li01.tci-thaijo.org/index.php/anres/article/view/244620.

[17] Ujwala O., Bhagwat, Prof. Jerry J. Wu, Prof. Abdullah M. Asiri, Prof. Sambandam Anandan, Synthesis of MgTiO3 Nanoparticles for Photoca talytic Applications,ChemistrySelect 2019, 4, 788. https://doi.org/10.1002/slct.201803583.

[18] Wang J., Minchao Qin, Hong Tao, Weijun Ke, Zhao Chen, Jiawei Wan, Pingli Qin, Liangbin Xiong1,2, Hongwei Lei, Huaqing Yu, and Guojia Fang, Performance enhancement of perovskite solar cells with Mg-doped TiO2 compact film as the hole-blocking layer, Appl. Phys. Lett. 106, 121104 (2015). https://doi.org/10.1063/1.4916345.

[19] Zahra S., Sania Mazhar, Sarwat Zahra, Hira Idrees, Ali Hussnain, Synthesis and characterization of magnesium doped titania for photocatalytic degradation of methyl red, Matéria (Rio J.) 27(01) 2022. https://doi.org/10.1590/1517-7076-RMAT-2021-44880.

[20] Zhang H., J. Shi, X. Xu, L. Zhu, Y. Luo, D. Li, Q. Meng, Mg-doped TiO2 boosts the efficiency of planar perovskite solar cells to exceed 19%, J. Mater. Chem. 4 (40) (2016) 15383–15389. https://doi.org/10.1039/C6TA06879K.

Jouf University Science and Engineering Journal (JUSEJ) 2023; 10(2): 10- 28
Published online: Dec. 2023 (https://www.ju.edu.sa/en/jouf-university-science-and-engineering-journal-jusej/home/) ***Print ISSN: 1658-6670*** ***Electronic ISSN:1658-9173 (1443/5074)***

Benchmarking urban planning and development: Sustainable, environmental and economic prospects in Riyadh, Eastern and Al-Baha provinces

Naief A. Aldossary[1*]

[1] Department of Architecture, Faculty of Engineering, Al-Baha University, Al-Baha P.O. Box 1988, Saudi Arabia

***Corresponding author**

Naief A. Aldossary

Email address:

Dr_naief@bu.edu.sa

Submission Date: *Sept. 11, 2023*
Accepted Date: *Sept. 23, 2023*

This study examines the urban and architectural factors influencing urban development in three provinces in Saudi Arabia, focusing on local development and infrastructure. The research will investigate and benchmark the urban planning and development of each region, considering climatic conditions, environment, topography and economics. Riyadh province, the eastern province and Al-Baha province have been selected due to their differences, so as to offer a broader understanding of urban development in Saudi Arabia. Riyadh province is a desert region, the eastern province is a coastal region and Al-Baha province is a mountainous region. The data used was gathered from the ministry of municipality and included information on urban development, mapping and quantitative data. The study discussed a number of urban facilities that contribute to the local economy, which have been set up to encourage the population to remain in the area. The results provide a benchmark for urban development incorporating environmental issues, the application of renewable energy resources, and economic prospects. The data includes information regarding each area's educational facilities and universities, sea and air ports, and factories, as these play a significant role in promoting urban development. Additional local urban factors, such as the preservation of forests in Al-Baha are considered where relevant. The study concludes with a number of recommendations for decision makers, urban developers and researchers.

Keywords: *Urban facilities; Architectural identity; urban development; environmental protection*

1. INTRODUCTION

The phenomenon of migration from rural towns and villages to cities in Saudi Arabia is a historical process that has shaped the local economies of its regions, as well as their social culture and history [1]. Expectations regarding continuing development are a factor considered when planning cities in response to the increased demand for services and urbanization [2]. Certainly, the movement of populations from remote villages to cities and towns has expanded the local economies in such areas, generating urban sprawl [3]. Since the 1960s, Saudi Arabia has seen a marked increase in urban development [4] that does not accord with the conventional urban planning strategies applied in Saudi Arabia for many centuries [4]. To date, the government and decision makers have chiefly focused on developing all of the Kingdom's regions to prevent an exodus of local populations, including

uniformly establishing new urban facilities and employment opportunities.

- Saudi Arabia is the largest nation in the Arabian peninsula, with thirteen provinces containing a variety of levels of urban development, along with related infrastructure and facilities [5]. One of these is the Al-Baha region, which has had a long history of navigating the migration of its population to other Saudi regions, in search of education and employment. This internal migration has affected local development, tourism and the economy. In recent years, the development of the tourism industry (i.e. 'heritage development') has lifted the local economy, resulting in sufficient urban sprawl to necessitate the creation of new neighborhoods and public facilities, as well as a fresh urban infrastructure in the form of 'urban sprawl' [6]. Since the establishment of a new university in 2006, the Al-Baha region has undergone considerable development, alongside improved urban facilities and the creation of new jobs. These have created urban sprawl throughout the region, which is a significant consideration in contemporary local urban development.

- Historically, members of the local population had chosen to leave Al-Baha for specific reasons, in particular to obtain a university education. However, managing urban facilities effectively can address gaps in city planning, including providing connectivity between neighborhoods by applying the Smart City concept. This aims to optimize access to data and focuses on prominent governance structures concerning facility management, urban facility management and city planning [7]. In addition, the value of both real estate and property tends to be heavily impacted by the development of urban facilities in Smart Cities. Green urban areas, in particular, are acknowledged for their positive impact on the well-being of the urban population [8]. However, no previous research has focused on the future use of urban green spaces by different segments of the population, as or the need to connect such spaces with social infrastructure [9].

- This study examines this aspect, and is structured as follows: (1) introduction; (2) overview of the Al-Baha region; (3) research methodology; (4) results and analysis; (5) discussion; and (6) conclusion and recommendations..

1.1. URBAN PLANNING AND DEVELOPMENT IN SAUDI ARABIA

The significance of the role of quickly emerging nations in reducing greenhouse gas emissions is increasingly attracting international attention. According to estimates, developing nations' carbon dioxide (CO2) emissions in 2011 comprised approximately 63% of global emissions, in contrast with eh 37% produced by developed countries [10]. To address this, planning authorities worldwide are using e-participation more frequently to strengthen and facilitate public participation in decision-making processes [11]. The potential to leverage information and communication technology to encourage public participation in urban planning contexts in traditional Arab communities is yet to be fully understood [11]. Undoubtedly, the negative effects of urban development patterns to date have encouraged Saudi Arabia to implement a variety of different strategies. Reviewing the historical spread of these strategies reveals that while they may have, improved the infrastructure in some areas of the Kingdom's major cities in the short term, their longer-term prospects have been less encouraging, as many of the challenges associated with urbanization remain [12].

The weather in Al-Baha region is greatly influenced by its diverse mountainous topography, where average temperatures in summer range between 12 and 23 °C. In Tihama, the climate is hot in summer, warm in spring and mild in winter, with level of humidity ranging from 52% to 67%, and an annual rainfall below 100 mm. Typically, towns and villages within mountainous areas tend to experience a higher degree of solar radiation relative to those in coastal areas [13]. Altitude results in cooler weather in both summer and winter, with high levels of annual rainfall, as well as rich forestry and other wildlife habitats [14, 15]. This study also focuses on urban factors and

facilities in the Al-Baha region, which have paralleled the recent increase in population, advancing the contribution to the local economy. When rapid urbanization emerges as a key theme in urban research and planning, especially in the Global South, it is important to address the meaning of these radical effects on the urban environment.

This article reviews the literature on urbanization and its impact on the urban environment of the Global South, also drawing on sustainability studies and environmental studies. It further discusses the eight effects of urbanization and environmental issues: pollution, water resource degradation, urban heat island effect, sea level and urban flooding, urban sprawl and slum growth, urban agriculture decline, public health degradation, and destruction of urban wetlands, including the challenging nature of urbanization in the cities of the global south [16]

2. METHODOLOGY

All studies need to be designed to ensure researchers can attain their goals by establishing a research question and designing an appropriate research method, as discussed below.

2.1 ESTABLISHING THE RESEARCH QUESTIONS

This study examines the factors influencing urban sprawl, and analyses data gathered from those who have migrated from another regions or countries, including their personal reasons for migrating. The data collection focuses on answering the following research questions:

- Research question one: What are the factors informing urban development in three different provinces in Saudi Arabia?
- Research question two: How far are environmental and renewable energy technologies applied to urban development?
- Research question three: How can urban development adapt to local climatic conditions and topography?

To answer the research questions, it is essential to investigate urban planning and development in three different regions of Saudi Arabia, taking into account urban features, urbanism factors, urban development changes and locations. For this purpose, Riyadh city, Al-Baha city and Damam city were selected as case studies for analysis. Urban plans and development were obtained for analysis and to offer a benchmark approach.

2.2 BENCHMARK APPROACH

Benchmarking requires the extraction of information to improve upon the actions associated with strategic choices and consumer expectations through company processes, prioritizing improvements and actions to significantly advance strategic goals. It draws on ideas concerning management, such as performance evaluation and other tools, as well as business process mapping. A set of instructions to direct the execution of such an approach have been proposed and covered in full after some preliminary theoretical background and discussion of the concept. Notions about validity, and the concerns associated with the possible advantages and limitations of this concept are then discussed in two scenarios associated with the application. To compare organizations, [17] introduces "evolutionary benchmarking" methodology, discussing the framework's design and functioning, as well as its alleged benefits as a benchmarking tool. The benchmarking method proposed also makes use of cladistics, an evolutionary categorization technique. It demonstrates how a proposed framework supports benchmarking by representing benchmarking information, and improving the quality and validity of that information in accordance with the classification rules of parsimony, congruence, and homology, offering a comparison to demonstrate how such practices should be adopted. The example classification for automotive assembly plants is used to demonstrate how the proposed framework supports benchmarking. Evaluations of benchmarking methodology, including those that classify the results from benchmarking studies suggest this framework is helpful [18].

2.3 SELECTING CASE STUDY CRITERIA

Saudi Arabia has 13 provinces, each with unique social, economic and environmental issues, and a specific framework to support urban planning and development in each region. Key issues relate to urban land use, transportation, energy conservation, housing demand and tourism. Al-Baha region has particular environmental and topographical challenges, but offers some advantages in terms of climatic conditions for agriculture and tourism and challenges to its topography for future development. This study will apply a benchmarking approach to all the case study regions, considering their different topographical climatical condition and different economical purposes. The three selected regions are: (a) Riyadh region which is one of the biggest regions marked by tourism and industry, (b) Eastern region due to its coastal economy and tourism and its topographical challenges, and (c) Al-Baha region with topographical challenges, forested zones and agricultural and tourism (Fig.1).

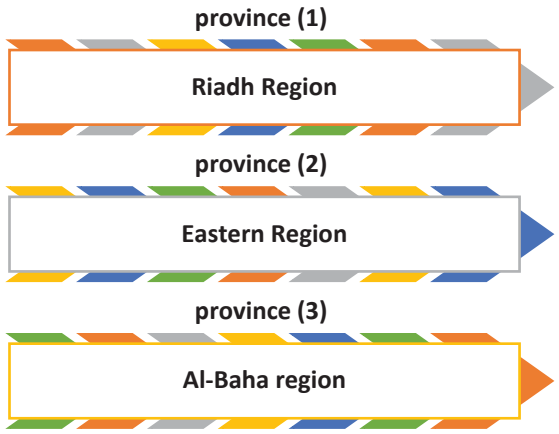

Fig. 1. The three selected provinces

3. RESULTS AND ANALYSIS

The capacity of each region depends on its location, the number of governorates and its local economic system. Furthermore, it is essential to confirm that climate conditions play a significant role, especially in relation to agriculture. The three selected regions differ geographically, environmentally, and by number of governorates as presented in table 1 below.

Table 1: *The three regions selected*

	Number governorates	Annual rainfall
Riyadh province [19]	21 governorates	84.4 millimetres
Easter provinces [20]	11 governorates	86 millimetres
Al-Baha province [21]	7 governorates	The rainfall data in Abha and Al-Baha indicate variable patterns over the past 10 years

Key urban factors consequently vary between the regions, in association with location and environmental conditions. The benchmark will focus on road hierarchy, urban sprawl, attractiveness of facilities, local economic factors, food productions, ports, forests, agriculture and wildlife habitat. Table 2 shows the benchmarking for the three regions for 17 different urban factors. It highlights how urban development requires particular local environmental factors to determine development.

Table 2: *Urban factors in three different cities in Saudi Arabia*

Urban Factor	Riyadh city	Damam City	Al-Baha city
Housing factor	Applied	Applied	Applied
New net road and hierarchy	Applied	Applied	Partly applied
New subdivision plans	Applied	Applied	Partly applied
Universities	Applied	Applied	Applied
Private colleges	Applied	Applied	Not Applied
Tourism facilities	Applied	Applied	Partly applied
Recreational facilities	applied	Partly applied	applied
Factories	Applied	Applied	Not Applied
International airport	Applied	Applied	Not Applied
Seaport	Not Applied	Applied	Not Applied
Commercial facilities	Applied	Applied	Applied
Agriculture activities	Applied	Applied	Applied
Fish production	Not Applied	Not Applied	Not Applied
Wildlife habitat	Partly applied	Partly applied	Applied

Forestry areas	Not Applied	Not Applied	Applied
Urban sprawl with forestry protection	Not Applied	Not Applied	Applied
Urban sprawl with topography protection	Partly Applied	Partly Applied	Partly Applied

3.1 RIYADH REGION

In the past years, the city of Riyadh has expanded from a small town with less than 500,000 residents to become a major city, home to more than 6 million residents [22]. There are few examples of cities that can compare in terms of the pace and scope of its development. The extent and progress of the city's urban development are explored in this article [22]. Progress is broken down into six stages: the first and second lay the groundwork for city development up to the mid-1960s; the third deals with the Doxaidis master plan from the late 1960s; the fourth, the oil boom in the mid-1970s and SCET's update to the master plan; the fifth, ADA's efforts to control the city's urban expansion in the 1980s and 1990s; and the sixth, the MEDSTAR project, subsequent updates, and the launch of Riyadh Public [22]. The suburbanization of Riyadh, creating homes for 4.5 million people, offers an interesting opportunity to examine the urban morphology of the city relative to socio-political and financial conditions [23]. Central government laws result in 'dysfunctional' sprawl, covering enormous areas with excessively wide roads [23]. Riyadh has also witnessed a rise in car ownership alongside the population increase [24]. Urban and regional planning in relation to the advancement of the Riyadh region was discussed in 1422H (2001G) by His Regal Height Sovereign Salman Container Abdulaziz, who then served as the Riyadh Representative and Chairman of the Territorial Board later becoming King of Saudi Arabia in 2015. He encouraged Riyadh Advancement Specialists (ADA) to consider the Territorial Council's requirement to plan more carefully for future development in Riyadh (Fig. 2).

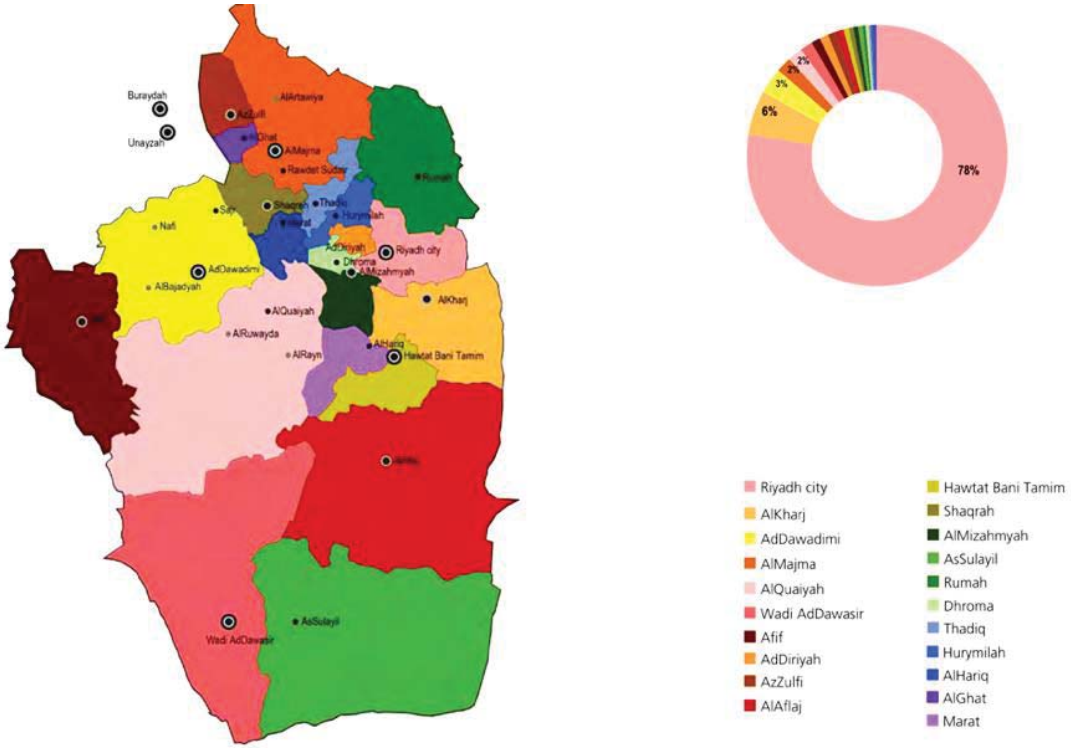

Fig. 2. Riyadh region's governorates [19]

3.1.1 LAND USE

Large tracts of land devoted to residential use only characterize the city of Riyadh, extending outward from the city center, as shown in Fig. 3 [19]. The majority of these neighborhoods lack key facilities, high-quality open spaces, or access to amenities, since there are few mixed-use and commercial properties. The urban structure is consequently unbalanced as a result of the uneven distribution of land use, necessitating longer and additional trips to access services and jobs [19]. In general, the 1450 UGB's built-up area is comprised of 39% more residential land use than non-residential land use. As the capital, Riyadh has a significant portion of its land devoted to governmental and public institutions. A total of 21% of the land inside this boundary is taken up by governmental structures and public buildings. Overall, the city has sparse distribution of commercial, retail, and mixed-use districts. These are primarily grouped along minor roads that enclose residential neighborhoods or a arranged in single-purpose clusters dispersed sporadically across the city, rendered accessible from main highways. The larger proportion of employment, accounts for 11% of the entire built-up urban zone, and is concentrated within the South, influencing the quality of urban life within the adjoining private neighborhoods [19]

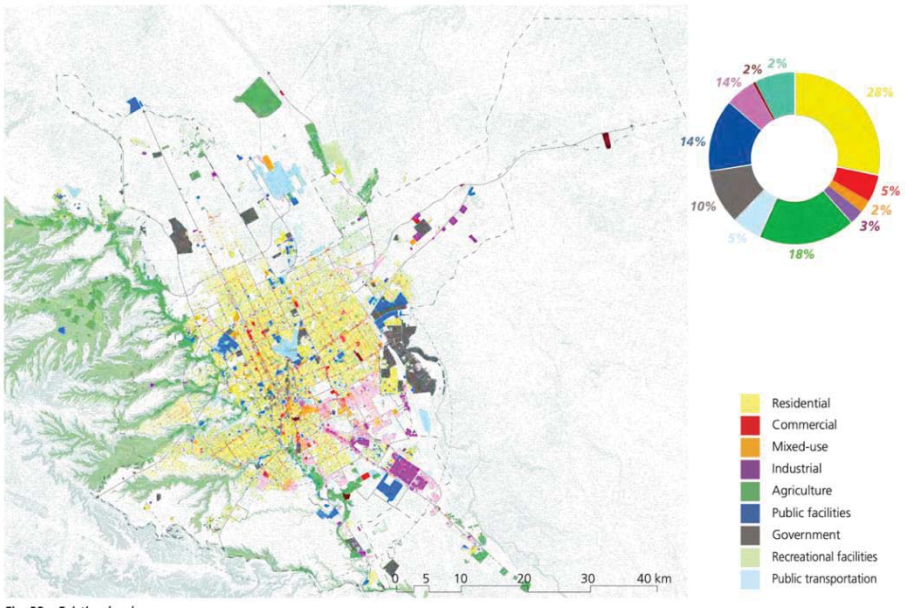

Fig. 3: Land use in Riyadh city [19].

The character of future urban development is likely to be determined by expansion in three primary directions; towards the Southwest, North, and East. The Eastern and Northern expansion areas are proposed as two modern major sub-centers, that will serve as satellites for the central area of the city. Due to there being detached from the rest of the city, and the direct arrangement of these expansions, the arrangement of administrations and integration of the street and transportation foundations will create challenges and is likely to impose a financial strain on the city.

3.1.2 ECOSYSTEM IN RIYADH PROVINCE

The urban character of the city has been determined by geographical features firmly combined with existing environmental structures, such as water channels, parks, and rural lands as shown in Fig. 4 [19]. Over time, the original personality of the city has changed, as original small-scale open spaces within neighborhoods have been neglected, due to the emphasis on

larger scale citywide open spaces at the expense of neighborhood parks. There is a clear need for more open spaces within the existing urban fabric, as the availability of open spaces is currently restricted, with many such areas only accessible via private transport [19].

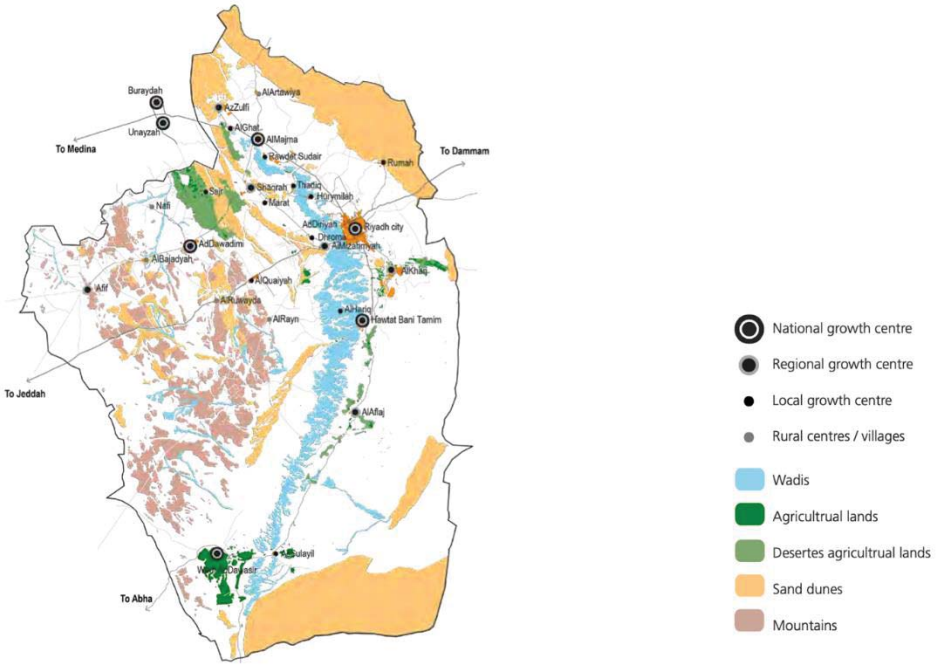

Fig. 4: Eco system in Riyadh province [19].

Travel within the city is primarily by car as Riyadh offers few public transport links to inhabitants. There are plans to develop bus rapid transit and Metro links. Introduction of additional public transport will undoubtedly alter the cityscape and the character of the city, providing an opportunity to coordinate development more efficiently (see Fig. 5) [19].

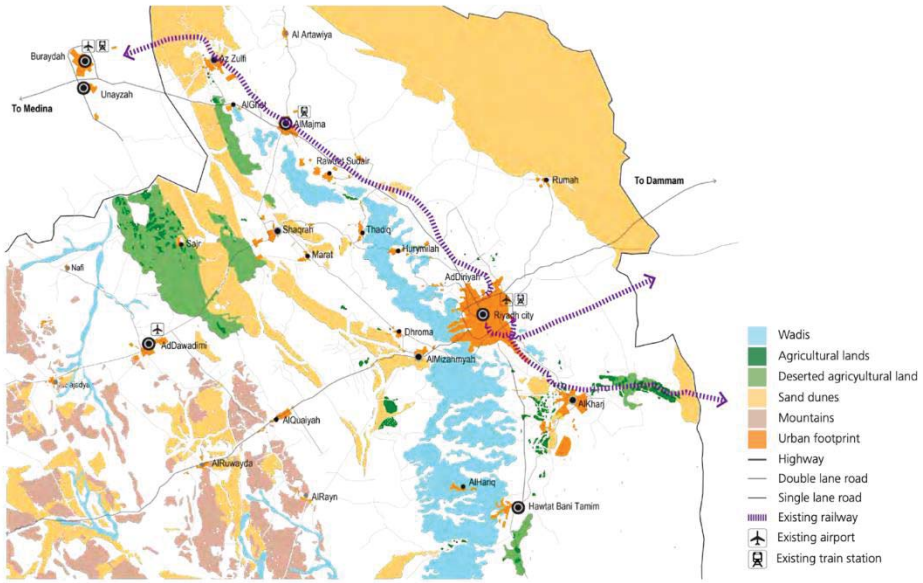

Fig. 5: Transport system within the Riyadh region [19].

3.2 EASTERN REGION

The Jeddah Islamic Port is both the busiest and the second-biggest port in the Middle East and North Africa, with Dammam Port being the largest port in the Arabian Gulf. The King Abdulaziz Port is an important oil industry export hub and is a crucial distribution point for the country's main landlocked towns, especially regional capitals such as Riyadh, which is connected to Dammam by rail link [20]. Fig. 6 details the cities in the Eastern region. This figure also displays the national growth center, regional growth center and local growth center.

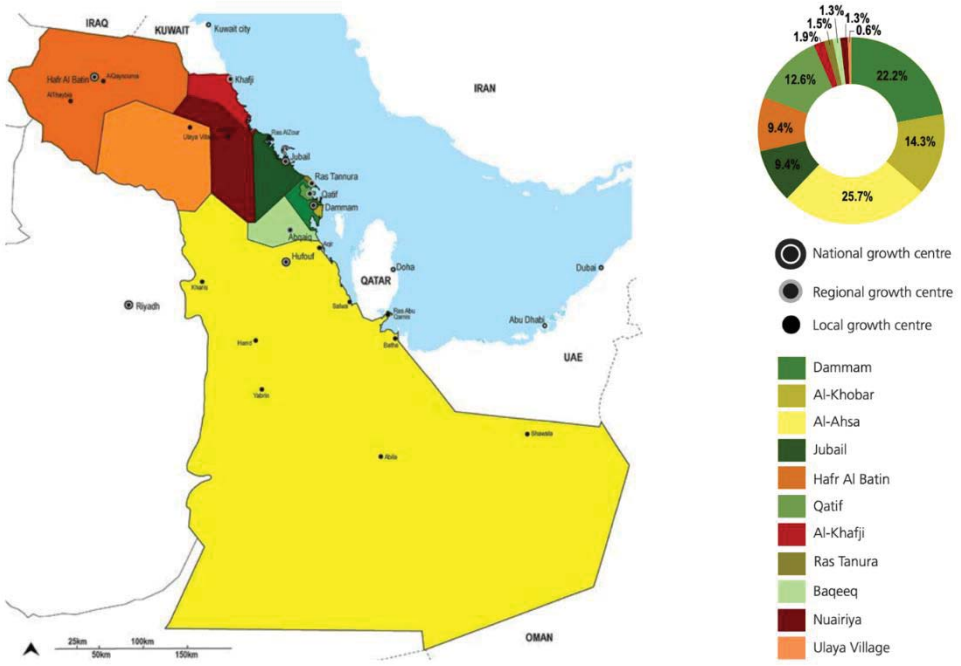

Fig. 6: Eastern region cities and growth centers [20].

3.2.1 LAND USE

Among the five municipalities, the order if significance has remained the same for decades, and it is not expected to alter in the near future. Between 1985 and 2025, Riyadh served as the biggest urban agglomeration after Jeddah, Makkah, Madinah and Dammam. Over the next two decades, Dammam (yet much littler) is anticipated to develop quicker than Jeddah. The development rate per decade for these five main cities has fallen from 82% (1985-1995), to 41% (2000-2010), 18% (2015-2025), following the common pattern observed moreover within auxiliary cities. In the early 1980s Dammam was an isolated city despite its proximity to Al Khobar and Dhahra. However, after a long period of rapid urban development, the three towns became consolidated into one, creating a single urban continuum, known as the Dammam Metropolitan Range. Dammam is the capital of the Eastern Region (one of the 13 province), and it is divided into 11 provinces that are further subdivided into sub-provinces including the traditional Al-Ahsa Oasis and the Empty Quarter Desert, which is the largest province in Saudi Arabia in terms of area. Similar to the other 12 provinces of Saudi Arabia, Dammam is governed by a "municipality" (see Fig. 7).

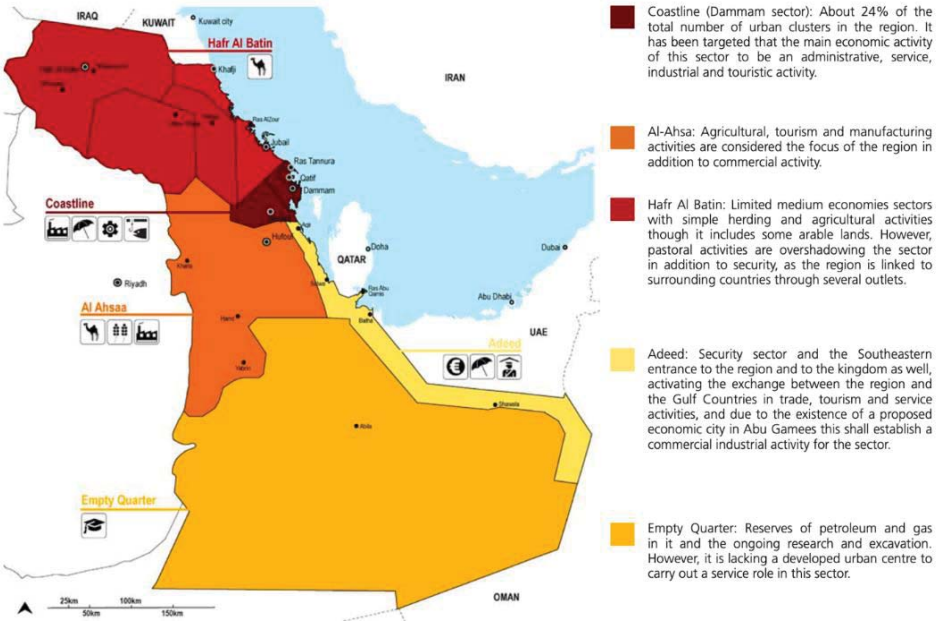

Fig. 7: Eastern region and uses of each province [20].

The city of Dammam is connected to other cities within the region via multiple road links. It is connected to Abqaiq, Dhahran, Al Hofuf, and Jubail by via the Dhahran – Jubail Interstate, and to Khafji, and Al Khobar by means of the Dammam – Khobar Interstate, and to Ras Tanura, Sihat, and Qatif through the Inlet Street (Saudi Arabia), as well as numerous cities in other parts of the Kingdom via eight highways. Dammam is linked to the Saudi capital, Riyadh, and to Jeddah on the West Coast by Thruway 40 and is connected to Bahrain by the 28 kilometer long Lord Fahd Causeway, as depicted in Fig. 8 below [20].

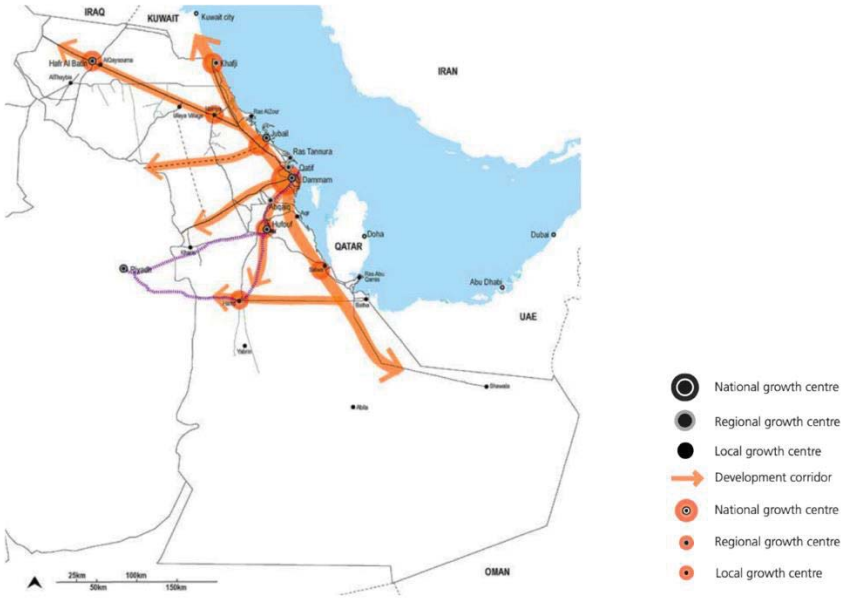

Fig. 8: transportation system in Eastern region [20].

3.2.2 ECOSYSTEM IN THE EASTERN PROVINCE

Saudi Arabia covers 80% of the Arabian peninsula. Environmentally, its structural features include 2,410 km of coastline, 2.7 million hectares of forestland, more than 171 million hectares of grazing land, 35 square kilometers of mangroves and 1,480 square kilometers of coral reefs. The Dammam region is located between the plains and the dunes. The majority of the territory is located at a moderate elevation, with about 50% of the area having an elevation between 0 and 50 meters, which is favorable for urban development [20]. Fig. 9 illustrates the availability of natural resources, including underground water, wades and agricultural areas. These ecosystems are invaluable, not only for their territorial structure, but also as key factors supporting the national economy and people's well-being. Saudi Arabia has the highest population growth rate in the world at 2.6% [20].

This level of population growth can severely impact natural systems, adversely affecting biodiversity and ecosystem dynamics; i.e. research concerning the cities of Damam and Dhahran has identified diverse factors that contribute to environmental degradation. Environmental issues should also be addressed, as unsustainable growth models and inadequate infrastructure is expected to jeopardize future economic development and impair existing natural resources. Meanwhile, climate change places an additional burden on the environment, with growth further fuelled by the fact that Dhahran is one of the richest regions in the world in terms of oil and natural gas. Moreover, in Dammam there are no permanent waterways, and groundwater can be found in aquifers located deep below the surface. The main groundwater sources are the Dammam and Saq aquifers, which contribute to the city's water supply. Overall, the country has a semi-arid to super-arid climate, characterized by very low rainfall and extremely high evapotranspiration. The region also has the lowest freshwater resources in the world, with fossil groundwater from sedimentary aquifers providing agricultural, urban and industrial needs [20].

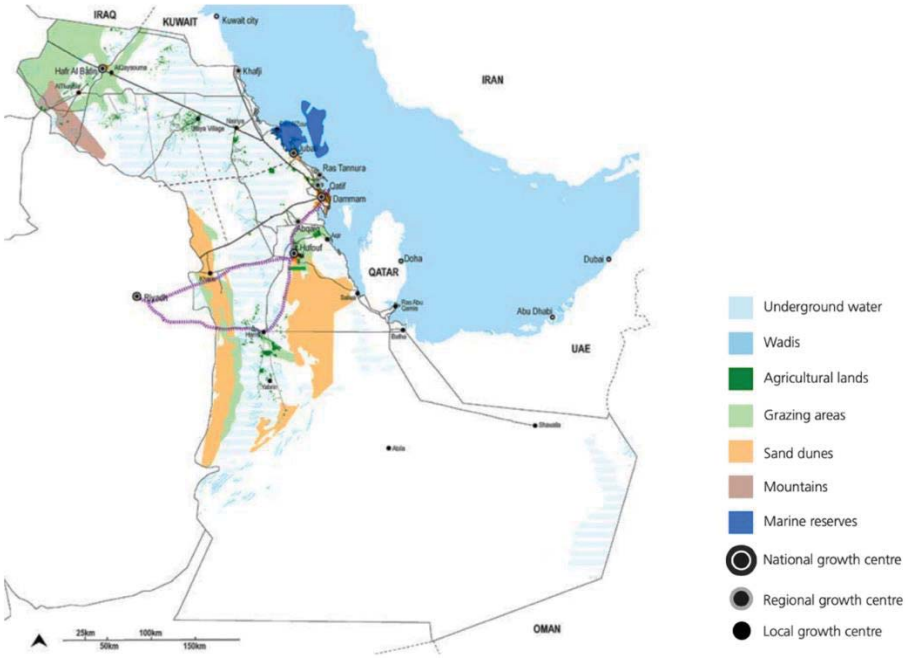

Fig. 9: Ecosystem in Eastern region

3.3 AL-BAHA REGION

The Al-Baha region currently experiences migration of its population to the main cities, or other regions, for the purposes of education or work. However, over the previous ten years, the region has attempted to increase the number of people remaining in the area by establishing a university and a number of other urban facilities. This strategy has proved successful in terms of population retention, but is resulting in urban sprawl within Al-Baha. The Al-Baha region is characterized by its relatively cool climatic conditions and its agriculture [25, 26], while its location and climate have also promoted the development of a successful tourism industry [27, 28]. In addition, relative to the other provinces of Saudi Arabia, the region is rich in natural resources and minerals [29, 30], with tourism and agriculture placing a considerable influence on the local economy. The Al-Baha region contains six main towns, four of which are located in the mountainous areas of the Al-Sarah mountains (i.e. Al-Baha city, Baljurashy, Al-Qara, Al-Aqiq andAl-Mandaq), while two, are located in coastal areas (i.e. Qelwa and Al-Mekhwa). The region also has a number of remote villages, including the Thee Ain Heritage Village [14]. Fig. 10 is a map of the Al-Baha region, including the seven districts, showing two cities (Qelwah and Al-Mekhwah) located in the coastal area of the region [31].

Al-Baha province covers 36,000 square kilometres, or approximately 1.6% of the Kingdom's total land area. Six governorates and the regional principality of Al-Baha comprise the administrative division of the area [21]. The regional “master” plan for Al-Baha province includes a hierarchy of growth centres and development corridors that are used to organize and coordinate future development efforts. Although the proposed corridors are not trans-regional, as was the case with areas such as Makkah or the northern border, they are intended to enhance intra-regional economic potential, which is vital to enhance future opportunities in the region [21].

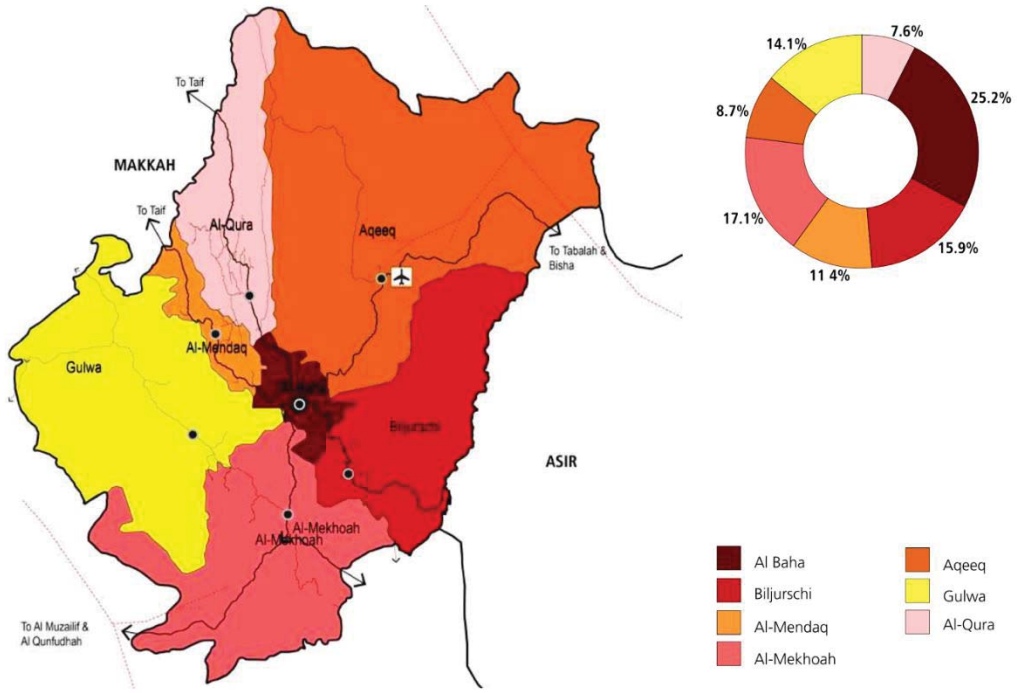

Fig. 10: Map of the Al-Baha region [21]

The primary commercial hubs, light industry hubs, and agricultural production centres in the Al-Baha Region are all connected by the proposed transport corridors. Fig. 11 highlights crucial links to other centres and the planned corridors as set out in the Regional Plan for Al-Baha Region. Al-Baha City serves as the starting point for the region's main growth corridor, continuing northwest connecting to Taif City and providing a significant link to the Taif-Makkah-Jeddah economic and religious corridor. According to the Regional Plan, Al-Baha City serves as a national growth centre, offering services of both regional and national significance, making it a significant economic hub for the area. By maximizing potential in terms of agricultural operations, tourism, and mining, regional growth centres like Aqiq, Al Mendag, Gulwa, and Al Qura, among the other governorate capitals, contribute to the region's revenue. However, the economic links between these centres and Al-Baha City are insufficient to create a city-region; thus, these cities are continuing to mostly function independently [21].

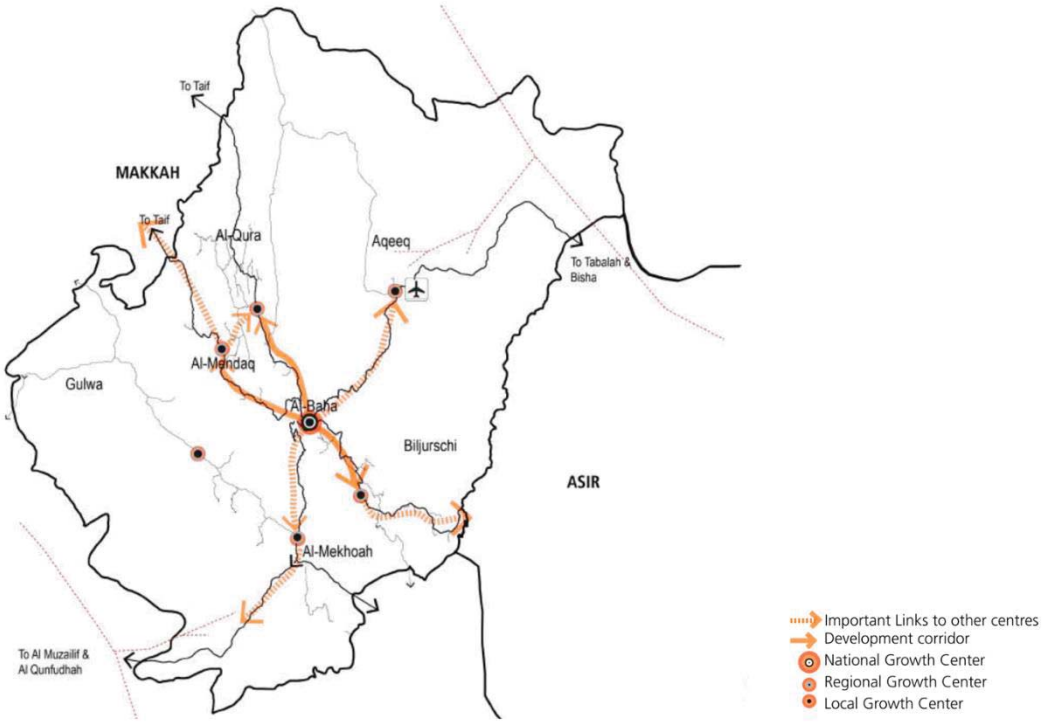

Fig. 11: Existing development corridors according to the Regional Plan for Al-Baha Region [21].

3.3.1 LAND USE

Contemporary developments in terms of land use in the region have been significantly influenced by the topography and morphology of the agricultural land. The majority of the city's territory is also being used for terraced agricultural land, following the natural topography of valleys and mountains. Along with 9% of forested land, agricultural activities occupy around 49% of the total amount of land used [21]. Other land uses are dispersed but harmonious. The main concern relates to the provision of services, particularly providing everyday necessities and specific purposes. The majority of amenities and commercial districts account for 3% of the total land use area, and are situated in the city's core and along its major thoroughfares. Due to the close proximity of these uses, getting

to them is difficult, resulting in lengthy commutes as presented in Fig. 12 [21]. The extent of residential land has increased within the city from 23% to 58%, according to the present land use plan, causing a significant loss of fertile agricultural land. Just 513 hectares, or 5% of the area is currently farmland. The ecosystem's ability to function well might be disrupted by this change [21].

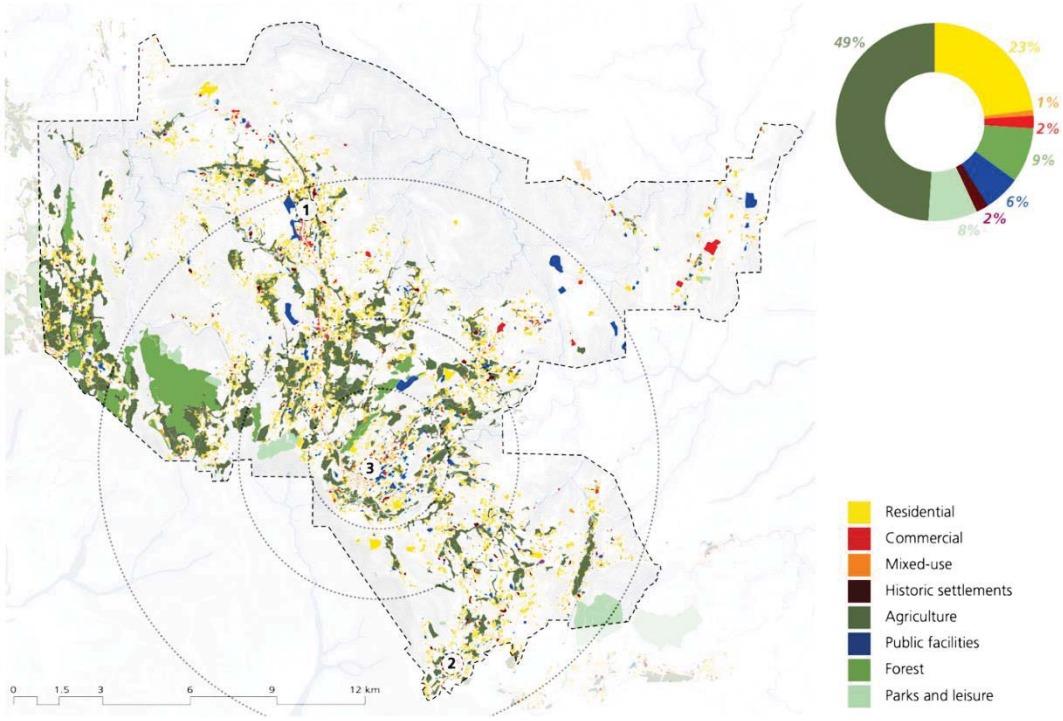

Fig. 12: Land use map for Al-Baha region [21].

3.3.2 ECOSYSTEM IN THE AL-BAHA REGION

According to the ministry of the municipality, it is prohibited to change land use from agricultural uses to residential without approval from the ministry of water and agriculture.

In the Al-Baha Region, agriculture has long been an important economic sector. Its 2.8% contribution to GDP makes it the eighth most important. The area also benefits from major comparative advantages accorded to agricultural production, including improved soil quality, better water quality and availability. However, farming is only permitted using methods that are appropriate to the region's hills and mountains as shown in Fig. 13 [21]. Around 3,400 hectares were planted as crops in 2011, which is approximately 0.4% of the 788,000 hectares planted in crops across the whole Kingdom in that same year.

At the level of the city, Al-Baha's terraced farms follow the natural topography of the mountains and wades. At the local level, grazing pastures are used for agriculture in the northeast of Aqiq and the south of Al Mekhoah. The entire area is known for its pastoral landscape and long-established, and highly skilled sheep farming culture. Additionally, an estimated 5% of the world's honey output comes from the region’s prestigious local honey farms [21].

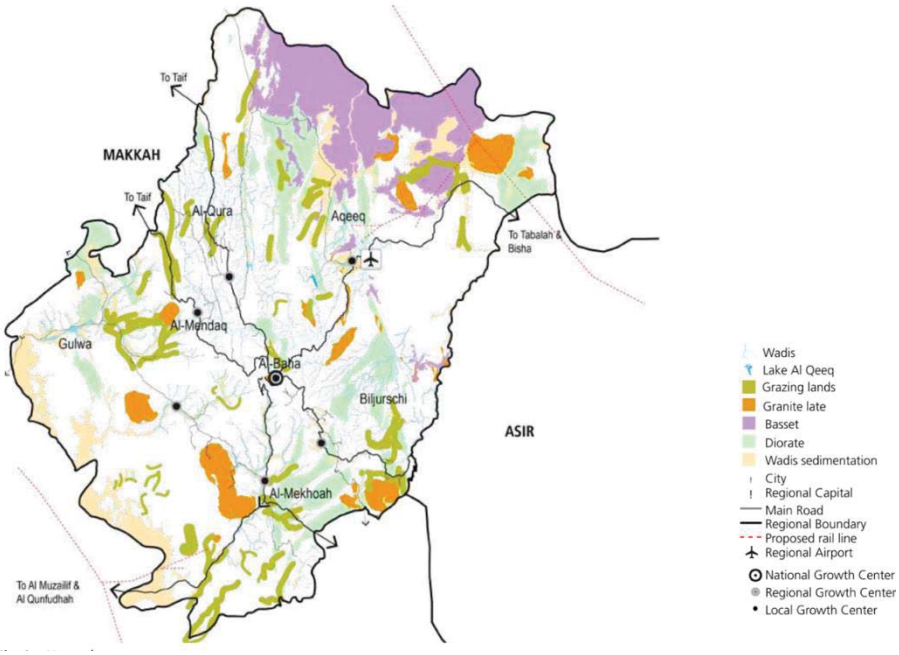

Fig. 13: Ecosystem in Al-Baha region [21]

4. DISCUSSION

The results reported above identified four main factors that promote permanent immigration to the chosen case study regions, as well as a number that determine lead to temporary residences. These factors relate directly to: (1) urban development and growth; (2) application of renewable energy technology; (4) life style; and (5) service and facilities, and are discussed individually in this section, which makes recommendations for future development as presented in Fig. 14 below:

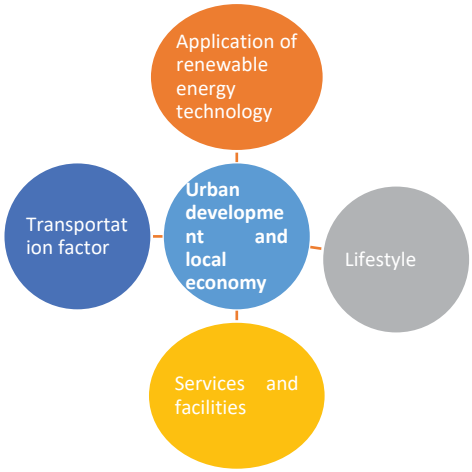

Fig. 14. Urban development in the different three regions

4.1 URBAN DEVELOPMENT STRATEGIES APPLIED IN THE THREE DIFFERENT REGIONS

The results analyzed presented different orientations in terms of the urban strategies applied in the three different regions. This was due to the role of each region, its topography and development. For example, it is clear that Al-Baha region is characterized by forests and wildlife habitats, that are unlike those in the other two regions considered. The benchmarking for urban factors and development is presented in table 3.

Table 3. *Urban strategies applied across the three different regions*

Category	Urban dimension	Riyadh Region	Easter Region	Al-Baha Region
Urban growth	New subdivision plans	√	√	√
	New urban facilities	√	√	√
Public transportation systems	Public trains	√	√	χ
	Local trains system	√	χ	χ
	Public buses	√	√	√
	Local bus system	√	√	χ
Urban challenges	Deserts	√	√	χ
	Mountains	χ	χ	√
	Forests	χ	χ	√

	Wildlife	χ	χ	√
Renewable energy	Encouragement renewable energy strategy	√	√	√
P.V. fields		χ	χ	χ
Wind turbines		√	√	√
Sustainable design reviolations		√	√	√

4.2 ENVIRONMENT AND INTEGRATION

It is vital that urban planners, decision makers and developers address the need to preserve the natural environment within the context of urban growth, including protecting forested areas from urban sprawl, as well as preserving wildlife habitat and minimizing the production of CO2 emissions. The issue of urban growth and development has recently become the subject of popular debate among governmental bodies and decision makers, who wish to establish a future framework to address sprawl in relation to both economic and environmental perspectives [32, 33]. From the mid-twentieth century onwards, the phenomenon of urban development and sprawl has been a topic of interest to specialist researchers [34], prompting extensive examination of key influencers and effects. Contemporary concerns are driving new research and a significantly increased level of participation from scholars and developers [34].

Since the current level of urban sprawl to the Al-Baha region is now resulting in urban sprawl and expanded urban development, there is an urgent need to take steps to preserve the natural ecosystem of the region, which includes determining how to manage urban development most effectively, while at the same time ensuring protection of wildlife, forests and the ecosystem. As discussed previously, Al-Baha is located in the southern western region of Saudi Arabia (41° 42 E, 19° 20 N) among the Makah and Asser regions [35, 36], which are characterized by climatic conditions associated with the impact of urbanization on biodiversity and urban ecosystems [37]. Despite this, many specialist researchers and professionals are interested in developing urban and regional planning to ensure sustainable and resilient towns and cities, highlighting the need to evaluate the broad range of services required by the urban environmental ecosystem [38, 39]. Urban development and growth is regularly characterized as a serious challenge relating to urban land use; one that refers to the extent of urban spread into adjoining remote villages and suburbs, resulting in the unbalancing of ecosystems [40, 41].

At the global scale, urban growth creates both opportunities and challenges for human well-being, resulting in a transition towards urban environmental planning [42]. Urban zones and areas allocated within cities are human environmental systems, which can be impacted by human activities that rely on urban ecosystems. These therefore demand complete understanding of the management of environmental urban ecosystems, so as to achieve the sustainability of environmental urban planning [42].

The Al-Baha region is well known for its wildlife habitats, as well as its forested areas, which are distributed across its mountainous regions. Planners need to ensure its identity is protected from human activities, including the consequences of urban sprawl. Forests are currently suffering from ongoing reduction in the Kingdom of Saudi Arabia, with an alarming rate of degradation having been observed due to factors associated with the natural conditions, as well as anthropogenic activities [43].

This highlights that it is essential when managing urban sprawl to select areas for new subdivisions that avoid any incursion into the forest due to the potential impact on the natural balance of the ecosystem. One concern, as discussed above, is the displacement of monkeys due to human activities, including the rubbish produced by housing, indicating this issue needs to be managed effectively with designated landfill sites appropriately located with a convenient distance of towns. The challenges faced by urban planners, architects and civil engineers include identification of suitable sites for urban sprawl, while avoiding any landcover modifications, as well as using local construction materials to minimize CO2 emissions caused by imported from a considerable distance.

4.3 URBAN AND ECONOMIC DEVELOPMENT

Urban growth leads to the development and sustainability of the local economy, including establishing new businesses, which subsequently became a financial resource for developing towns, alongside additional investment in local resources. Furthermore, economic development and growth is attracting a diverse population at both the district and neighbourhood level,

with a consequent minimizing of any social divide at the urban regional level [44]. Urban sprawl and a growing population is playing a significant role in the local economy, having been recently increased in developing countries [44, 45]. Previous studies have also evaluated urban growth as a negative phenomenon, due to the expectation of associated costs [46, 47]. Nevertheless, many researchers have investigated the influence of urban growth relative to public expenses or fuel consumption, rather than following a more comprehensive approach [46]. There remains a gap in the research concerning the influence of urban growth and sprawl on the local economy from a wider perspective [46]. The expansion of cities and towns is now receiving increased attention from both decision makers and researchers [48].

Urban sprawl in the Al-Baha region will help develop the local economy, due to the establishment of increased job opportunities, as well as new urban facilities and services. A number of urban facilities were established in Al-Baha region between 2006 and 2022, resulting in new jobs, associated with reverse migration, rising demand for housing, alongside increase purchasing power, contributing to the development of local economy.

On the other hand, it is also vital to ensure appropriate investments in facilities for tourism and the entertainment sector, to develop the local economy. Urban heritage has also been protected in Saudi Arabia, with areas such as the Al-Baha region having had their urban identity protected [49]. As the Al-Baha region is well known for its historic villages and heritage facilities, these sites are being be conserved and developed to promote tourism and contribute to the local economy, including by attracting additional investors and developers. Furthermore, government interventions are playing a significant role in determining priorities relating to heritage villages and conservation facilities, as well as exploiting these for tourism-related development [50, 51]. This reflects how heritage villages and historical sites in the Al-Baha region can be conserved and employed as part of the tourism industry. In addition, steps are being taken to improve the development of the local economy, while at the same time protecting heritage, social legacy and urban identity of the area. Moreover, future buildings could use local construction materials, reflecting their urban identity, minimizing embodied energy and reducing CO2 emissions, resulting in increased environmental protection and advancing standards relating to urban environmental and sustainable criteria [52, 53].

5. CONCLUSION AND RECOMMENDATIONS

The paper has examined the factors promoting urban development throughout three different regions in Saudi Arabia in relation to urban development, the provision of facilities to support the population, and the impact of urban development on the natural environment and ecosystem. This study also aimed to identify the response to the establishment of new facilities, including the university, hospitals and other urban facilities based on the local urbanization of the region. To achieve this, the study included a benchmark the urban planning and development with the inhabitants of Riadh region, eastern and Al-Baha region, exploring the issue of urbanization and development. The study also analyzed the factors attracting factories, new residents within the regions while at the same time encourages and develops the local economy. The findings confirmed the most attractive factor in ensuring urban development has been the introduction of new urban educational facilities, factories, life style and employment opportunities. In addition, the study concluded that a variety of urban facilities need to be developed in some remote towns within the region in order to manage urban development; i.e. introducing malls and entertainment facilities. Furthermore, it confirmed the establishment and ports was one of the most effective developments, and contributes in development the economy in the regional and country scales. The study discussed the factors that contribute in urban development resulting from this increase in population in terms of the economic and environmental implications, including the importance of protecting the ecosystem for mountainous regions i.e. Al-Baha region. The study therefore concludes with offering the following recommendations for developers, decision makers and future researchers with regard to urban planning.

5.1 RECOMMENDATIONS FOR DEVELOPERS

It is advised that developers do the following:

- Invest in commercial projects capable of contributing new jobs for the inhabitants of the area to prevent emigration and manage urban sprawl within the region.

- Invest in heritage villages to develop the tourism industry and create new employment opportunities.
- Establish factories to sustain the local economy and invest in local natural resources.
- Invest in entertainment facilities to encourage and develop the local tourism industry and establish new jobs to enhance the local economy.

5.2 RECOMMENDATIONS FOR DECISION MAKERS

It is recommended that decision makers aim to:

- Select sites for new districts to manage future urban sprawl, avoiding forest boundaries to protect the integrity of the ecosystem as a wildlife habitat.
- Establish new urban facilities, including private colleges, hospitals, schools and additional educational facilities, to avoid an exodus of the population.
- Allocate landfill sites for waste disposal at a suitable distance from inhabited areas and the forest.
- Allocate future sustainable neighbourhoods to exploit renewable energy resources in order to protect the environment from CO2 emissions.

5.3 RECOMMENDATIONS FOR FUTURE RESEARCHERS

It is recommended that future researchers do the following:

- Focus on modifications to landcover examining the factors influencing changes in the ecosystem and landcover.
- Focus on the application of on-site renewable energy to fulfil future energy demands while minimizing CO2 emission.
- Focus on the impact of common diseases that could be transferred to humans from the monkey population through increased contact with wildlife.
- Focus on factors that contribute to a lack of balance in the ecosystem as a result of human activities.

6. REFERENCES

[1] Hasan, A., Migration, small towns and social transformations in Pakistan. Environment and Urbanization, 2010. **22**(1): p. 33-50.

[2] Bhagat, R.B. Migration and urban transition in India: Implications for development. in United Nations expert group meeting on sustainable cities. Human mobilities and international migration. 2017.

[3] Hussain, N.H.M., Machine learning of the reverse migration models for population prediction: a review. Turkish Journal of Computer and Mathematics Education (TURCOMAT), 2021. **12**(5): p. 1830-1838.

[4] Al-Hemaidi, W.K., The metamorphosis of the urban fabric in Arab-Muslim city: Riyadh, Saudi Arabia. Journal of Housing and the Built Environment, 2001. **16**(2): p. 179-201.

[5] Abdul Salam, A., et al., Population distribution and household conditions in Saudi Arabia: reflections from the 2010 Census. SpringerPlus, 2014. **3**(1): p. 1-13.

[6] Buckley, R., et al., World heritage tourism triggers urban–rural reverse migration and social change. Journal of Travel Research, 2020. **59**(3): p. 559-572.

[7] Lindkvist, C., et al., Exploring urban facilities management approaches to increase connectivity in smart cities. Facilities, 2020.

[8] Yuan, F., Y.D. Wei, and J. Wu, Amenity effects of urban facilities on housing prices in China: Accessibility, scarcity, and urban spaces. Cities, 2020. **96**: p. 102433.

[9] Artmann, M., et al., The role of urban green spaces in care facilities for elderly people across European cities. Urban forestry & urban greening, 2017. **27**: p. 203-213.

[10] Abubakar, I.R. and U.L. Dano, Sustainable urban planning strategies for mitigating climate change in Saudi Arabia. Environment, Development and Sustainability, 2020. **22**(6): p. 5129-5152.

[11] Bouregh, A.S., et al., Investigating the prospect of e-participation in urban planning in Saudi Arabia. Cities, 2023. **134**: p. 104186.

[12] Mandeli, K.N., The realities of integrating physical planning and local management into urban development: A case study of Jeddah, Saudi Arabia. Habitat International, 2008. **32**(4): p. 512-533.

[13] Khalil, S.A., et al., Assessment of UVB solar radiation in four different selected climate locations in Saudi Arabia. NRIAG Journal of

Astronomy and Geophysics, 2021. **10**(1): p. 125-137.

[14] El-Hawagry, M.S., et al., A preliminary study on the insect fauna of Al-Baha Province, Saudi Arabia, with descriptions of two new species. ZooKeys, 2013(274): p. 1.

[15] Mahmoud, S.H., F. Mohammad, and A. Alazba, Determination of potential runoff coefficient for Al-Baha Region, Saudi Arabia using GIS. Arabian Journal of Geosciences, 2014. **7**(5): p. 2041-2057.

[16] Almulhim, A.I. and P.B. Cobbinah, Urbanization-environment conundrum: an invitation to sustainable development in Saudi Arabian cities. International Journal of Sustainable Development & World Ecology, 2023. **30**(4): p. 359-373.

[17] Giddens, J.F., M. Wright, and I. Gray, Selecting concepts for a concept-based curriculum: Application of a benchmark approach. Journal of Nursing Education, 2012. **51**(9): p. 511-515.

[18] Fernandez, P., I.P. McCarthy, and T. Rakotobe-Joel, An evolutionary approach to benchmarking. Benchmarking: An International Journal, 2001. **8**(4): p. 281-305.

[19] Anne Eilenberg, H.S.A., Costanza La Mantia, Rama Nimri, Anne Klen-Amin, Samuel Njuguna, Faisal Bin Sulaiman, Giuseppe Tesoriere, Elizabeth Glass, Mazen Mokhtar, Solomon Karani Future Saudi Cities Programme: City Profiles Series: Riyadh, in Ministry of Municipal and Rural Affairs, King Fahd National Library Cataloging-in-publication Data. 2019.

[20] Anne Eilenberg, H.S.A., Costanza La Mantia, Rama Nimri, Anne Klen-Amin, Samuel Njuguna, Faisal Bin Sulaiman, Giuseppe Tesoriere, Elizabeth Glass, Mazen Mokhtar, Solomon Karani Future Saudi Cities Programme City Profiles Series: Dammam. Ministry of Municipal and Rural Affairs; King Fahd National Library Cataloging-in-publication Data, 2019.

[21] Anne Eilenberg, H.S.A., Costanza La Mantia, Rama Nimri, Anne Klen-Amin, Samuel Njuguna, Faisal Bin Sulaiman, Giuseppe Tesoriere, Elizabeth Glass, Mazen Mokhtar, Solomon Karani, Future Saudi Cities Programme City Profiles Series: Al Baha. Ministry of Municipal and Rural Affairs; King Fahd National Library Cataloging-in-publication Data, 2019.

[22] Al-Hathloul, S., Riyadh development plans in the past fifty years (1967-2016). Current Urban Studies, 2017. **5**(01): p. 97.

[23] Mubarak, F.A., Urban growth boundary policy and residential suburbanization: Riyadh, Saudi Arabia. Habitat international, 2004. **28**(4): p. 567-591.

[24] Alotaibi, O. and D. Potoglou, Introducing public transport and relevant strategies in Riyadh City, Saudi Arabia: A stakeholders' perspective. Urban, Planning and Transport Research, 2018. **6**(1): p. 35-53.

[25] Al-Robai, S.A., et al., Vegetation structure and species diversity of Wadi Turbah Zahran, Albaha area, southwestern Saudi Arabia. Annals of Agricultural Sciences, 2017. **62**(1): p. 61-69.

[26] Al-Zahrani, K.H., et al., Biological yields through agricultural extension activities and services: A case study from Al-Baha region–Kingdom of Saudi Arabia. Saudi Journal of Biological Sciences, 2021. **28**(5): p. 2789-2794.

[27] Alsumairi, M. and K.W.H. Tsui, A case study: The impact of low-cost carriers on inbound tourism of Saudi Arabia. Journal of Air Transport Management, 2017. **62**: p. 129-145.

[28] Bokhari, A., Understanding Tourists' Motivations: The Case of Al Baha Mountainous Region in Saudi Arabia. International Journal of Environmental Science & Sustainable Development, 2021. **6**(1): p. 75-87.

[29] Al-Barakah, F.N., et al., Comparison and hydrochemical characterization of groundwater resources in the Arabian Peninsula: A case study of Al-Baha and Al-Qassim in Saudi Arabia. Water Resources, 2020. **47**(5): p. 877-891.

[30] Alghamdi, A.G., et al., Impact of climate change on hydrochemical properties and quality of groundwater for domestic and irrigation purposes in arid environment: A case study of Al-Baha region, Saudi Arabia. 2022.

[31] El-Hawagry, M.S., et al., Addenda to the insect fauna of Al-Baha Province, Kingdom of Saudi Arabia with zoogeographical notes. Journal of Natural History, 2016. **50**(19-20): p. 1209-1236.

[32] Johnson, M.P., Environmental impacts of urban sprawl: a survey of the literature and proposed research agenda. Environment and planning A, 2001. **33**(4): p. 717-735.

[33] Banai, R. and T. DePriest, Urban sprawl: Definitions, data, methods of measurement, and environmental consequences. Education, 2010. **7**.

[34] Rubiera-Morollón, F. and R. Garrido-Yserte, Recent literature about urban sprawl: A renewed relevance of the phenomenon from the perspective of environmental sustainability. Sustainability, 2020. **12**(16): p. 6551.

[35] Mahmoud, S.H. and A. Alazba, Land cover change dynamics mapping and predictions using EO data and a GIS-cellular automata model: the case of Al-Baha region, Kingdom of Saudi Arabia. Arabian Journal of Geosciences, 2016. **9**(5): p. 1-20.

[36] Ibrahim, M.M., Study of cystic echinococcosis in slaughtered animals in Al Baha region, Saudi Arabia: interaction between some biotic and abiotic factors. Acta Tropica, 2010. **113**(1): p. 26-33.

[37] Sanford, M.P., P.N. Manley, and D.D. Murphy, Effects of urban development on ant communities: implications for ecosystem services and management. Conservation Biology, 2009. **23**(1): p. 131-141.

[38] Ahern, J., S. Cilliers, and J. Niemelä, The concept of ecosystem services in adaptive urban planning and design: A framework for supporting innovation. Landscape and Urban Planning, 2014. **125**: p. 254-259.

[39] Gómez-Baggethun, E., et al., Urban ecosystem services, in Urbanization, biodiversity and ecosystem services: Challenges and opportunities. 2013, Springer, Dordrecht. p. 175-251.

[40] Colding, J., The role of ecosystem services in contemporary urban planning. 2011.

[41] Haase, D., et al., A quantitative review of urban ecosystem service assessments: concepts, models, and implementation. Ambio, 2014. **43**(4): p. 413-433.

[42] Luederitz, C., et al., A review of urban ecosystem services: six key challenges for future research. Ecosystem services, 2015. **14**: p. 98-112.

[43] El-Juhany, L.I., Forestland degradation and potential rehabilitation in southwest Saudi Arabia. Australian Journal of Basic and Applied Sciences, 2009. **3**(3): p. 2677-2696.

[44] Di Feliciantonio, C., et al., Class diversification, economic growth and urban sprawl: Evidences from a pre-crisis European city. Quality & Quantity, 2018. **52**(4): p. 1501-1522.

[45] Yigitcanlar, T. and M. Bulu, Dubaization of Istanbul: Insights from the knowledge-based urban development journey of an emerging local economy. Environment and Planning A, 2015. **47**(1): p. 89-107.

[46] Lityński, P., The correlation between urban sprawl and the local economy in Poland. Urbani izziv, 2016. **27**(2): p. 86-96.

[47] Wu, J., Environmental amenities, urban sprawl, and community characteristics. Journal of Environmental Economics and Management, 2006. **52**(2): p. 527-547.

[48] Weilenmann, B., I. Seidl, and T. Schulz, The socio-economic determinants of urban sprawl between 1980 and 2010 in Switzerland. Landscape and Urban Planning, 2017. **157**: p. 468-482.

[49] Bokhary, A. S., & Mohamed Hammad, M. T. (2020). ROOTING THE ARCHITECTURAL VALUES OF HERITAGE IN THE CONTEMPORARY ARCHITECTURE (AN ANALYTICAL STUDY OF THE ARCHITECTURE HERITAGE AT AL-BAHA IN THE KINGDOM OF SAUDI ARABIA IN ORDER TO BE STABILIZEDWITHIN THE CONTEMPORARY ARCHITECTURE). Journal of Al-Azhar University Engineering Sector, 15(54), 297-314.

[50] Wang, Y. and B. Bramwell, Heritage protection and tourism development priorities in Hangzhou, China: A political economy and governance perspective. Tourism Management, 2012. **33**(4): p. 988-998.

[51] Kakiuchi, E., Cultural heritage protection system in Japan: current issues and prospects for the future. National Graduate Institute for Policy Studies, 2014. **2**: p. 1-12.

[52] Ali, A., et al. Vernacular and Modern Building: Estimating the CO2 emissions from the building materials in Egypt. in Building Simulation Conference, Cairo, Egypt. 2013.

[53] Ji, C., T. Hong, and H.S. Park, Comparative analysis of decision-making methods for integrating cost and CO2 emission–focus on building structural design–. Energy and Buildings, 2014. **72**: p. 186-194.

Jouf University Science and Engineering Journal (JUSEJ) 2023; 10(2): 29- 38
Published online: Dec. 2023 (https://www.ju.edu.sa/en/jouf-university-science-and-engineering-journal-jusej/home/)
Print ISSN: 1658-6670 ***Electronic ISSN:1658-9173 (1443/5074)***

Water Cycle Approach Based Load Frequency Controller for Renewable Energy Resources Combined Heat Power Network

Ehab Salim Ali [1*]

[1] Department of Electrical Engineering, College of Engineering, Jazan University, Jazan, Kingdom of Saudi Arabia

***Corresponding author**

Ehab Salim Ali

Email address:

esalama@jazanu.edu.sa

Submission Date: *May 22, 2023*
Accepted Date: *Sept. 17, 2023*

Load Frequency Control (LFC) is complicated widely in multiple areas linked power framework due to the growing permeation of renewable energy resources, like Photovoltaic (PV) cells and wind turbine. This paper suggests a fresh optimization tool called as Water Cycle Approach (WCA) for optimum regulation of Proportional added to Integral added to Derivative)PID(controller for LFC. The task of tuning of PID robustly based LFC layout is constructed as an optimization case based on the time scope charge equation, which is handled by the suggested approach. WCA owns a vigorous capability to detect the most hopeful outcomes. The schematic diagram of the composite framework is executed. Simulation outcomes are organized to investigate the reinforced attitude of the advised WCA based the developed controller compared with Ant Lion Optimizer (ALO), Firefly Approach (FA), and Genetic Approach (GA). These outcomes give that the developed controllers introduce better attitude above others by examining the time characteristic and distinct indicators..

Keywords: *WCA; LFC; PID; Two Zones System; PV grid*

1. INTRODUCTION

The fundamental topical of LFC is to ensure the frequencies and the power of inter area tie line during sensible limits to transact with the variation of disturbances and loads [1]. This prime objective is concerning with LFC case due to the truth that an exemplary destined electric network could continue voltages and frequencies in classified boundary whilst presuming an agreeable weight of system goodness [2].

Distinct approaches had been utilized to the process of LFC. Sturdy shape [3-4], decentralized control [5], linear quadratic [6], pole shifty [7] and changing framework [8] are used to LFC layout. However, these approaches possess diverse demerits which lessen their fulfilment. To push through these hurdles, distinct papers have exercised artificial technique like Fuzzy Logic (FL) [9-10] and Neural Network (NN) [11]. Though the artificial techniques were efficacious in handling the nonlinearity of the electric power network, they possess several demerits. For instance, NN hurts from stating the figure of neurons and layers while, FL necessitates a drastic mission to secure the operative inputs.

Second path is to exercise Evolutionary Approach (EA). EA has the ability to handle the LFC process due to its capability to resolve nonlinear complex equalizations. Genetic Approach (GA) [12], Particle Swarm Optimizer (PSO) [13-14], Bacteria Foraging [15-16], Firefly [17], Gravitational Search [18], Cuckoo Search Approach [19], Bat Approach [20], Ant-Lion Optimizer (ALO) [21-22], Whale Optimization Approach [23-26], Crow Search Approach [27-28], Differential Evolution (DE) [29], and Marine Predator Approach [30] are addressed with LFC layout. Though these approaches imitate to

be efficacious for the layout issue, they distress from delayed congregation and soft regional investigation strength that fabricate them trick in regional minimum.

Water Cycle Approach (WCA) is a novel metaheuristic and population-based seeking tool that imitates the activity of the water rotation on the Earth's exterior. It is extra efficacious for resolving compelled optimization tasks and it is extra dynamic compared with the other population and stochastic-based approaches discussed in brief [31]. Various applications for WCA tuned controller parameters are found in [32-35], they show more robust and superior stabilization. Application of WCA in LFCs has not been examined in the modern review. Also, its ability and effectiveness to keep an equilibrium among the phases of exploration and exploitation motivated the investigators to arrange WCA for the optimum setting of PID based LFC problem in this article.

This article offers a novel optimization approach called as WCA for the best setting of PID constants in LFC case for heat grid joined with solar network. The intent of this study is to prove the efficiency of WCA based PID, and to ameliorate the attitude of frequency variation and the power of tie line under distinct events.

2. SYSTEM UNDER STUDY

Zone 1 is a heat grid that includes of turbine, supply, reheater and governor. The constants of the studied framework are appeared in appendix. The equations of distinct transfer functions are given as following [36]:

The equalization of governor can be stated as:

$$\frac{K_{go}}{T_{go}S+1} \tag{1}$$

The equalization of reheater can be stated as:

$$\frac{K_{re}T_{re}S+1}{T_{re}S+1} \tag{2}$$

The equalization of steam turbine can be stated as:

$$\frac{K_{tu}}{T_{tu}S+1} \tag{3}$$

and the equalization of dynamo can be stated as:

$$\frac{K_{d}}{T_{d}S+1} \tag{4}$$

For the i^{th} zone, the signals Area Control Error (ACE) consist of the divergences of tie-line power and frequency shall be written as:

$$ACE_i = B.\Delta._i + \Delta Ptie_i \tag{5}$$

The solar grid paradigm is collected of solar current supply that is instantly comparative with the sunlight strength shunt with a diode and a short series touch resistor. The product voltage and current from the cell is following to the demand working period. The arithmetical styling of PV cell is displayed in [17]. The block graph of the considered network is shown in Fig. 1. The variation in temperature and radiation are shaped like the unit step function in the solar grid.

For the considered network, the conventional integral block can be displaced by the PID block as appeared by the next equalization:

$$K_i(S) = K_{Pi} + \frac{K_{Ii}}{S} + SK_{Di} \tag{6}$$

The signal of control is displayed by equalization:

$$U_i(S) = -K_i(S)\ ACE_i(S) \tag{7}$$

A certain attitude indicator shall be realized by the Integration of Time multiply Absolute Error (ITAE) of the variation of frequencies for two zones and the power of tie line [37]. Appropriately, the designed cost equalization **J** is adjusted to be

$$\mathbf{J} = \int_0^{\infty} t\left(\left|\Delta f_1\right| + \left|\Delta f_2\right| + \left|\Delta P_{tie}\right|\right)dt \tag{8}$$

To ameliorate the outputs of considered system, it is substantial to diminish equalization (8). The layout mission may be modeled as the next limited optimization process. Lessen **J** vulnerable to:

$$K_{Pi}^{lower} \le K_{Pi} \le K_{Pi}^{upper},$$
$$K_{Ii}^{lower} \le K_{Ii} \le K_{Ii}^{upper},$$
$$K_{Di}^{lower} \le K_{Di} \le K_{Di}^{upper} \tag{9}$$

The borders of the selected values are [-2 to 2] as presented in [17, 22] and the developed cost equalization are considered under 0.1 trouble in every zone.

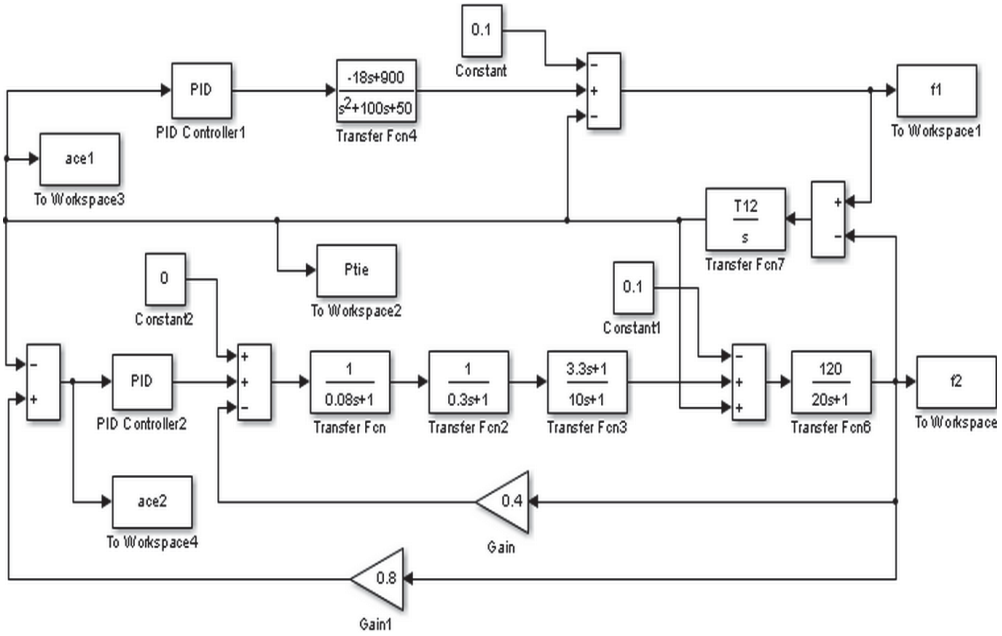

Fig. 1. The graph of the considered network.

3. WATER CYCLE APPROACH

WCA is a novel approach based metaheuristic optimization approaches that various papers are concentrating on, particularly for limited engineering optimization cases. The growth of this approach, established by [31], was stimulated by the status of the water period on the exterior of Earth. Then, this algorithm has developed implementations in various scopes. However, the achievement of the WCA in electric system control has not been considerable until now. This inspired the researcher in this article to apply this checking approach to get the optimum values of PID based LFC to adjust the frequency and preserve the stabilization of connected electric power network.

The examination plan of the WCA begins with a premier population of snowflakes or raindrops that squash on mountains or hills and later as a group shift downhill to shape rivers and streams. Latterly, these rivers and streams are supposed to be associated at the sea, handled as the comprehensive superior output.

For a resolution with fluctuating values 1 x N_{var}, the rain drops vector (RD) is contrived as

$$RD_j = Y_j = [y_1, y_2, \ldots\ldots, y_{N_{var}}] \quad (10)$$

$$RD_{Population} = \begin{bmatrix} RD_1 \\ -- \\ RD_j \\ -- \\ RD_{N_{Pop}} \end{bmatrix} \quad (11)$$

After realizing the premier population, the charge of an individual RD is estimated taking into account the purposed objective indicator of ITAE, as formed in equalization (8).

Thence, the sites (P) of streams and rivers are modernized, as given in neutralizations (12) and (13), relied on the hypothesis that these combine eventually at the sea.

$$P_{stream}^{new} = P_{stream} + \text{rand}(). C. (P_{river} - P_{stream}) \quad (12)$$

$$P_{river}^{new} = P_{river} + \text{rand}(). C. (P_{sea} - P_{river}) \quad (13)$$

The amount C is fixed and is produced at random, having an amount lying among 0 and 2, whereas rand( ) has an amount among 0 and 1. If the estimated performance indicator amount of the stream occurs to be less than that of the river, then the locations of the river and stream can be alternated. An identical case is exercised for river and the sea.

To simplify area for rainwater in the sea, the optimization approach is worked with a vaporization phase for seawater. Furthermore, this cycle shall avert fast congregation and convey prime ability to the screening mechanics. The stage of vaporization concludes if

$$\left|P_{sea} - P_{river}\right| \prec d_{upper} \quad (14)$$

Where d_{upper} is a figure near to zero that diminishes impulsively like

$$d_{upper}^{new} = d_{upper} - (d_{upper}/\text{upper. generation}) \quad (15)$$

The period of rain begins promptly subsequent to the ending of the vaporization procedure. Novel streams will be composed during rain at various sites, and their locations are given by the next equalization:

$$P_{stream}^{new} = P_{sea} + \sqrt{U} * \text{rand}(1, N_{var}) \quad (16)$$

Where U shows the average of inspection near to the sea. The technique offers the universal superior resolution when it arrives
the ultimate generation counting. The parametric amounts applied while layout the suggested WCA for electric power network optimization are given in appendix

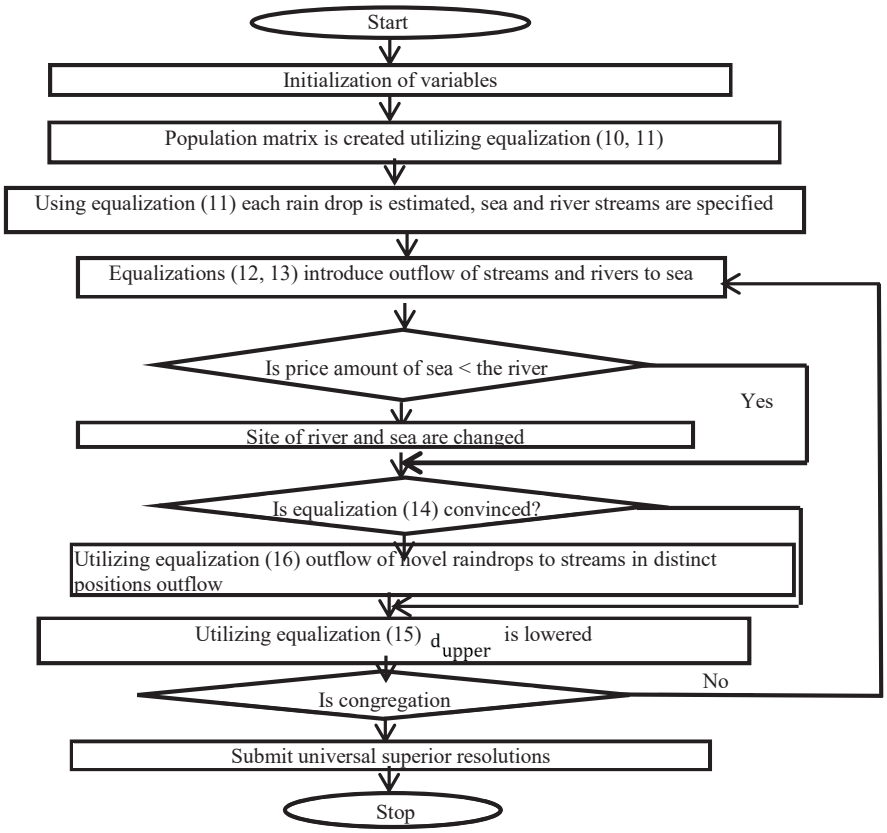

Fig. 2. Displays the flowchart of WCA [31]

4. RESULTS AND DISCUSSION

Distinct events are tested to assert the durability of the mentioned WCA for optimum electing PID values. The developed WCA [32] is schemed in MATLAB 7.1. The given outcomes are the superior for whole approaches relying on amount of J. The amounts of whole controllers and the rates of diverse indicators are displayed in Table (1).

4.1 CASE 1: STEP VARIATION IN LOAD OF HEAT NETWORK

A 0.1 step increment in load of thermal grid is employed. Figures (3-5) give the network reactions. It is evident that, the prepared PIDs are more vigorous in enhancing the alleviation features of electric power network in comparison with ALO, FA, and GA. Thence, WCA shows superior outcomes than others.

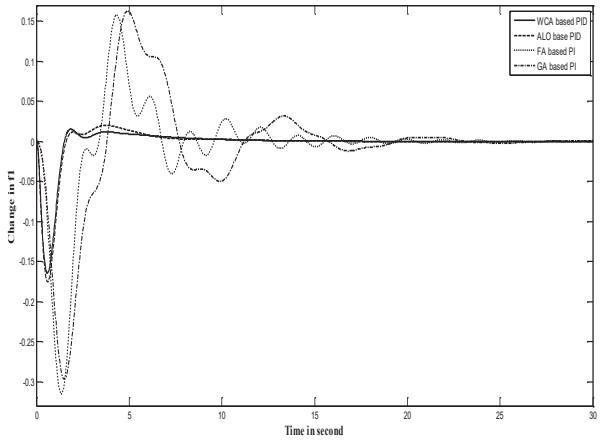

Fig. 3. Variation in f_1 for first case.

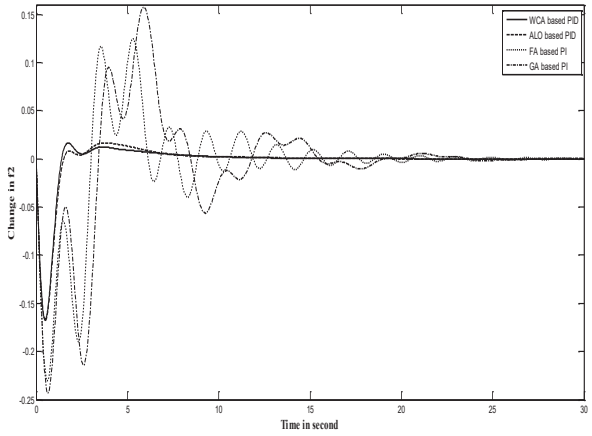

Fig. 4. Variation in f_2 for first case.

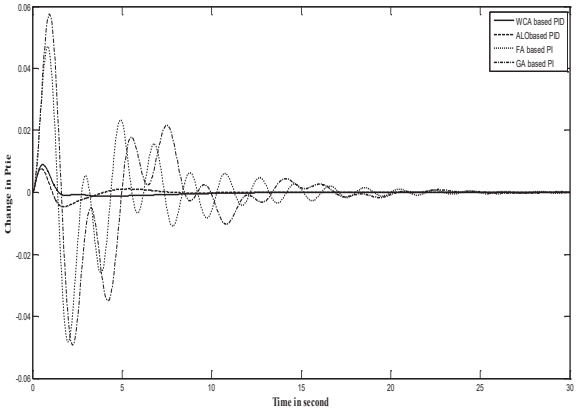

Fig. 5. Variation in P_{tie} for first scenario.

4.2 CASE 2: STEP VARIATION IN BOTH ZONES

In this case, a 0.1 step growing in load of heat grid and temperature and radiation and of solar grid is used. Figures (6-8) present the outputs of the closed loop network. In these Shapes, the network fluctuations are mitigated with the suggested PIDs. Furthermore, the developed PIDs possess a minimal settlement time contrasted with ALO, FA, and GA and network reaction is achieved rapidly the steady state. Moreover, the strength of the layout approach is evidenced in resolving LFC issue.

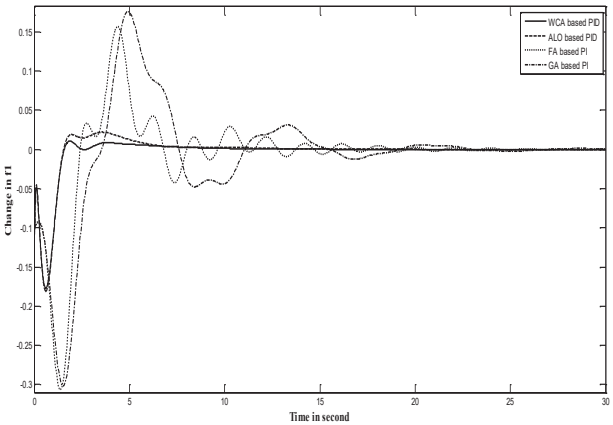

Fig. 6. Alteration in f_1 for second scenario.

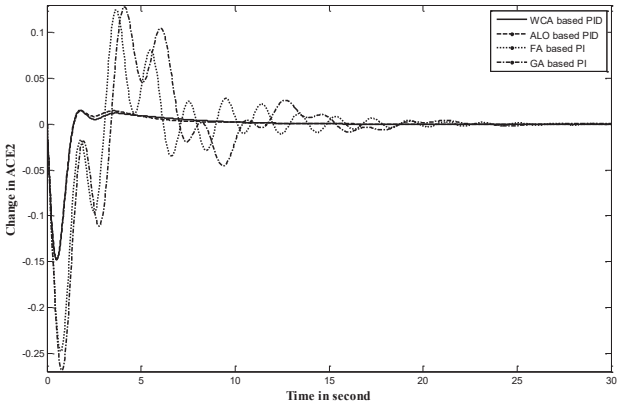

Fig. 7. Variation in f_2 for second scenario.

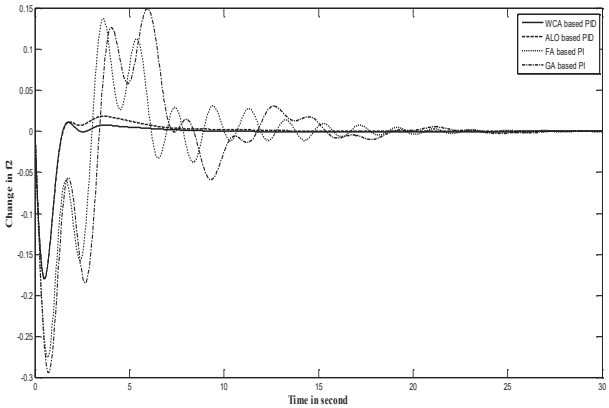

Fig. 8. Variation in ACE_2 for second scenario.

4.3 PERFORMANCE INDICATORS AND ROBUSTNESS

The nobleness of the developed PIDs is confirmed via distinct indicators like the Integration of Absolute amount of the Error (IAE), ITAE, the Integration of Square Error (ISE) and the Integration of Time multiply Square Error (ITSE):

$$IAE = \int_0^{30} \left(\left|\Delta f_1\right| + \left|\Delta f_2\right| + \left|\Delta P_{tie}\right| \right) dt, \quad (17)$$

$$ITAE = \int_0^{30} t \left(\left|\Delta f_1\right| + \left|\Delta f_2\right| + \left|\Delta P_{tie}\right| \right) dt. \quad (18)$$

$$ISE = \int_0^{30} \Delta f_1^2 + \Delta f_2^2 + \Delta P_{tie}^2 \, dt \quad (19)$$

$$ITSE = \int_0^{30} t \left(\Delta f_1^2 + \Delta f_2^2 + \Delta P_{tie}^2 \right) .dt \quad (20)$$

Table 1 assigns the constants of every PID, whilst the amounts of distinct indicators are shown in Table 2. It is obvious that, the amounts of these indicators with the developed PIDs are minimal contrasted with these of WOA [38], MWOA [38], SHO [38], FA [17], and GA [17]. This proves that the time scope features are diminished extremely by utilizing the developed WCA. Thence, the resolved controllers through WCA are more vigorous and quicker than others.

Table. 1. *The constants of various approaches*.

Controller constants	FA adjusted PI [17]	GA adjusted PI [17]	ALO adjusted PID [22]	WCA
K_{P1}	-0.8811	-0.5663	-1.999	-0.86
K_{I1}	-0.5765	-0.4024	-1.973	-0.129
K_{D1}	0	0	-1.9953	-1.94
K_{P2}	-0.7626	-0.5127	-2	-2
K_{I2}	-0.8307	-0.7256	-2	-2
K_{D2}	0	0	-1.4618	-0.261

Table. 2. *The performance indices for various approaches*

Algorithm	IAE	ITAE	ISE	ITSE
GA tuned PI [17]	2.3341	12.1244	0.3202	0.8618
FA tuned PI [17]	1.7207	7.4259	0.2907	0.4723
WOA tuned PI [38]	1.0566	4.1211	0.1663	0.4262
SHO tuned PI [38]	0.6491	2.5308	0.1021	0.26179
MWOA tuned PID [38]	0.5625	1.5602	0.0815	0.0601
SHO tuned PID [38]	0.3091	0.8582	0.0448	0.0369
Proposed WCA	0.2997	0.8492	0.0409	0.0328

5. CONCLUSION

In this article, the optimal constants of PID controller are selected by WCA for LFC issue. Solar grid at MPPT is taken into account and joined to heat grid. An Integration of time absolute error of the change of frequencies for jointly zones and the power of tie line is possessed as the developed charge equalization to ameliorate the network reaction. The seniority of the suggested technique is purified by utilizing distinct disruptions, and distinct indices. It is obvious that, WCA outperforms ALO, FA, and GA in resolving LFC process. Also, the sublimity of the suggested PIDs is confirmed by examining of distinct indicators.

6. REFERENCES

[1] M. Abdillah, R. H. Pratama, N. L. Pertiwi, and H. Setiadi, "Retired Electric Vehicle Battery To Reduce The Load Frequency Control Oscillation in the Micro Grid System", *Indonesian Journal of Electrical Engineering and Computer Science*, Vol. 28, No. 3, 2022, pp.1266-1275, http://doi.org/10.11591/ijeecs.v28.i3.pp1266-1275.

[2] N. Zendehdel, and D. Bustan, "An Open-Source Active Power Controller for Grid Required Ancillary Services", *Telkomnika Telecommunication Computing Electronics and Control*, Vol. 20, No. 3, 2022, pp. 691-698.

[3] W. Tan, and Z. Xu, "Robust Analysis and Design of Load Frequency Controller for Power Systems", *Electric Power Systems Research*, Vol. 79, Issue 5, May 2009, pp. 846-853, https://doi.org/10.1016/j.epsr.2008.11.005.

[4] W. Tan, and H. Zhou, "Robust Analysis of Decentralized Load Frequency Control for Multi-Area Power Systems", *Int. J. of Electrical Power and Energy Systems*, Vol. 43, Issue 1, Dec. 2012, pp. 996-1005, https://doi.org/10.1016/j.ijepes.2012.05.063.

[5] S. Selvakumaran, S. Parthasarathy, R. Karthigaivel and V. Rajasekaran, "Optimal Decentralized Load Frequency Control in a Parallel AC-DC Interconnected Power System Through HVDC Link Using PSO Algorithm", *Energy Procedia*, Vol. 14, 2012, pp. 1849-1854, https://doi.org/10.1016/j.egypro.2011.12.1178.

[6] S. K. Pandey, S. R. Mohanty, N. Kishor, and J. P. S. Catalão, "An Advanced LMI-Based-LQR Design for Load Frequency Control of an Autonomous Hybrid Generation System", *Technological Innovation for the Internet of Things*, *IFIP Advances in Information and Communication Technology*, Vol. 394, 2013, pp. 371-381, https://doi.org/10.1007/978-3-642-37291-9_40.

[7] N. Hasan, "Design and Analysis of Pole-Placement Controller for Interconnected Power Systems", *Int. J. of Emerging Technology and Advanced Engineering*, Vol. 2, Issue 8, Aug. 2012, pp. 212-217, https://www.ijetae.com/files/Volume2Issue8/IJETAE_0812_34.pdf.

[8] E. Awada, E. Radwan, and M. Nour, "Robust Sliding Mode Controller for Buck DC Converter in Off-Grid Applications", *Bulletin of Electrical Engineering and Informatics*, Vol. 11, No. 5, 2022, pp. 2425-2433, http://doi.org/10.12928/telkomnika.v20i3.23320.

[9] G. Gorel, and I. Fadhil, "Control Technique for Power Quality Improvement of Isolated Wind Power Generation System", *Bulletin of Electrical Engineering and Informatics*, Vol. 12, No. 4, 2023, pp. 1881-1892, https://doi.org/10.11591/eei.v12i4.5082.

[10] S. Swathi, B. S. Kumar, and J. Upendar, "Voltage and Frequency Stabilization by Fuzzy Integrated Droop Control of A Multi Renewable Source Micro Grid", *Indonesian Journal of Electrical Engineering and Computer Science*, Vol. 30, No. 3, 2023, pp. 1308-1320, http://doi.org/10.11591/ijeecs.v30.i3.pp1308-1320.

[11] R. Francis, and I. A. Chidambaram, "Application of Modified Dynamic Neural Network for the Load Frequency Control of a Two Area Thermal Reheat Power System", Int. Review of Automatic Control, Vol. 6, No. 1, 2013, pp. 47-53 .

[12] V. Jeyalakshmi, and P. Subburaj, "Load Frequency Control in Two Area Multi Units Interconnected Power System Using Multi objective Genetic Algorithm", *WSEAS Trans. on Power Systems*, 2015, Vol. 10, pp. 35-45, .

[13] S. S. Oleiwi, A. T. Humod, and F. A. Hasan, "Injected Power Control for Grid-Connected

Converter based on Particle Swarm Optimization", *Indonesian Journal of Electrical Engineering and Computer Science*, Vol. 27, No. 3, 2022, pp. 1199-1211, http://doi.org/10.11591/ijeecs.v27.i3.pp1199-1211.

[14] K. Jagatheesan, B. Anand and M.A. Ebrahim**,** "Stochastic Particle Swarm Optimization for Tuning of PID Controller in Load Frequency Control of Single Area Reheat Thermal Power System", *Int. J. of Electrical and Power Engineering*, Vol. 8, No. 2, 2014, pp. 33-40, doi: 10.36478/ijepe.2014.33.40.

[15] E. S. Ali, and S. M. Abd-Elazim, "Bacteria Foraging Optimization Algorithm Based Load Frequency Controller for Interconnected Power System", *Int. J. of Electrical Power and Energy Systems*, Vol. 33, No. 3, March 2011, pp. 633-638, https://doi.org/10.1016/j.ijepes.2010.12.022.

[16] E. S. Ali, and S. M. Abd-Elazim, "BFOA based Design of PID Controller for Two Area Load Frequency Control with Nonlinearities", *Int. J. of Electrical Power and Energy Systems*, Vol. 51, October 2013, pp. 224-231, https://doi.org/10.1016/j.ijepes.2013.02.030.

[17] S. M. Abd-Elazim, and E. S. Ali, "Load Frequency Controller Design of a Two Area System Composing of PV Grid and Thermal Generator via Firefly Algorithm", *Neural Computing and Applications*, Vol.30, No. 2, 2018, pp.607-616, https://doi.org/10.1007/s00521-016-2668-y.

[18] S. J. Safi, S. S. Tezcan, I. Eke, and Z. Farhad, "Gravitational Search Algorithm (GSA) Based PID Controller Design for Two Area Multi-Source Power System Load Frequency Control (LFC)", *Gazi University, J. of Science*, 2018, Vol. 31, No. 1, pp.139-153.

[19] A. Y. Abd-Elaziz and E. S. Ali, "Load Frequency Controller Design via Artificial Cuckoo Search", *Electric Power Components and System*, Vol. 44, Issue 1, 2016, pp. 90-98, https://doi.org/10.1080/15325008.2015.1090502

[20] S. M. Abd-Elazim, and E. S. Ali, "Load Frequency Controller Design via BAT Algorithm for Nonlinear Interconnected Power System", *Int. J. of Electrical Power and Energy Systems*, Vol. 77C, May 2016, pp. 166-177, https://doi.org/10.1016/j.ijepes.2015.11.029.

[21] N. C. Patel, B. K. Sahu, D. P. Bagarty, P. Das, and M. K. Debnath, "A Novel Application of ALO-based Fractional Order Fuzzy PID Controller for AGC of Power System with Diverse Sources of Generation", *Int. J. of Electrical Engineering Education*, 2021, Vol. 58, pp.465-487, https://doi.org/10.1177/0020720919829710.

[22] O. Can, A. Ozturk, and H. Kotb, "Ant-Lion Optimizer-Based Load Frequency Controller for a Hybrid Power System with PV and Thermal Power Plant", *Research Square*, June 29th, 2022, https://doi.org/10.21203/rs.3.rs-1669336/v1.

[23] D. Mohanty, and S. Panda, "Frequency control of Hybrid Power System by Sine Function Adapted Improved Whale Optimization Technique", *Int. J Ambient Energy*. 2020, https://doi.org/10.1080/01430750.2020.1839550.

[24] R. K. Khadanga, A. Kumar, and S. Panda, "A Novel Modified Whale Optimization Algorithm for Load Frequency Controller Design of a Two-Area Power System Composing of PV Grid and Thermal Generator", *Neural Computing and Applications*, 2020, Vol. 32, pp.8205-8216, https://doi.org/10.1007/s00521-019-04321-7.

[25] A. Kumar, and S. Suhag, "Whale Optimization Algorithm Optimized Fuzzy-PID Plus PID Hybrid Controller for Frequency Regulation in Hybrid Power System", *J. Inst. Eng. India Ser. B*, April

2022, Vol. 103, No. 2, pp. 633-648, https://doi.org/10.1007/s40031-021-00656-9.

[26] Ö. Can, H. Eroğlu, and A. Öztürk, "The Automatic Generation Controller based on Whale Optimization Algorithm in PV-Thermal Power Systems", *Journal of the Faculty of Engineering and Architecture of Gazi University*, Vol. 38, No. 2, 2023, pp. 915-926.

[27] N. R. Babu, L. C. Saikia, S. Bhagat, and A. Saha, "Maiden Application of Hybrid Crow-Search Algorithm with Particle Swarm Optimization in LFC Studies", *In; In: P. Bansal, M. Tushir, V. Balas, and R. Srivastava, (Eds) Proceedings of Int. Conference on Artificial Intelligence and Applications; Advances in Intelligent Systems and Computing, Springer: Singapore*, 2021, pp. 427-439, https://doi.org/10.1007/978-981-15-4992-2_40.

[28] N. R. Babu, L. C. Saikia, S. K. Bhagat, S. K. Ramoji, B. Dekaraja, and M. K. Behra, "LFC of a Solar Thermal Integrated Thermal System Considering CSO Optimized TI-DN Controller", *In: B. Das, R. Patgiri, S. Bandyopadhyay, and V. E. Balas ,(Eds) Modeling, Simulation and Optimization. Smart Innovation, Systems and Technologies. Springer, Singapore*, 2021, pp. 323-334, https://doi.org/10.1007/978-981-15-9829-6_25.

[29] N. Jalali, H. Razmi, H. D. Mojarrad, "Optimized Fuzzy Self-Tuning PID Controller Design based on Tribe-DE Optimization Algorithm and Rule Weight Adjustment Method for Load Frequency Control of Interconnected Multi-area Power Systems", *J . Applied Soft Computing*, 2020, Vol. 93, 106424, https://doi.org/10.1016/j.asoc.2020.106424.

[30] A. H. Yakout, H. Kotb, H. M. Hasanien, and K. M. Aboras, "Optimal Fuzzy PIDF Load Frequency Controller for Hybrid Microgrid System Using Marine Predator Algorithm", *IEEE Access*, 2021, Vol. 9, pp. 54220-54232, https://doi.org/10.1109/ACCESS.2021.3070076.

[31] A. Sadollah, H. Eskandar, A. Bahreininejad, and J. H. Kim, "Water Cycle Algorithm with Evaporation Rate for Solving Constrained and Unconstrained Optimization Problems", Applied Soft Computing, Vol. 30, 2015, pp. 58-71, https://doi.org/10.1016/j.asoc.2015.01.050.

[32] A. Sadollah, H. Eskandar, H. M. Lee, D. G. Yoo, and J. H. Kim, "Water Cycle Algorithm: A Detailed Standard Code", *SoftwareX*, 5, 2016, pp.37-43, https://doi.org/10.1016/j.softx.2016.03.001.

[33] M. M. Hato, S. Bouallegue, and M. Ayadi, "Water Cycle Algorithm-Tuned PI Control of A Doubly Fed Induction Generator for Wind Energy Conversion", *9th Int. Renewable Energy Congress (IREC)*, 20-22 March 2018, Hammamet, Tunisia, doi 10.1109/IREC.2018.8362516.

[34] CH. N. S. Kalyan, B. S. Goud, M. Bajaj, M. K. Kumar, E. M. Ahmed, and S. Kamel, "Water-Cycle-Algorithm-Tuned Intelligent Fuzzy Controller for Stability of Multi-Area Multi-Fuel Power System with Time Delays", *Mathematics* 2022, Vol. 10, 508, doi.org/10.3390/math10030508.

[35] M. Y. Javed, A. Hasan, S. T. H. Rizvi, A. Hafeez, S. Sarwar and A. J. Telmoudi, "Water Cycle Algorithm (WCA): A New Technique to Harvest Maximum Power from PV", *Cybernetics and System An International Journal*, 2022, Vol. 53, No. 1, pp. 80-102, doi.org/10.1080/01969722.2021.2008683.

[36] F. T. Tomy and R. Prakash, "Load Frequency Control of a Two Area Hybrid System Consisting of a Grid Connected PV System and Thermal Generator", *Int. J. of Research in Engineering and Technology*, Vol. 3, No. 7,

May 2014, pp. 573-580, doi: 10.15623/ijret.2014.0319103.

[37] M. A. Raouf Shafei, A. N. Abd Alzaher, and D. K. Ibrahim, "Enhancing Load Frequency Control of Multi-Area Multi-Sources Power System with Renewable Units and Including Nonlinearities", *Indonesian Journal of Electrical Engineering and Computer Science*, Vol. 19, No. 1, 2020, pp. 108-118, http://doi.org/10.11591/ijeecs.v19.i1.pp108-118.

[38] C. Andic, S. Ozumcan, M. Varan and A. Ozturk, "A Novel Sea Horse Optimizer Based Load Frequency Controller for Two-Area Power System with PV and Thermal Units", 14 April 2023, https://doi.org/10.20944/preprints202304.0368.v1.

APPENDIX

The network parameters are given as follow:

a) The constants of the heat grid: T_d =20 sec; T_{tu} =0.3 sec; T_{re} ==10 sec; T_{12} =0.545 p.u; T_{go} =0.08 sec; K_d =120. Hz/p.u MW; B=0.80 p.u MW/Hz; a_{12} =-1; R =0.40 Hz/p.u MW; K_{re} =0.33 p.u MW.

b) The constants of WCA: N_{var} =21, N_{pop} =100, C=2, U= 0.04, d_{upper} =0.001, $Max.generation$ =50.

Jouf University Science and Engineering Journal (JUSEJ) 2023; 10(2): 39- 55
Published online: Dec. 2023 (https://www.ju.edu.sa/en/jouf-university-science-and-engineering-journal-jusej/home/)
Print ISSN: 1658-6670 ***Electronic ISSN:1658-9173 (1443/5074)***

DESIGN AND PRODUCTION OF SELF-COMPACTING CONCRETE (SCC) BY USING GUM ARABIC (GA) AS A NATURAL PLASTICIZER

A.E. Hassaballaa[1,*] and Ahmed A. El-Abbasy[2]

[1] Assistant Prof., Civil Engineering Department, Faculty of Engineering, Jazan University, Jazan 82822, KSA.

[2]Professor, Civil Engineering Department, Faculty of Engineering, Jazan University, Jazan 82822, KSA.

***Corresponding author**

A.E. Hassaballa

Email address:
tomali99@yahoo.com

Submission Date: *July 17, 2023*
Accepted Date: *Sept. 21, 2023*

The aim of this study is to determine whether gum Arabic can be used as a natural plasticizer to produce self-compacting concrete and increase its compressive strength. In this article, the ability of gum Arabic to act as a plasticizer in concrete was studied with the goal of producing self-compacting concrete. The EFNARC (European Federation of National Associations Representing Concrete) guidelines were used for the concrete mix design. To test the effect of this low-cost natural admixture on producing self-compacting concrete, liquid gum Arabic was added to concrete mixtures in ratios ranging from 0.1% to 0.7% taken from the weight of cement. Two values of water-cement ratios (w/c) were used: the first one is 0.45 (calculated by mix design procedure), and the second was taken as 0.40 (to use gum Arabic acting as a water-reducer). Three cubes from each sample were prepared, molded and tested at 7 and 28 days of age. The results obtained show that GA has significant effects on the production of self-compacting concrete according to the ratios used. As GA ratios increase, filling ability, passing ability and segregation resistance improve. The effect of GA on the properties of hardened concrete was also studied by preparing concrete cubes mixed with 0.3% to 0.7% of the GA and tested at all ages. The results of these samples revealed that gum Arabic did not improve compressive strength at the age of 7 days, but that gum Arabic did so at the age of 28 days, when compressive strength increased significantly.0.4% of GA resulted in the highest value of compressive strength (36.894 MPa) followed by 0.5% (35.820 MPa). Another sample was prepared using GA as the water reducer, decreasing W/C to 0.40. In addition, at the age of 7 days, gum showed no effect on the increase in strength, but at the age of 28 days, there was a clear effect on the increase in strength of SCC; 0.5% of GA showed the highest strength value (39.79 MPa) followed by 0.6% (38.51 MPa).

Keywords: *Self-compacting concrete; Gum Arabic; admixture; Concrete mix design; Workability; Compressive strength*

1. INTRODUCTION

Self-compacting concrete (SCC) applications are in higher demand as megastructure construction expands globally. Excessive reinforcement of the main structural components is a problem in many sites. Due to the high risk of seismic areas, vulnerability to hurricane storms, and increased production capacity on a very large scale, design challenges are exacerbated. In these tough environments, SCC has become the only option. SCC is today the most remarkable technological achievement and inventive development in the area of concrete technology. SCC is the concrete of the future due to its distinct advantages, so it will eventually replace conventional concrete. Self-compacting concrete (SCC), often referred to as self-consolidating concrete or rheodynamic concrete, is a recently designed concrete that does not require vibration for placement and compaction. It can flow under its own weight even when there is crowded reinforcement, completely filling the formwork and performing a complete compaction. SCC mixtures are proportionate in a manner that is not the case for ordinary concrete mixtures. In order to ensure the strength and fluidity of the concrete mix, SCC requires a high powder content, less coarse aggregate, a high-range superplasticizer, and a VMA (Viscosity Modifying Agent). Fluidity, deformability, filling capacity and resistance to segregation are all factors that make SCC workable. A report on self-consolidating concrete with new viscosity-modifying admixtures was presented by Lachemia et al. (1). The experimental investigation of this study was a two-stage process. Four different polysaccharide-based VMAs (suspended in water), categorized as new VMA types A, B, C, and D, as well as a commercial VMA predominantly used in Canada, was tested on a variety of mortar mixtures in Phase 1. Phase 2 examined the viability of producing CCS with newly selected VMAs. Cement, aggregates, and admixtures make up the constituent materials. The article concluded that theological and setting time tests on mortar indicate that all novel VMAs can be used in the production of an SCC with satisfactory qualities and with a less VMA dose than commercial motor. A presentation on the use of gum Arabic as an additive in self-compacting concrete was presented by Caroline M. Athman et.al. (2). In this study, Gum Arabic and Superplasticizer were used as admixtures in addition to the normal concrete ingredients. Different types of superplasticizers have been used for concrete mixtures. Based on the European Standards for Testing Self-Compacting Concrete (EFNARC), trial mixtures were created. Cement and gum Arabian react faster. The final ideal mix design ratios used were: 1.1, 1.0, 0.9, and 0.8 water-powder ratios, and dosages of 2%, 4%, 6%, 8%, 10%, and 12% gum Arabic by weight of cement. Gum Arabic behaves well in a spread flow with a water-powder ratio between 1.0 and 0.8. Self-compacting concrete (SCC) with great performance was explored by Syed Ali Rizwan et al. (3). The data presented in this essay is based on observations made in the lab, research conducted at a concrete manufacturing facility, and finally, underground installations made in a nearby tunnel of a teaching and research mine. There, SCC was poured 150 metres vertically and 150 metres horizontally (above and beneath the ground). According to reports, replacing cement quantity with limestone filler (LSP) (on the order of 100 kg/m3) reduces the amount of cement required to obtain a given slump flow, viscosity, and concrete strength at a young age. The superplasticizer (SP) content in a desired flow rate and (FA) usually reduces water demand. Paratibha et. al. investigated an experimental technique for the design of self-compacting concrete mixtures (4) Results of experiments on workability that were done to produce self-compacting concrete. Experiments began with coarse aggregates representing 50% of the total volume of concrete and fine aggregates representing 40% of the total volume of concrete. To achieve SCC

mixes, the w/p ratio and superplasticizer were varied. The superplasticizer content was determined to be 0, 0.76 and 3.80, respectively. The properties of some mixes satisfied the slump flow property, however only one mix had a T50 cm of 2 sec. As presented by P. Ramanathan et al. (5), tests of workability for various mineral admixtures are conducted in order to investigate strength types experimentally. The procedure involves replacing mineral admixtures with 30%, 40%, and 50% Portland cement, followed by performance testing. The results of the studies conducted to ascertain the mechanical and fresh properties of mixtures for self-compacting concrete are as follows: The results of the mechanical properties tests (compressive, split, and flexure) showed significant performance changes, and it was discovered that the Silica fume series had a higher compressive strength. Nenrad Ristic et al. examined the characteristics of the SCC made from waste materials. (6). In this paper, the results of research on the effects of mineral admixtures on the properties of freshly mixed and cured self-compacting concrete were given. These admixtures included red mud, fly ash, flotation tailings from a copper mine, milled recycled glass from cathode tubes, and others. The study discovered that waste resources, including red mud and fly ash as mineral admixtures, flotation tailings from a copper mine, milled recycled glass from cathode tubes. This study examined the impact of mineral admixtures, flotation tailings from a copper mine, red mud, and fly ash, on the characteristics of fresh and hardened SCC. According to the study, it is possible to create SCCs using waste materials such red mud and fly ash as mineral admixtures, milled recycled glass from cathode tubes, flotation tailings from a copper mine, and recycled glass from cathode tubes. R. Khurana et al. (7) shows the value of low water cement to improve the durability of concrete, which has long been recognized; in this study, the properties of self-compacting concrete with significant amounts of fly ash are compared to those of freshly mixed, hardened regular concrete. In order to evaluate if gum Arabic is appropriate for use as a plasticizer in the creation of self-compacting concrete, Ravichandran Subbarayalu et al., (8) examined the influence of gum Arabic on an ecological self-compacting concrete. The self-compacting concrete, that used Gum Arabic as a plasticizing admixture at two different percentages, had a water/powder ratio of 0.45 compared to the normal concrete (regular concrete), which had a water/cement ratio of 0.5. The quantity of components needed to determine the proportions of the mix was weighed. According to the European Standards for Testing Self Compacting Concrete, the L-box, Fill-box, Slump Flow, and V-Funnel tests were used to assess the concrete's self-compacting abilities. It has a conformity value of ≥ 0.75 for a class 1 passing ability and a time-based conformity of 7.2 seconds. The fill-box test deals with the filling ability process of the concrete through heavily reinforced formwork. Based on the results obtained, it was concluded that gum Arabic was found to be a viable ecological plasticizer and a very good viscosity-modifying agent. Ravichandran Subbarayalu et al. (9), Muhammad Waqas Malik (10), Rose Mbugua et al. (11) and Abdeliazim et al. (12) all carried out studies on self-compacting concrete. Gum Arabic was found to be a very effective natural admixture in all of these studies. This work uses (EFNARC) Specification & Guidance. It focuses on specialist concrete systems and construction chemicals. The European Federation of National Trade Associations, which represents manufacturers and users of specialist building materials, was created in March 1989 (13). It also uses the methodology of the British Department of Environment (DoE) (14). However, because of the chemical interactions between them and concrete, some chemical admixtures are expensive in addition to raising environmental concerns, and they are also vulnerable to damage from improper storage. Researchers started to consider ways to address this issue through experiments using inexpensive local materials and looked at the

viability of using Gum Arabic as a cheap admixture. Gum Arabic is an effective water-reducer for calcium sulphate plasters and is utilized as a pumping aid, according to American Concrete Institute (ACI-2005) (15) and (Caroline, 2018) (2)

2. MIX DESIGN DATA USING EFNARC SPCIFICATIONS

The following are the EFNARC standards guidelines (13) that have been applied in this research to produce SCC:

2.1. *COMPOSITION OF INITIAL MIX*

It is more useful to think about the relative proportions of major components per volume rather than per mass while creating the mix. The following list includes typical ranges of quantities and proportions required to obtain a SCC. For the needs of strength satisfaction and other performance criteria, further adjustments will be required.

- Water/powder ratio from 0.80 to 1.10.
- Total quantity of powder (m^3) varies from 160 to 240 liters (400 to 600 kg)
- The mix typically contains 28 to 35 percent by volume of coarse aggregate.
- The chosen water-cement ratio is determined by the specifications of EN 206. Normally, water content is no more than 200 litres/m3.
- The volume of the other components is balanced with the sand content.

2.2. MIXTURE ADJUSTMENT

If satisfactory performance is not possible, then a fundamental redesign of the mix should be taken into account. Depending on the apparent issue, one of the following actions might be suitable:

- Add more or different types of fillers (if they exist),
- Adjusting the ratios of the coarse aggregate or sand,
- Adding a viscosity-modifying agent, if one is not already present in the mixture,
- Changing the water content of the admixture to change the water/powder ratio, increasing the dosage of the superplasticizer and/or the viscosity modifying agent, or
- Using different kinds of superplasticizers (and/or VMA), more compatible with local materials.

2.3. MIX DESIGN PROCEDURE

This example shows how to produce SCC combinations effectively. The following is the recognized order:

A. The optimum air content is usually given by 2 %.

B. Calculating the volume of coarse aggregate

C. Determination of the sand content.

D. Design a paste composition.

E- Estimate the amount of superplasticizer to use in a mortar and the optimal water to powder ratio.

F- Concrete characteristics are assessed by standardized tests.

3. MATERIALS AND METHODS

In this study, water, cement, coarse aggregate and fine aggregate were used to generate concrete mixes.

3.1. CEMENT

Ordinary Portland cement in accordance with ASTM C 150 (15) is used and supplied by the South Cement Company in the Jazan area of Saudi Arabia. According to ASTM C 191-01 (16), the cement mortar consistency, setting time and strength of the concrete have all been tested.

3.2. COARSE AGGREGATE

Concrete aggregates must comply with the specific requirements relating to the best technical use. They must be clear, solid, hard and durable, free of chemicals, clay and other substances. Quantities of fine materials that could have an impact on how cement paste bonds and hydrates. Sieve analysis results in a general characterization of an aggregate granular distribution (ASTM C 136) (17). The largest size of coarse aggregate used in this research has a maximum size of 12.5 mm.

3.3. WATER:

The cheapest and most crucial element in concrete is water. When adding water to the cement, the chemical hydration process happens. Rehydration results in the formation of a thick, viscous gel with the ability to bind and bind all aggregates into a solid form. This means that all of the components of concrete are held in place by cement and water. ASTM C 94 (18) outlines acceptable requirements for the use of water in concrete. The raw gum was mechanically ground into a liquid form, which was then added in ratios of 0.0% (control mix), 0.1%–0.7% by the weight of cement. This was done to verify the impact of gum Arabic on the compressive strength of concrete. The workability tests were conducted as soon as the concrete was mixed for all samples (19, 20). The compressive strength of the concrete cubes was tested at the age of 7 and 28 days. Using 100 x 100 x 100 mm metallic molds, concrete cubes were cast.

Fig. 1. Processed gum Arabic

Fig. 2. Unprocessed gum Arabic

4. RESULTS OF LABORATORY EXPERIMENTS

In this research, Gum Arabic was added to concrete mixes in liquid state at ratios ranging from 0.1% to 0.7%, taken from the weight of cement, in order to investigate its impact on producing self-compacting concrete and on the compressive strength of hardened concrete. The experiments conducted in this research include sieve analysis of coarse and fine aggregate, slump flow test, T50 test, L-box test, V-Funnel test and compressive strength test for 7 and 28 days. Three cubes representing each sample were cast using a mould of 10 cm x 10 cm x 10 cm. The cubes were immersed in water tank for full curing and tested at 7 and 28 days (in this sample, W/C = 0.45). In another sample, the GA was used as a water reducing agent (W/C = 0.4) using 0.5%, 0.6% and 0.7% of the GA. Since the ratios of 0.1% to 0.4% of the GA were resulted in dry mixes (by investigating 0.4%), so they were not considered. The results are given in the tables and figures below.

4.1 RESULTS OF INITIAL TESTS OF METERIALS

TABLE 1 *Results of Physical Properties of Cement Paste*

No	Test	Results	ASTM C150
1	Standard paste consistency (water %)	25%	25%-33%
2	Standard of cement paste Vicat apparatus) (mm)	34	33 - 35
3	Initial setting time (min)	85	Not less than
4	Final setting time (min)	149	Not more than
5	Fineness %	2%	Not more than

Table 1 demonstrates that the ordinary Portland cement used in this research conforms to the ASTM C150 specifications. Such cement can produce good concrete mixes, which in turn can result in high compressive strength.

TABLE 2 *Initial and Final Setting Time of Cement Paste Using 0.0% to 0.7% of the GA*

No	GA	Initial setting		Final setting time	
	(%)	(min)	(hr)	(min)	(hr)
1	0.0	85	1.41	149	2.48
2	0.1	110	1.83	155	2.58
3	0.2	118	1.96	166	2.76
4	0.3	128	2.13	184	3.06
5	0.4	164	2.73	280	4.66
6	0.5	244	4.06	367	6.12
7	0.7	383	6.38	514	8.57

Table 2 displays how gum affects both the initial and final setting time. The data shown in this table clearly show that gum Arabic is regarded as a retarder admixture due to the length of time it takes cement paste to set. As can be seen, the first setting time for gum ratios ranging from 0.0% to 0.7% takes 85 to 383 minutes, whereas the final setting time for the same GA ratios requires 149 to 514 minutes.

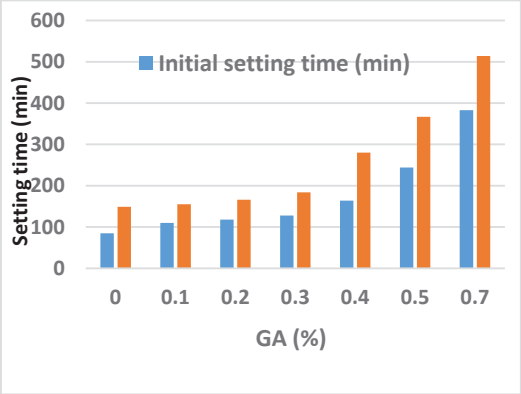

Fig. 3. Initial and final setting time of cement paste using 0.0% to 0.7% of the GA

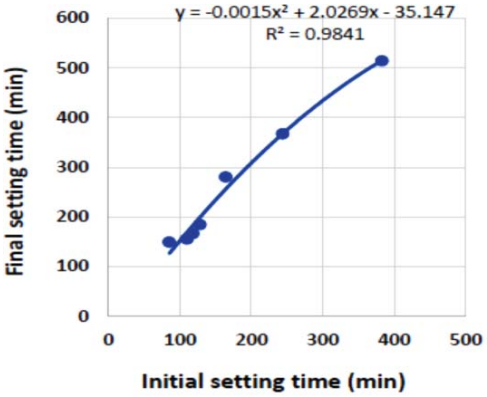

Fig. 4. Relationship between Initial and final setting time of cement paste using 0.0% to 0.7% of the GA

Fig. 4 shows a relationship between initial and final setting time of cement pastes by adding gum Arabic, from which formula 1 can be obtained. Figure 4 indicates that the final setting time is a function of initial setting time, and this relationship is valid only for gum Arabic ratios ranging from 0.0% to 0.7%.

$$Y = -0.0015X^2 + 2.0269X - 35.147 \quad (1)$$

$$R^2 = 0.9841$$

Where

Y = Final setting time, X = Initial setting time

R^2 = the coefficient of determination

TABLE 3: *Results of Sieve Analysis of Fine Aggregate*

Sieve Size (mm)	Retained (gm)	Cumulative Retained (gm)	Cumulative Retained (%)	Passing (%)
4.75	48	48	4.82	95.18
2.36	48	96	9.64	90.36
1.18	131	227	22.79	77.21
0.6	526	753	75.60	24.40
0.3	140	893	89.66	10.34
0.15	74	967	97.09	2.91
Pan	29	996	100	0
Total	996	-	-	-

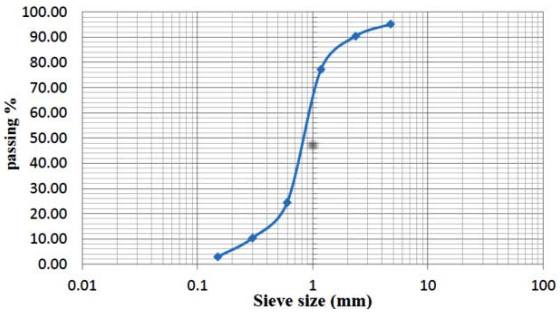

Fig. 5. Grading of fine aggregate

From Figure 5:

D10=0.29 D30 = 0.66 D60 = 0.99

Cu = D60/D10 =3.41 Cu >1 (well graded aggregate)

$Cc = \frac{D30\hat{}2}{D60 * D10} = (0.66*0.66)/(0.99*0.29) = 1.51$

1< Cc < 3 Smooth curve (well graded)

From Table 3, Fineness modulus (FM) of fine aggregate can be calculated as

FM = 299/100 = 2.99.

Fine aggregate FM is useful for estimation of the proportion of fine and coarse aggregates in concrete mixtures (ASTM C 136) (14).

TABLE 4: *Results of Sieve Analysis of Coarse Aggregate*:

Sieve Size (mm)	Retained (gm)	Cumulative Retained (gm)	Cumulative Retained (%)	Passing (%)
25	0	0	0	100
19.2	0	0	0.00	100.00
12.5	332	332	16.58	83.42
9.5	1226	1558	77.78	22.22
4.75	445	2003	100.00	0.00
Pan	0	2003	100	0
Total	2003	-	-	-

D10 = 6.89 D30 = 9.88 D60 =11.35
Cu= D60/D10 = 1.65 Cu >1 (well graded aggregate)
$Cc=\frac{D30^2}{D60*D10}$ *= (9.88*9.88)/(11.35*6.89) =1.24*
1< Cc <3

Smooth curve (well graded) The results in Tables (3 and 4) show that the fine aggregate and coarse aggregate are well graded as depicted in Figures (5 and 6). This grading will lead to achieving good concrete properties

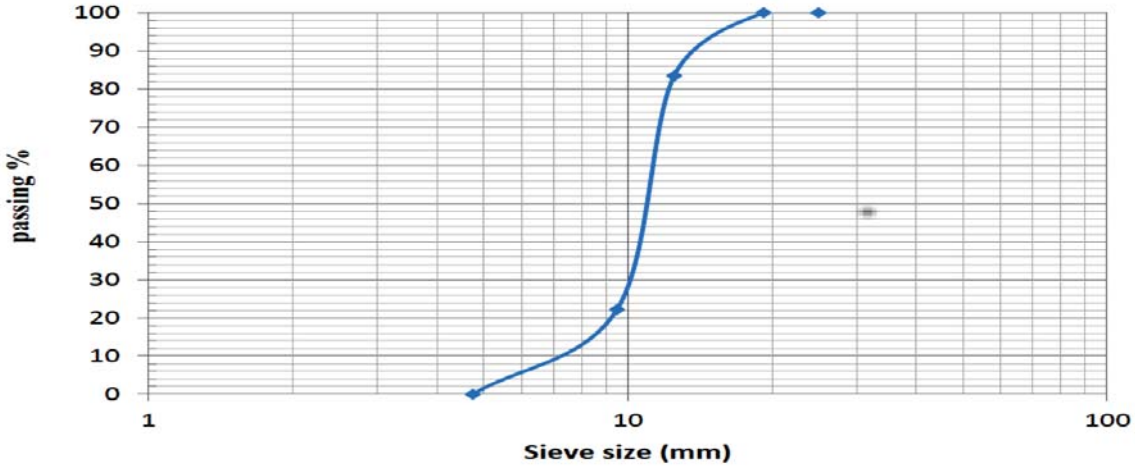

Fig. 6. Grading of crushed coarse aggregate

4.2 RESULTS OF CONCRETE MIXES (W/C = 0.45)

TABLE 5: *Concrete Constituents Used in This Study, as Per EFNARC Mix Design Guidelines Using 0.1% to 0.7% of the GA*

Ingredient	Quantity (kg/m^3)			EFNARC Guidelines			
Water	190			< 200 liters			
Cement	420			400 - 600			
Fine aggregate.	760			> 50% by weight of total aggregate			
Coarse aggregate	750			Normally, 28 to 35 per cent by volume of the mix			
Gum Arabic (%)	0.1%	0.2%	0.3%	0.4%	0.5%	0.6%	0.7%
Gum Arabic (kg/m^3)	(0.42)	(0.84)	(1.26)	(1.68)	(2.10)	(2.52)	(2.94)
Total (kg/m^3)	2120.42	2120.84	2121.26	2121.68	2122.10	2122.52	2122.94

4.2.1 Testing of Workability of Self-Compacting Concrete

Fig. 7. Samples of T50 and slump flow tests

Fig. 8. L-box test

Fig. 9. Sample of V–Funnel test

TABLE 6: *Results of Slump Flow Tests*

No	G.A. (%)	D1 (mm)	D2 (mm)	Average (mm)	Acceptable Range (650 to 800 mm)
1	0.1	570	540	555	Rejected
2	0.2	640	580	610	Rejected
3	0.3	720	640	680	Acceptable
4	0.4	760	780	750	Acceptable
5	0.5	700	800	750	Acceptable
6	0.6	750	770	760	Acceptable
7	0.7	810	810	810	Acceptable

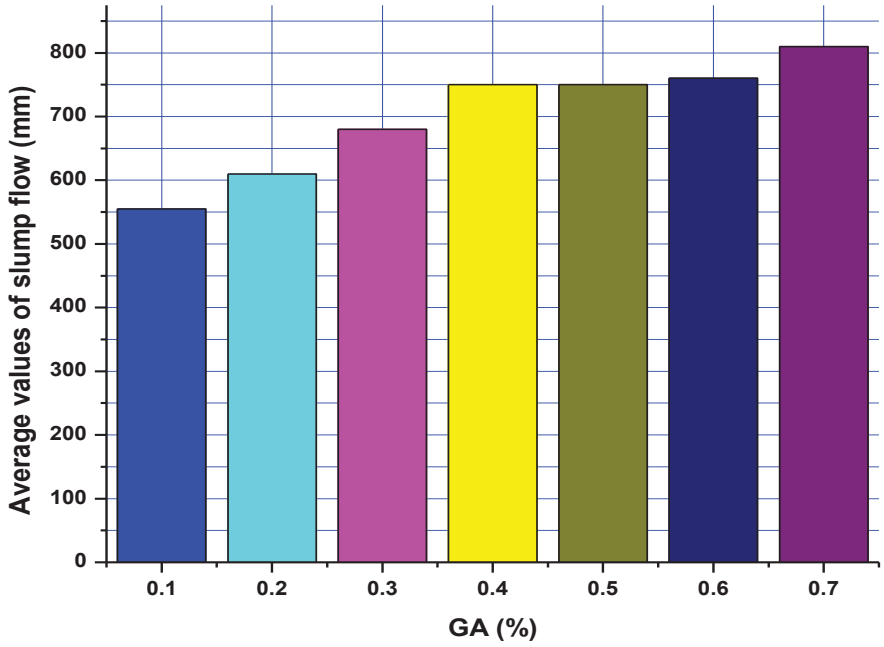

Fig.10. Results of slump flow tests

TABLE 7: *Results of T50 (sec)*

Number	G.A. (%)	Time (sec)	Acceptable Range (2 to 5 sec)
1	0.1	9.20	Rejected
2	0.2	7.85	Rejected
3	0.3	4.10	Acceptable
4	0.4	3.52	Acceptable
5	0.5	3.33	Acceptable
6	0.6	3.12	Acceptable
7	0.7	2.45	Acceptable

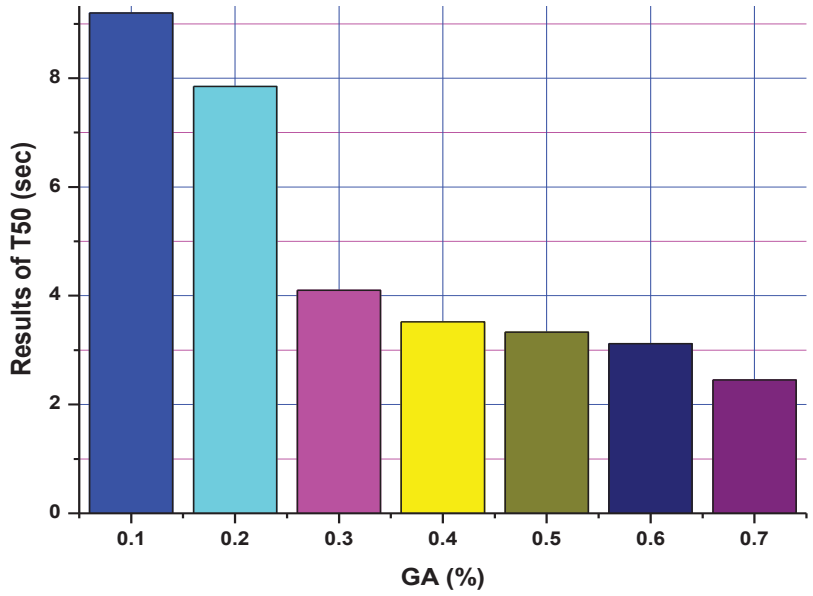

Fig. 11. Results of T50 tests (sec)

TABLE 8: *Results of L-box Tests*

No	G.A (%)	H1 (cm)	H2 (cm)	Passing Ratio (H2/H1)	Acceptable Range (0.8 to 1) cm
1	0.1	10.1	7.2	0.71	Rejected
2	0.2	9.8	7.8	0.79	Rejected
3	0.3	9.5	8.2	0.86	Acceptable
4	0.4	9.3	8.4	0.90	Acceptable
5	0.5	9.0	8.6	0.96	Acceptable
6	0.6	8.8	8.6	0.97	Acceptable
7	0.7	8.1	8.0	0.99	Acceptable

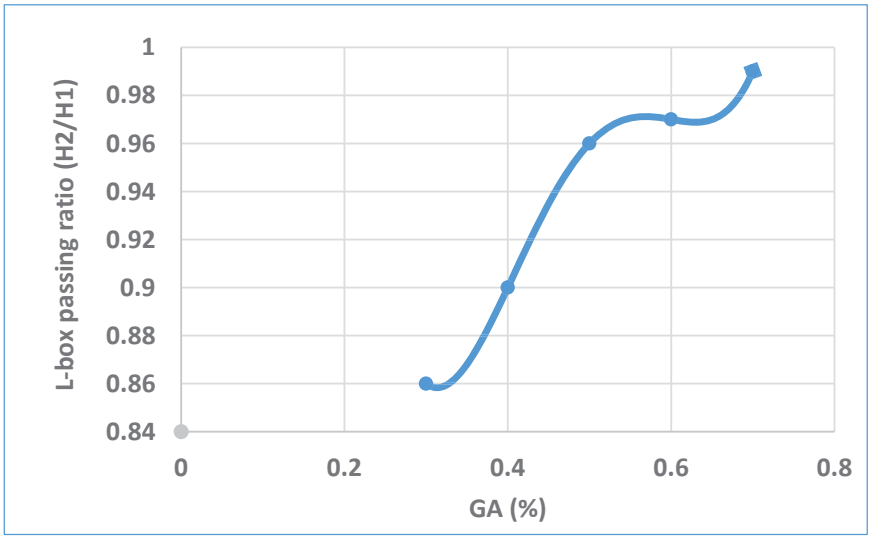

Fig.12. L-box passing ratio test

Referring to Fig. 12, Formula 2 can be obtained. This formula expresses the effect of gum Arabic, as a product of producing self-compacting concrete, on passing ability of concrete mixtures.

$$Y = 54.167X^4 - 109.17X^3 + 79.458X^2 - 24.308X + 3.51 \quad (2)$$

$$R^2 = 1$$

Where:

Y is passing ability ratio (H2/H1).

X is the percentage of added Gum Arabic.

This formula is valid only for the ratios ranging from 0.3% to 0.7% of gum Arabic.

TABLE 9: *Results of V-Funnel Tests*

No	G.A. (%)	Time (sec)	Acceptable Range (8 to 12 sec)
1	0.1	15.30	Rejected
2	0.2	14.10	Rejected
3	0.3	11.00	Acceptable
4	0.4	10.20	Acceptable
5	0.5	9.70	Acceptable
6	0.6	9.00	Acceptable
7	0.7	8.60	Acceptable

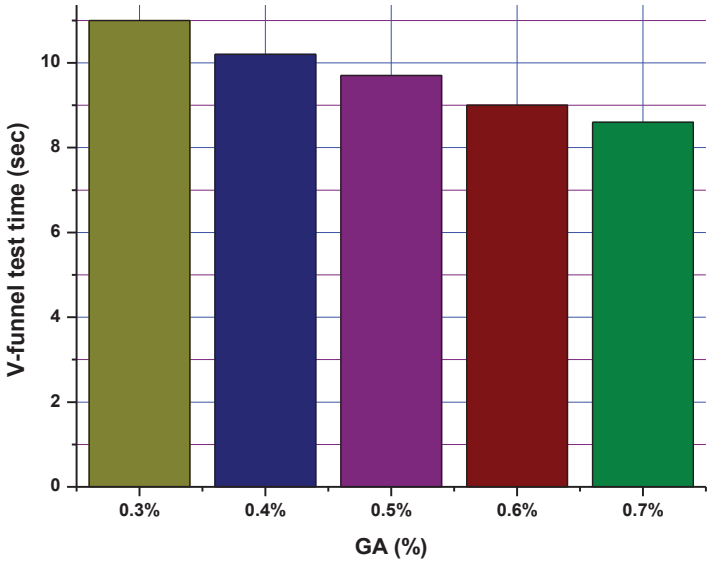

Fig. 13. Results of V-Funnel test

4.2.2 Results of Compressive Strength (W/C = 0.45)

TABLE 10: *Results of Compressive Strength of Concrete Using 0.3% to 0.7% of GA for 7 and 28 Days of Age (W/C = 0.45)*

No.	G.A (%)	Age: 7 days		Age: 28 days		% Difference in strength at 7 and 28 days
		Average Load (kN)	Average Strength (MPa)	Average Load (kN)	Average Strength (MPa)	
1	0.0	261.06	26.11	301.20	30.120	15.36
2	0.3	247.80	24.78	338.74	33.874	36.68
3	0.4	235.50	23.55	368.94	36.894	56.65
4	0.5	216.70	21.67	358.20	35.820	65.30
5	0.6	210.60	21.06	351.90	35.190	67.09
6	0.7	206.80	20.68	347.00	34.700	67.79

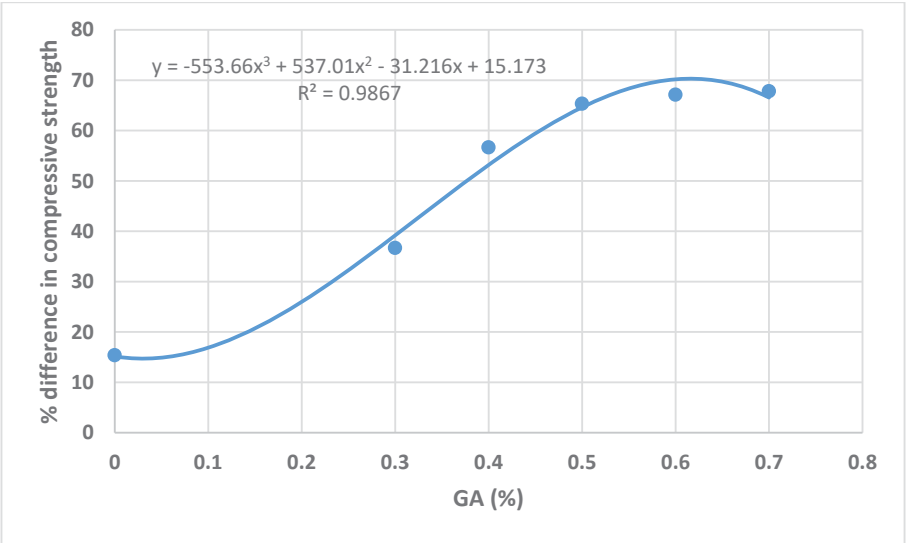

Fig. 14. % difference in compressive strength using 0.5% to 0.7% of GA at 7 and 28 days (W/C = 0.45)

With a water-cement ratio of 0.45, Fig. 14 illustrates a polynomial relationship between the compressive strength at 7 and 28 days of age.

4.3 RESULTS OF CONCRETE MIXES (W/C = 0.40)

In the following mixes, the water-cement ratio is reduced to 0.40, to investigate the ability of gum Arabic to act as a water-reducer. GA ratios less than 0.5% are neglected in the following results, because they resulted in dry mixes (by investigating 0.4% as a trial mix). Workability of self-compacting concrete in this case is determined by two tests: slump flow and L-box.

TABLE 11: *Results of Slump Flow Test*

No	G.A. (%)	D1 (mm)	D2 (mm)	Average (mm)	Acceptable Range (650 to 800 mm)
1	0.5	651	657	654	Acceptable
2	0.6	681	687	684	Acceptable
3	0.7	744	760	752	Acceptable

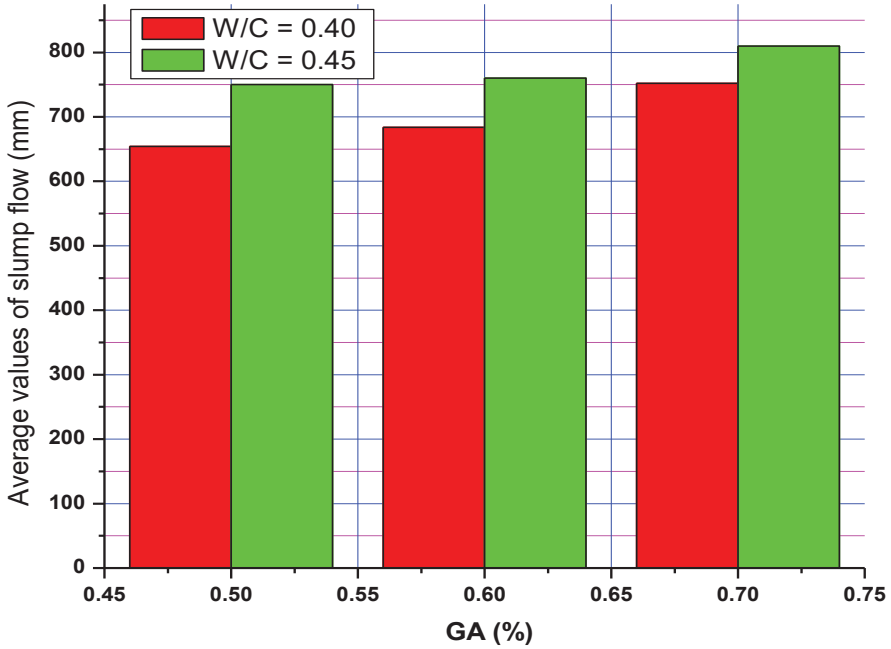

Fig.15. Results of slump flow tests using W/C ratios of 0.40 and 0.45

Figure 15 is illustrated from the results shown in Tables (6 and 11)

TABLE 12: *Results of L-box Tests*

No	G.A. (%)	H1 (cm)	H2 (cm)	Passing Ratio (H2/H1)	Acceptable Range (0.8 to 1) Cm
1	0.5	9.2	7.6	0.83	Acceptable
2	0.6	8.9	7.9	0.89	Acceptable
3	0.7	8.4	8.0	0.95	Acceptable

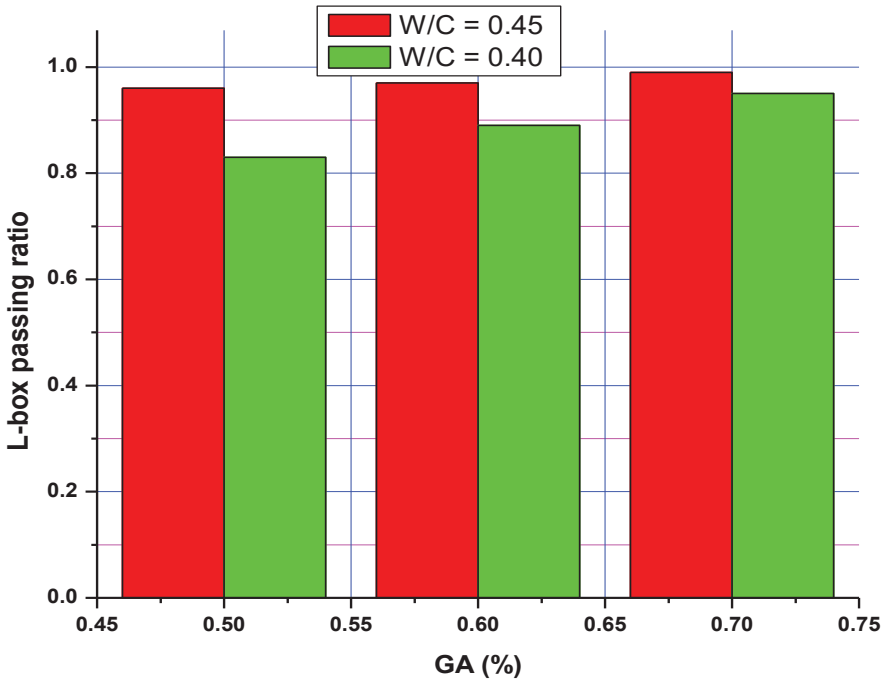

Fig. 16. L-box passing ratios using W/C ratios of 0.40 and 0.45

TABLE 13: *Results of Compressive Strength of Concrete Using 0.5% to 0.7% of GA for 7 and 28 Days of Age (W/C = 0.40)*

No	GA (%)	Age: 7 days		Age: 28 days		% Difference in strength at 7 and 28 days
		Average Load (kN)	Average Strength (MPa)	Average Load (kN)	Average Strength (MPa)	
1	0.0	293.40	29.34	331.20	33.12	12.88
2	0.5	271.50	27.15	397.90	39.79	46.56
3	0.6	243.60	24.36	385.10	38.51	58.09
4	0.7	222.21	22.22	362.20	36.22	63.01

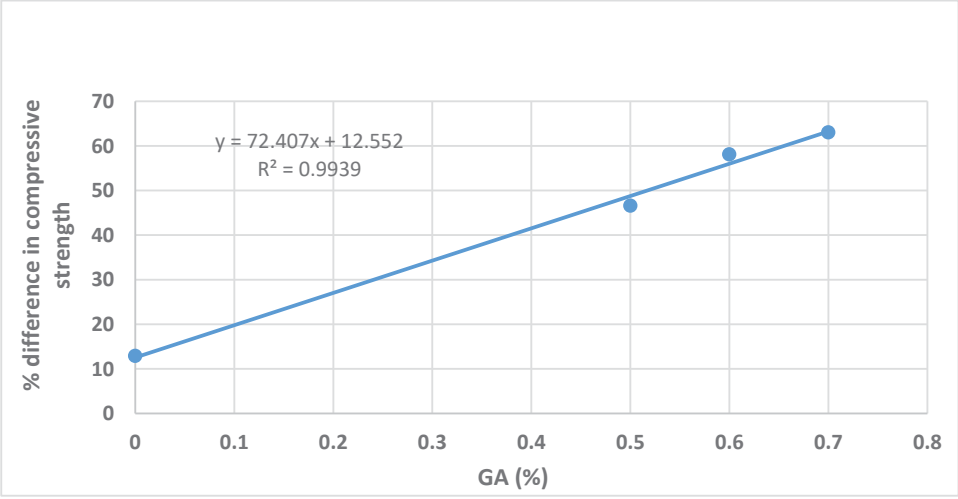

Fig. 17. % difference in compressive strength using 0.5% to 0.7% of GA at 7 and 28 days (W/C = 0.4)

Figure 17 demonstrates how the strength of the difference increases linearly as the GA ratio increases. The difference in strength between 7 and 28 days of age when GA is employed as a water reduction is practically a linear connection with R^2 = 0.994, as can be seen from this relation. This relationship is distinct from the one depicted in Fig. 14 where the water-cement ratio is assumed to be 0.45 and GA is not utilized as a water reducer.

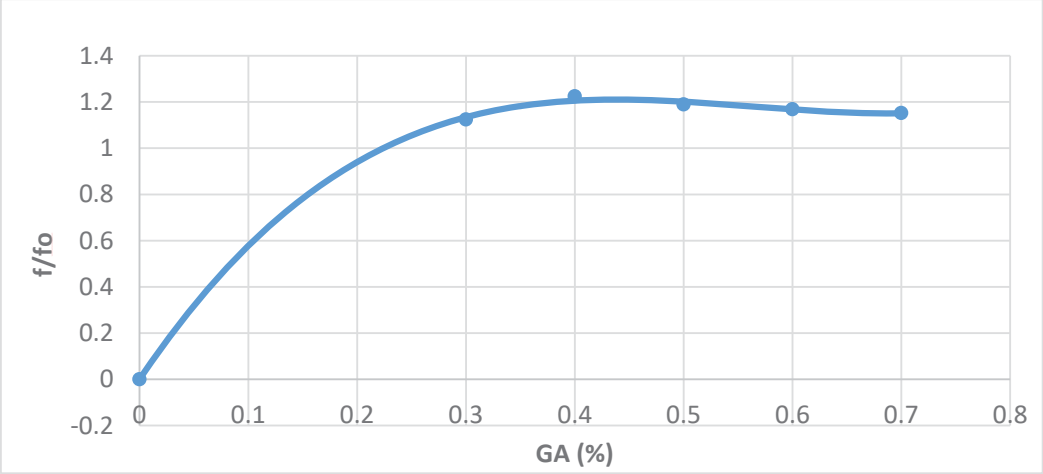

Fig. 18. Relationship between compressive strength of self-compacting concrete with and without adding GA

Referring to Table 10 and Fig. 18, Formula 3 can be generated:

$$Y = 7.7407X^3 - 13.083X^2 + 7.0104X - 0.0005 \quad (3)$$

$$R^2 = 0.9995$$

Where

Y is the ratio of compressive strength with and without adding gum Arabic (f/fo).

X is the percentage of added Gum Arabic.

This formula is only valid for ratios of 0.3% to 0.7% of gum Arabic.

The formulas above, which combine the experimental findings from this study, indicate that gum Arabic is a useful substance for producing self-compacting concrete and serving as a water-reducer agent.

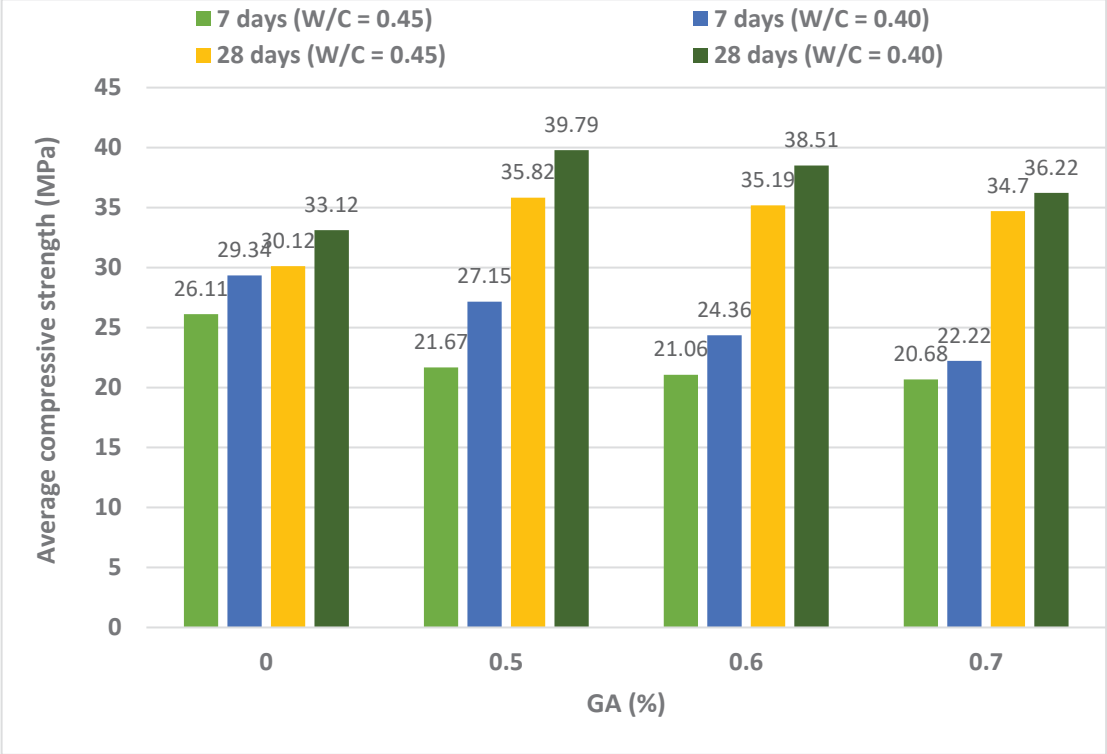

Fig. 19. Compressive strength of concrete mixes at 7 and 28days of age using W/C = 0.4 and 0.45.

The compressive strength of self-compacting concrete evaluated at 7 and 28 days of age using water-cement ratios of 0.45 and 0.40 and gum Arabic ratios of 0.0%, 0.5% to 0.7% is summarized in Fig. 19. This figure demonstrates that the highest compressive strengths for all gum Arabic ratios have been reached at 28 days of age when w/c = 0.40.

5. RESULTS AND DISCUSSION

Table 1 shows that the Portland cement used in this study complies with the ASTM C150 specifications. With this cement, concrete can have good workability and good compressive strength. Gum Arabic has a considerable impact on the cement's setting time. Table 2 and Fig. 3 make it very evident that as the GA ratio increases, so do the initial and final setting times. Both the fine and coarse aggregate are well graded, as indicated visually in Figures (5 and 6) and according to Tables (3 and 4). From this grading, it will be expected to achieve good concrete properties for that the well graded aggregates represent the main factor affecting the properties of fresh and hardened concrete. From 0.3% to 0.7% of GA used in determination of workability tests (slump flow, T50, L-box and V-Funnel) resulted in the acceptable range and show a good workability. 0.1% and 0.2% of GA gave dry samples and are in rejected areas, as specified by EFNARC guidelines. Workability tests are displayed graphically in Figures 8 to 13 and shown in Tables 6 to 9. According to Table 10, when using a water-cement ratio of 0.45, GA does not increase the compressive strength of concrete after 7 days, indicating that it should only be used to improve the workability of self-compacting concrete. When the gum was increased at the age of 28 days, there was a considerable improvement in strength. The maximum compressive strength was achieved with 0.4% GA (36.894 MPa), followed by 0.5% (35.820 MPa). These findings suggest that gum Arabic may increase the compressive strength of concrete at late age. Tables 11 and 12 display the slump flow test and L-box test outcomes when GA is used as a water-reducer and the W/C ratio is reduced to 0.40. In these samples, only

0.5% to 0.7% of the GA is used because ratios below 0.5% produced dry mixes, which are discarded. Although they are lower in values than those obtained without the decrease of water, the results in these Tables often fall within the accepted range. Using GA as a water-reducer (W/C = 0.40), Table 13 and Figure 17 show the results of compressive strength at 7 and 28 days. For the first seven days, GA has no impact on strength, but by day 28, compressive strength has significantly increased. However, at 28 days, there is a 20% strength difference between normal concrete and self-compacting concrete made with gum Arabic. As the GA ratio increases, the compressive strength at 28 days of age exhibits higher values than those at 7 days (see Table 13), ranging from 13% to 63%.

6. CONCLUSION

In this study, self-compacting concrete was produced using gum Arabic (GA), as a natural admixture. In numerous concrete mixes, liquid amounts of GA ranging from 0.1% to 0.7% (measured as percentages from the weight of cement) were employed. The following conclusions were reached:

1. By achieving the requirements of filling ability, passage ability, and segregation resistance, the liquid GA Arabic applied to concrete mixes produces self-compacting concrete in a considerable way.
2. It is found that the ratios of 0.3 to 0.7 of GA resulted in accepted flow tests, T50 tests, L-box tests and V-funnel tests whereas 0.1 and 0.2 of GA ratios showed rejected test results.
3. At the age of 7 days, gum Arabic does not increase the compressive strength of concrete and the control mix (0.0% GA) of concrete achieves the highest compressive strength.
4. It was found that gum Arabic had a substantial effect on enhancing compressive strength at the age of 28 days, with 0.4% producing the highest value (W/C =0.45) and the control mix producing the lowest value.
5. When using GA as a water-reducer, 0.5% of GA resulted in highest compressive strength for 28-day of age and lowest values resulted from the control mix.
6. The results of compressive strength generated by using GA as a water reducer (W/C = 0.40) showed higher values than when using W/C = 0.45 (normal mixes).

7. RECOMMENDATIONS

Since gum Arabic is an environment friendly admixture and its use in self-compacting concrete promote the global fight towards climate changes, it is recommended to use it as a local admixture to produce self-compacting concrete and act as a water-reducer in concrete mixtures.

8. ACKNOWLEDGEMENTS

Authors thank all associated personnel that have contributed to this study.

9. FUNDING

The study is not being supported by anyone or anything.

10. CONFLICT OF INTEREST

The authors affirm that their publication of this work does not include any conflict of interest.

11. REFRENCES

[1] M. Lachemia,*, K.M.A. Hossaina, V. Lambrosa, P.-C. Nkinamubanzib, N. Bouzoubaab. CANMET/Natural Resources Canada, 405 Rochester Street, Ottawa, ON, Canada K1A 0G1. Receive 5 February 2003; accepted 27 October 2003.

[2] Caroline M. Athman, Silvester O. Abuodha, Timothy Nyomboi. International Journal of Innovative Science and Modern Engineering (IJISME) ISSN: 2319-6386, Volume-5 Issue-4, April 2018.

[3] Syed Ali Rizwan, Thomas A Bier, Husnain Ahmad. Pakistan Engineering Congress, 70th Annual Session Proceedings. Paper No. 670.

[4] Paratibha AGGARWAL, Rafat SIDDIQUE, Yogesh AGGARWAL , Surinder M GUPTA (2008) Self-Compacting Concrete- Procedure for Mix Design. Department of Civil Engineering, National Institute of Technology (Deemed University), Kurukshetra (Haryana), India. Leonardo Electronic Journal of Practices and Technologies ISSN 1583-1078

[5] P. Ramanathan, I. Baskar, P. Muthupriya , and R. Venkatasubramani. Performance of Self-Compacting Concrete Containing Different Mineral Admixtures.

KSCE Journal of Civil Engineering (2013) 17(2):465-472.

[6] Ristic, N., Grdic, Z., Curcic, G. T., Grdic, D., & Krstić, D. (2019). Properties of self- Compacting concrete produced with waste materials as mineral admixture. *Revista Romana de Materiale*, *49*(4), 568-580.

[7] Khurana, R., & Saccone, R. (2001). Fly ash in self-compacting concrete. *Special Publication*, *199*, 259-274.

[8] Ravichandran Subbarayalu. A. M. Vasumathi. P. Kalai Selvi, Performance analysis of self-compacting concrete without superplasticizer: 18 January 2017 /Accepted: 9 August 2017/Published online: 19 August 2017 © Springer International Publishing AG 2017.

[9] Ravichandran Subbarayalu. A. M. Vasumathi. P. Kalai Selvi, Performance analysis of self-compacting concrete without super plasticizer: 18 January 2017 / Accepted: 9 August 2017 / Published online: 19 August 2017 © Springer International Publishing AG 2017.

[10] Muhammad Waqas Malik and Syed Ali Rizwan (2022), Utilization of Acacia Modesta Gum Powder as Viscosity- Modifying Agent in Self-Compacting Paste Systems, Engineering Proceeding, Eng. Proc. 2022, 22, 15. https://doi.org/10.3390/engproc 2022022015.

[11] Rose Mbugua , Ramadhan Salim and Julius Ndambuki (2016), Effect of Gum Arabic Karroo as a water-reducing admixture in cement mortar, Construction Materials 5 (2016), 100-111.

[12] Abdeliazim Mustafa Mohamed, Mohd Hanim Osman, Hichem Smaoui, Mohd Azreen and Mohd Ariffin, (2018), Durability and Microstructure Properties of Concrete with Arabic Gum Biopolymer Admixture, Advances in Civil Engineering Volume 2018, Article ID 1962832, 9 pages https://doi.org/10.1155/2018/1962832.

[13] European Federation of National Associations Representing for Concrete (EFNARC), Specification and Guidelines for Self-Compacting Concrete, Association House, 99 West Street, Farnham, Surrey GU9 7EN, UK, tel: +44 (0)1252 739147 fax: +44 (0)1252 739140
www.efnarc.org.

[14] Department of the Environment (DoE), Design of Normal Concrete Mixe s(Building Research Establishment, Walford, U.K., 198.

[15] American Concrete Institute. Specifications for Structural Concrete. Pumping Aids; ACI 301-05; ACI Education Bulletin, American Concrete Institute: Farmington Hills, MI, USA, 2005.

[16] ASTM C191-01. Standard Test Method for Time of Setting of Hydraulic Cement by Vicat Needle. ASTM International, West Conshohocken, PA, USA. 2001. http://www.astm. org.

[17] ASTM C136-96a, Standard Test Method for Sieve Analysis of Fine and Coarse Aggregates, ASTM International, West Conshohocken, PA, USA, 2001. http://www.astm.org.

[18] Abrams, Duff A., Tests of Impure Waters for Mixing Concrete, Bulletin 12, Structural Materials Research Laboratory, Lewis Institute, Chicago, http://www.portcement.org/ pdf_files/LS012.pdf. 1924. 50 pages (available through PCA as LS012).

[19] Kosmatka, S. H., Kerkhoff, B., &Panarese W. C. Design and control of concrete mixtures (Vol.5420, pp. 60077-1083). Skokie, IL: Portland Cement Association. 2002.

[20] M.S. Shetty. Concrete Technology. Seventeenth edition, New Delhi, 2005.

Jouf University Science and Engineering Journal (JUSEJ) 2023; 10(2): 56- 67
Published online: Dec. 2023 (https://www.ju.edu.sa/en/jouf-university-science-and-engineering-journal-jusej/home/)
Print ISSN: 1658-6670 ***Electronic ISSN:1658-9173 (1443/5074)***

EFFECT OF MACHINING CURRENT ON THE ACCURACY OF ELECTRO CHEMICAL MASK ETCHING MACHINING OF ARRAY HOLES ON ALUMINUM SHEET

G.A.El-Awadi [1*]

[1] Department of Mechanical Engineering, Faculty of Engineering, Jazan University, Jizan 45142 KSA

***Corresponding author**

G.A.El-Awadi

Email address:

gelawdi@Jazanu.edu.sa

gaberelawdi1964@gmail.com

Submission Date: *Sept. 21, 2023*
Accepted Date: *Oct. 19, 2023*

Machining techniques include both conventional and unconventional methods for removing material. Several factors, such as material type, intended post-machining purpose, geometry, hardness, thickness, and heat effects, influence the selection of a machining method. Non-traditional machining (NTM) is a method of material removal during machining that maintains the original characteristics of the material without making any changes. Electrochemical machining (ECM) is a crucial technology used for processing challenging materials. This technique offers several advantages, such as the ability to process materials of varying hardness, the absence of a heat-affected zone, and the prevention of residual strains and cracks. ECM hole-array machining is recognized for its advantages in fabricating holes in aluminum alloys that are challenging to machine using conventional mechanical techniques. Electrochemical machining and mask etching are utilized for this purpose. The machinability of a hole array is an important consideration, especially when manufacturing parts with multiple holes in a 1 mm-thick metal plate. These factors can lead to reduced processing efficiency, increased processing costs, and heightened susceptibility to material deformation. The study aimed to investigate the process of through-mask electrochemical machining (TMECM) for hole creation through experimental methods. The experiments employed current values of 5, 10, 15, and 20 amps, a constant voltage of 5, and gap thicknesses of 20 mm. A 1-mole concentration of sodium chloride (NaCl) electrolyte was used. The research used a one-sided electrochemical process to produce a 4-hole array on an aluminum sheet. The achievement was attained by applying a current of 20 amperes.

Keywords: *Electrochemical Machining Mask Etching, Current, Volt, Etching, array holes,Electrolyte NaCl*

1. INTRODUCTION

Various techniques, including micromilling, chemical etching, and electrical discharge machining (EDM), can be employed to fabricate the flow channel array. ECM has gained popularity as a method for fabricating arrays with metallic interconnect plates in recent years. ECM provides various benefits such as reduced wear on the cathode tool, absence of burr formation, high operational efficiency, and cost-effectiveness. When implementing the Electrochemical Machining (ECM) technique, there are three primary processing methods for acquiring a flow channel array[1, 2].

This phenomenon has been observed in contemporary times. Electrochemical etching is a method that employs an electric current to

eliminate material from the surface of a metal. This process is frequently employed in the manufacturing sector to mark and label metal components. An array hole refers to an empty or unoccupied index within an array data structure. Electrochemical etching refers to a specialized technique employed for the purpose of generating arrays of small holes or features on a metal surface.[3].

ECM electrochemical machining is a non-conventional machining (NTM) procedure classified under the electrochemical category. ECM stands in direct opposition to electrochemical or galvanic coating or depositing processes. Electrochemical machining (ECM) is a process that entails the deliberate anodic dissolve of an electrically conducting workpiece at the atomic scale. This process is achieved through the use of a specifically designed tool and the passage of a high current with a relatively low voltage across an electrolyte. The electrolyte commonly employed is a water-based solution containing neutral salts, which can have different concentrations and voltage settings.[4] Material removal from a substrate can be achieved through either a chemical reaction or an etch process. Hole arrays are widely employed in various industries, such as aerospace engineering, automotive production, and the electronics sector. The materials used for these parts are typically hard metals that are challenging to cut due to their application in specialized environments. [5, 6] These parts often have numerous small holes in the thin metal plate, measuring less than 1 mm. These holes can cause various issues in the production process, including reduced efficiency, increased costs, and material deformation.[7] Electrochemical machining (ECM) is a significant technology for processing difficult materials due to its hardness independence, lack of heat-affected layers, and residual stresses. It is highly favored in manufacturing.[5, 8]

The utilization of electrochemical machining (ECM) for machining hole arrays has gained popularity owing to its various advantages. ECM technology for machining hole arrays can be classified into two main categories: Multiple electrodes are used for drilling holes with ECM and through-mask electrochemical machining. Research has been done on the use of multiple electrodes for machining hole arrays. The holes produced with ECM have sharp edges, indicating precise dissolution. ECM has potential for high precision hole array machining.[9] The multiple electrode electrochemical machining (ECM) process has been investigated to fabricate hole arrays on SS 304. The machining gap for this process has been successfully decreased to as low as 1mm. Through-mask electrochemical machining is a method that removes metal from parts of a mask-patterned workpiece, using an electrolytic cell. It is effective and economical for making arrays of holes, especially for precision applications like ink-jet printer heads. The angle of the hole's taper has a significant impact on its quality. The isotropic nature of the metal removal process during TMECM will cause the sidewall to have a certain taper, which is a critical factor to consider in the fabrication of precision hole arrays. Overall, the TMECM process has shown great potential for the fabrication of high-quality hole arrays with low processing costs. [10-12] TMECM is a process that involves dissolving the metal workpiece can be dissolved from one or both sides simultaneously using the TMECM technique. This technique has been used for machining hole arrays with low-taper angles. The double-sided TMECM is considered a symmetrical counterpart to the single-sided TMECM. Scientists have analyzed the single-sided TMECM machining process..[13] Presently, there has been no analysis conducted on the process of machining the double-sided TMECM using numerical simulation and experimentation. In traditional TMECM processes, the photoresist is applied as a mask and sticks to the workpiece. The adhesion strength of the photoresist to the workpiece surface is

significant, rendering the photoresist mask non-reusable following TMECM. Hence, it is necessary to repeat the process of applying the light-resistant coating and conducting the exposure. In this study, a modified TMECM was introduced, wherein a modeled insulating material plate coated with a metal film was employed as a mask, replacing the conventional use of photoresist. The revised procedure exhibited reduced lead time and cost-effectiveness due to the reusability of the maskThe modified TMECM process was improved by increasing the electric field and regulating voltage. This study refers to it as the double-sided TMECM mask.A copper coating is applied to an insulation plate with a pattern, serving as a reusable mask. Electrochemical etching is a method that employs an electric current to eliminate material from the surface of a metal. This process is frequently employed in the manufacturing sector to mark and label metal components. The term "array hole" refers to an empty or unoccupied element within an array data structure. Electrochemical etching refers to a specialized technique employed to produce arrays of small holes or features on a metal surface.[5, 8, 10]

The ECM technique utilizes electrochemical processes to dissolve materials at the atomic scale. The characteristics of the material used for work can be described as mechanical or physical properties. have no bearing on the rate of material removal in machining. The electrically conductive property of a material is influenced by its atomic weight, its valiancy, and its inherent electrical conductivity. ECM is capable of machining electrically conductive work materials, irrespective of their hardness, strength, or thermal characteristics. Furthermore, electrochemical machining (ECM) induces atomic-level dissolution, leading to a superior surface finish that exhibits minimal stress and lacks thermal damage.[14-16] Electrochemical machining (ECM) is utilized in various applications such as grinding, die sinking, profiles, drilling contouring, micro-machining, and trepanning.[17]

2. EXPERIMENTAL PROCEDURES

The machining current is one of the factors that can affect the precision of array hole electrochemical etching machining on aluminum sheet. The electric current utilized for machining refers to the amount required for etching metal surfaces. A study was conducted to investigate the accuracy of array hole electrochemical etching machining on aluminum sheet, specifically focusing on the influence of machining current. During the Electrochemical Machining (ECM) procedure, several reactions take place at the electrodes, specifically the workpiece (anode) and the tool (cathode), as well as within the electrolyte solution. Figure 1 depicts the electrochemical masking etching mechanism employed in the machining of aluminum sheets. Sodium chloride (NaCl) is frequently used as the electrolyte in the electrochemical machining process of aluminum. Ionic dissociation is the process by which ions separate from each other when an electric potential is applied across an electrolyte solution and water.[18]

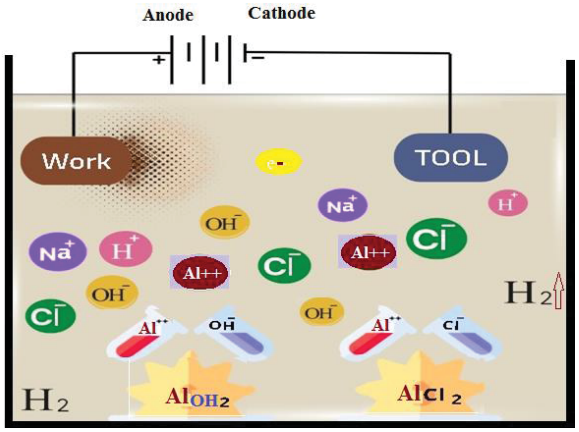

Fig. 1. schematic of electrochemical machining etching Process

When a variance in potential is applied among the workpiece (anode) and the tool (cathode), ions migrate towards their respective electrodes based

on their charge. Hydrogen ions will extract electrons from both the cathode and hydrogen gas.

$2H + + 2e- = H2$ *at the cathode* (1)

The aluminum atoms will exit the anode (work piece) in a similar manner, as

$Al = Al^{++} + 2e^{-}$ (2)

Sodium and aluminum ions both react with hydroxyl ions to create their respective hydroxides in the electrolyte.

$Na^{+} + OH^{-} = NaOH$ (3)

$Al^{++} + 2Cl^{-} = AlCl2$ (4) [12]

An experiment was conducted on an aluminum plate. This study investigates the impact of electrochemical etching on machining accuracy and tolerance variation in machined parts, specifically focusing on the correlation among the parameters of etching, specifically the voltage, and current density, and their effects. The results and discussion sections provide a comprehensive demonstration of the outcomes. The design and production of ECM mask etching rely on engineering principles, computations, and calculations in mechanical design, employing traditional design methodologies. The concepts and computations presented originate from the field of mechanical design. The process involves several steps, which will be briefly described below.

2.1 MATERIALS

This study examines the impact of varying current values on the accuracy of drilling array holes during machining as shown in figure 2. This research focuses on the parameters used for aluminum sheet material. The chemical composition of aluminum sheet 3A36 is Al 95.2, Cu0.5, Cr 0.1, Fe,0.7, Mg 0.5, Mn 1.6 and Si 0.6). The samples were prepared by cutting them into 100 x 200 x 1 mm pieces. These pieces were then ground using SiC grit sheets with increasing roughness, ranging from 120 to 400 grit. After grinding, the samples were degreased using ethanol, cleaned with distilled water, and dried using an air jet. The entire surface of the samples is masked, and only the material that will undergo machining is subsequently removed. The connection of the cathode (-) and anode (+) is necessary for the machining of the substrate. The metal blank will undergo etching following exposure to the electrolyte. Furthermore, it is ensured that the anode sheet is securely attached to the face of the cathode (metal blank). Connect the electrode and cathode ends to the DC power supply, as shown in Figures 1 and 2 as previous work[19].

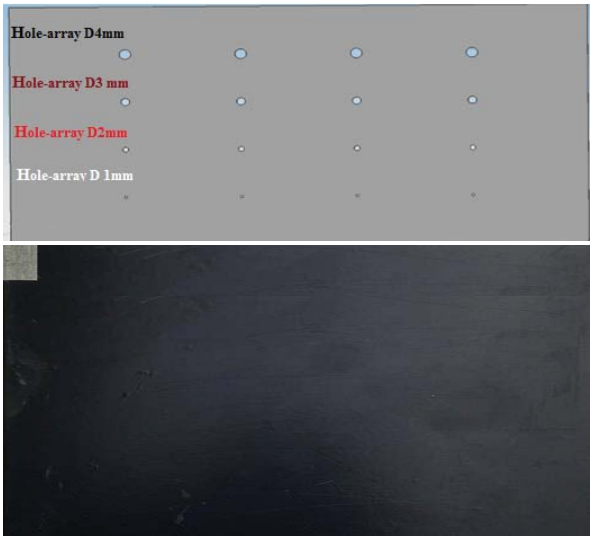

Fig. 2. sample coverd by Mask and as desierd arry holes 4x4 of Alumium sheet

Electrolyte levels there are two primary categories of electrolytes utilized in ECM etching: passivity electrolytes, the process involves using oxidizing anions, such as nitrates of sodium and sodium chlorate, along with non-passive electrolytes that contain highly reactive anions like sodium chloride. The mentioned components are essential to the procedure. Passivity electrolytes are recognized for their ability to enhance machining precision. Stray currents can generate oxide coatings and produce oxygen. In this experiment, a 1Mole/liter concentration of NaCl was selected as the electrolyte. This choice was based on a review of previous studies, which indicated that researchers

commonly used $NaClO_3$, $NaNO_3$, and NaCl solutions with different concentrations for ECM supply [20].

2.2 VOLTAGE AND CURRENT

Voltage and current play important roles in the ECM. The relationship between RMR Rate of Material Removal and machining surface accuracy is directly proportional to the increase in current and voltage. Once a certain point is reached, the increase becomes imperceptible, and this has a notable effect on the precision and quality of the output [17]. Thus, it was essential to apply the current correctly. To examine the impact of current on machining precision, the experiment will maintain a constant supply voltage of 5 volts while manipulating the current to values of 5, 10, 15, and 20 volts.

3. EXPERIMENTAL WORK

The apparatus used in this study, as depicted in Figure 3 and described in Table 1, illustrates the schematic diagram of the experimental setup for the ECM procedure.

Electrochemical machining (ECM) involves the use of masking techniques. Reactions take place at the electrodes (anode and cathode) as well as within the electrolyte during masking on a substrate. Let us consider the process of machining aluminum as an illustrative example. In electrochemical machining of aluminum, A 1M neutral solution of chloride of sodium (NaCl) is commonly employed as an electrolyte. Ionic dissociation occurs in the electrolyte and water when a potential variation is applied. Figure 1 illustrates the electrochemical reactions in a schematic manner. The machined surface exhibits a high-quality surface finish and is free from stress, as the removal of material occurs through atomic level dissociation [21].

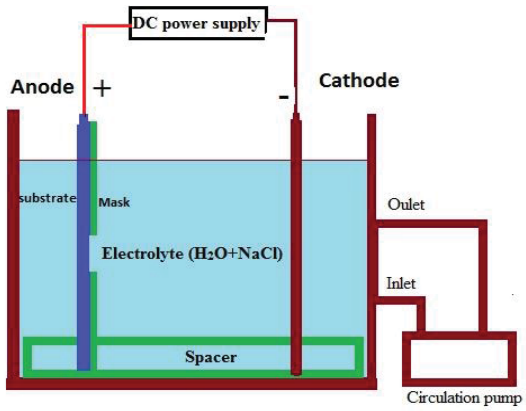

Fig. 3. Experimental set up of ECM etching process

Table. 1: *Etching set up data*

Item	Descriptions
DC Power Supply	This is an adjustable proportional single-output DC power supply capable of providing a voltage range of 0-30V and a current range of 0-24A.
Tanks	Glass sheet assembly with silicone rubber
Electrolyte	NaCl 1 Mole concentration
Digital Timer	for timing the etching process
Water pumping flow	In order to implement a cycling flow filtration system, it is necessary to filter the fluid containing electrolytes before it is reintroduced into the container in which it is stored.
Digital Timer	To measure the duration of the etching procedure.

This experiment aims to examine the production of holes with predetermined dimensions, followed by measuring and comparing the resulting diameter with the specified diameter.

We will monitor the current within a 60-minute timeframe and observe any changes that occur during the operation. It is important to mention that the molarity of the solution remains constant in all instances, specifically 1 mole of sodium chloride dissolved in 1 liters of water. We endeavor to establish the appropriate voltage levels in various operational scenarios.

4. RESULTS AND DISCUSSION

An experiment was conducted on an aluminum plate. This study investigates the impact of electrochemical etching on machining accuracy and tolerance variation in machined parts, specifically focusing on the relationship between etching parameters such as volts and Current

density refers to the electric current density refers to the value of electric current passing through a unit area that is at right angles to the path of current flow. The findings have been obtained. Presented in a comprehensive manner in the results the study includes analysis and discussion sections. The study observed a positive correlation between the machining current and the accuracy of the etched features. Increased machining currents can result in a more aggressive etching process, potentially leading to over-etching and fell accuracy.[22]

The working piece has four groups of holes, each of which has four holes of the same diameter, and holes of various diameters. The machining current is one of several variables that can impact the precision of array holes electrochemical etching processing on aluminum sheet. The quantity of electric current used to etch metal surfaces is referred to as machining current.[23]

An investigation was made into how array hole electrochemical etching on aluminum sheet affected the precision of the machining current. According to the study, increasing the machining current improved the accuracy of the etched features. This is so because increased machining currents may make the etching process more aggressive, which can result in excessive etching and a reduction in precision. The research also discovered that 0.5 A/cm2 was the ideal machining current for array holes electrochemical etching processing on aluminum plates to achieve excellent accuracy. This current produced well-defined and uniform details by striking a fair equilibrium between etching rapidity and precision.[22, 24]

The study determined that a voltage of 5 volts and a current of 20 amps were the ideal machining parameters for achieving high accuracy in array hole electrochemical etching machining on aluminum sheet. This method achieved a satisfactory equilibrium between the speed of etching and the precision, leading to the formation of distinct and consistent features. Table and Figure 4 illustrate the findings.

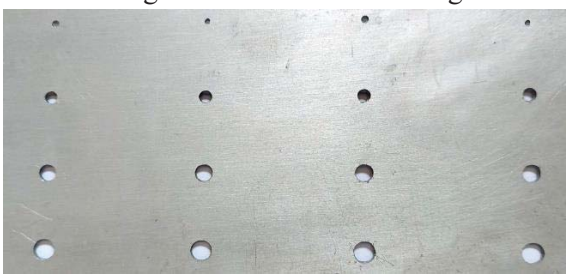

Fig. 4. Array holes 4,3,2,1 mm after machining at current 20Amp, 5 volt

The machining current is a crucial factor to consider in array hole electrochemical etching machining of aluminum sheets. By optimizing the machining current to 20 amps (Figure 5), it is possible to attain precise and clearly defined features, which hold significance in various manufacturing applications.

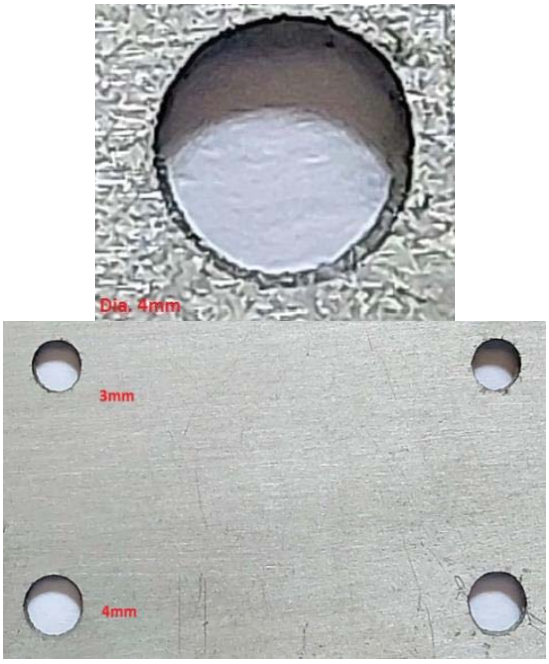

a)Hole 4mm diametr after machining b) Hole 3,4mm diametr after machining

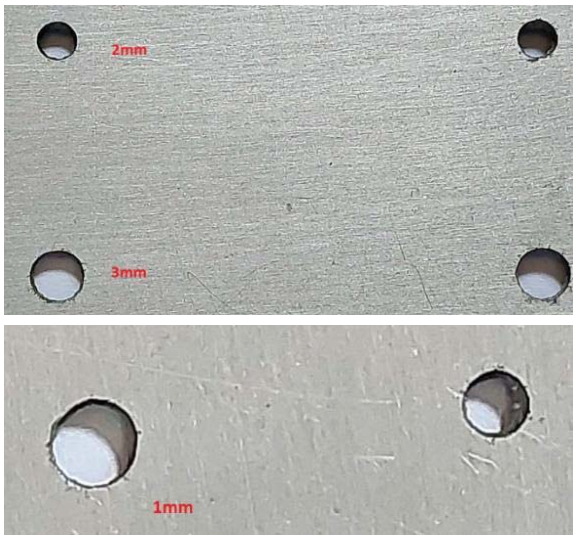

c) Hole 3,2mm diametr after machining d) Hole 1 mm diametr after machining

Fig. 5. (a,b,c,d) photograph of holes machining at V=5, I=20 time, 60 min, electrolyte 1M, gap distance 20mm

Overall, when undertaking array holes electrochemical etching processing on aluminum sheet, the machining current is a crucial factor to take into account. High accuracy and well-defined features can be obtained by controlling the machining current, which is crucial for many production applications. The dimension of the holes in a series during electrochemical etching might not match the size of the etching mask. This is due to the fact that a number of variables, including the characteristics of the metal being etched, the make-up of the solution of electrolytes, and the mask design, can affect how accurately the etching process works. [25] The diffusion of the electrolyte solution is one of the primary elements that can significantly influence the precision of the etching process. The electrolyte solution is used in the etching procedure to dissolve the metal and make the holes in the array. However, etching may proceed unevenly due to the diffusion of the electrolyte solution, varying the diameter of the holes. The design of the mask is another element that may have an impact on the accuracy of the etching procedure. The mask is used to specify the pattern of the holes in the array; if it is not made properly, the diameter of the holes may vary. For instance, improper mask alignment with the metal surface may result in etching that occurs at an angle and variances in the size of the holes. The characteristics of the metal being etched can also impact how accurately the process works. For instance, variations in the thickness or composition of the metal can affect the holes' diameter. [26]

Figures 6, 7, 8, and 9 demonstrate that the holes have not been machined to the desired depth under the current parameters of 15, 10, and 5 Amperes, 5 Volts, and a machining time of 60 minutes. The machining depth is inadequate for the sheet thickness. The machining removal rate is also influenced by the machining current.

Fig. 6. photograph of holes machining at V=5, I=15 time, 60 min, electrolyte 1M, gap distance 20mm

Fig. 7. Array holes 4,3,2,1 mm after machining at current 15Amp, 5 volt

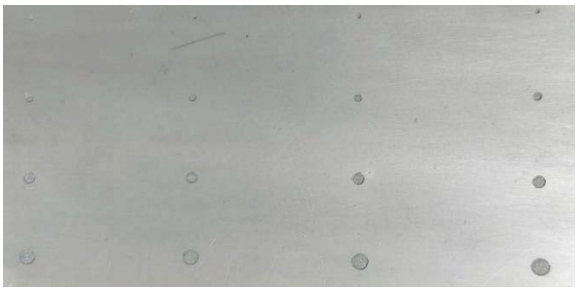

Fig. 8. photograph of array holes 1,2,3,4mm machining at V=5, I=10 time, 60 min, electrolyte 1M, gap distance 20mm

Fig. 9. photograph of array holes 1,2,3,4mm machining at V=5, I=5 time, 60 min, electrolyte 1M, Gap distance 20mm

Along with the exposed portions, nearby uncovered areas also experience deterioration. When the mask is thinner, this phenomenon is stronger. This could provide an explanation for the findings in Fig.4 (a). The mask's significant aspect ratio reduces overcut of holes during machining by inducing localization through the development of non-uniform current density [27, 28]. This phenomenon occurs due to the increased time required for machining a workpiece with uneven current density when creating holes. The isotropic characteristics of electrochemical machining can account for this phenomenon. During the initial stage of machining, materials dissolve solely along the Z-axis of the workpiece as shown in Figure 10(a,b,c,d). The uniform dissolution rate is due to an even distribution of current density on the surface, resulting in reduced overcut length. Material dissolution occurs less on the X side of the hole as machining time increases, attributed to current density and ion dissolving direction relative to cathode direction. Overcutting happens when unexposed areas near hole boundary dissolve. [29]

Due to the numerous variables that can affect the process' precision, establishing uniform hole dimensions in an array by electrochemical etching can be difficult. However, it is possible to attain a high level of accuracy and consistency in the hole diameters by carefully managing the etching conditions and improving the mask design.[30]

The setup voltage for the experiment, as shown in Figure11, is 5 v, although the actual volt is almost the same as. [28]

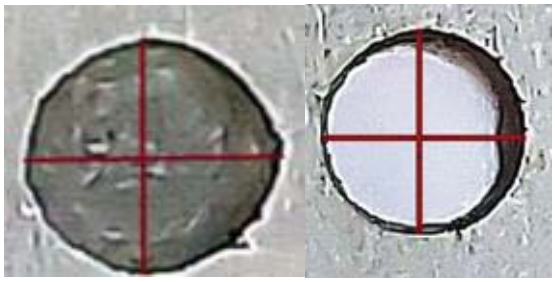

a) hole 4 mm b) hole 3mm

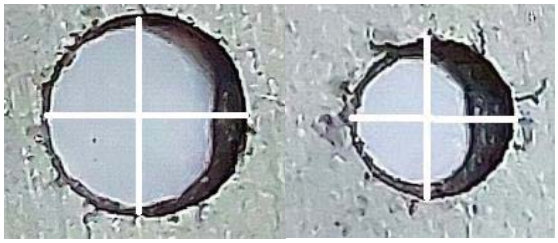

c) hole 3mm d) hole 1mm

Fig. 10. Hole diameter 4, 3, 2 and 1mm after machining

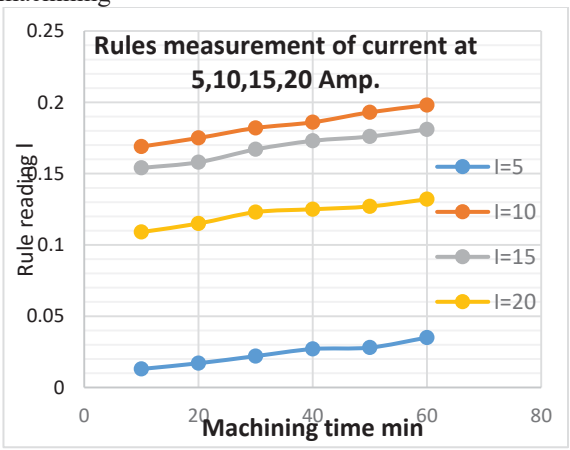

Fig. 11. Relation between setting current 5,10,15 and 20 with actual current

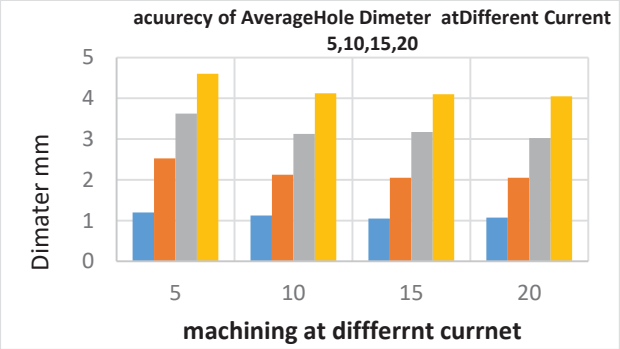

Fig. 12. Accuracy of cutting a set of holes of 1, 2, 3, and 4 mm in diameter

This layer creates a current difference, and the material's ionization is controlled by the electric current. Therefore, it's crucial to establish appropriate machining parameters that affect the double layer, such as electrolyte the concentration, IEG, and voltage[15, 29]. A diffusion layer is also created surrounding the substance of the workpiece during the electrochemical reaction. The substance dissolves more quickly with high current density than with metal ion extraction. The ions migrate more slowly through thicker diffusion layers, which takes down the dissolve. As a result, the material requires a suitable current density, which can be achieved by adjusting the voltage between both electrodes[31]. The machining of various array series of holes with diameters of 1, 2, 3, and 4 mm at various machining currents yields the best results for dimensions accuracy at currents of 15 and 20 amps, for the majority of holes with diameters of 1, 2, 3, and 4, at constant other conditions such as gap distance, volt, and electrolyte concentration as shown in Figure 11.

There are a few factors that could affect how uniformly sized the hole is during the ECM (Electrochemical Processing) cover etching process. One of the main causes is the non-uniformity of the current density distribution during the etching process. The lack of uniformity observed in this context may stem from a range of factors, including the degree of depth exhibited by the mask, the spatial separation between the face piece and the workpiece, as well as the overall shape of the mask. [31]. Another factor that could affect the size of the hole is the type of electrolytes used during the etching procedure. Changes in the conductivity and viscosity of the electrolyte could have an impact on how the distribution of current density is presently observed. and how quickly it etches. [15, 31].The diameter of the hole may also be influenced by the shape of the workpiece. Currently, if the surface of the workpiece is curved or irregular, the density concentration may not be consistent, which would result in an uneven etching rate and uneven whole diameter. [28, 31].It is essential to properly control the etching factors, such as the current density, the electrolyte material, and the mask design, in order to achieve a uniform and constant diameter of the holes during ECM mask etching. This graph demonstrates how the current is increasing over time [32].

Notably, despite all the changes, the current activities were identical to the beginning diameter. The immensity of the original work and the new, haphazard attempt are contrasted at the beginning and end. Several holes did not have the components cut due to machining variables such current, time, volt, electrolyte concentration, and gap distance because bubbles that formed during the cutting process for other holes rested on the initial hole and blocked the flow of current. Make adjustments to the experiment's conditions. Due to the diameter being larger than the mask design's own diameter, as demonstrated by the measurements made with 1 mm, 2 mm, or other precisions [33].

5. CONCLUSION

The masking electrochemical process enhances machining localization on aluminum surfaces, offering potential benefits in industries such as automotive, aerospace, machinery production, aircraft, and chemical manufacturing. Metal removal rate increasing with increasing machining current. The electrochemical machining masking (ECMM) technique works

well for small holes, but correct results require a precise mechanism. Increasing the current is important to modify the solution's temperature because if it goes up, the cutting operation will be halted. Increasing the current is important to modify the solution's temperature because if it goes up, the cutting operation will be halted. Increasing current improves drilling holes precision and speeds up removal.

6. CONFLICT OF INTEREST

The author declares no conflict of interest.

7. REFERENCES

[1] 1. Scott, S.M. and Z. Ali, *Fabrication methods for microfluidic devices: An overview*. Micromachines, 2021. **12**(3): p. 319. https://doi.org/10.3390/mi12030319

[2] 2. El-Hofy, H., *Fundamentals of machining processes: conventional and nonconventional processes*. 2018: CRC press. https://cir.nii.ac.jp/crid/1363670320111039104

[3] 3. Debnath, S., et al., *Non-traditional micromachining processes: opportunities and challenges.* Non-traditional Micromachining Processes: Fundamentals and Applications, 2017: p. 1-59. https://doi.org/10.1007/978-3-319-52009-4_1

[4] 4. Patil, P. and V.S. Jadhav, *Evaluation of Material Removal Rate Using Circular-Shaped Tube Electrode in Electrochemical Machining.* International Journal of Engineering and Technical Research, 2013. **1**: p. 30-35.

[5] 5. Wang, G.Q., et al., *Investigation of the hole-formation process during double-sided through-mask electrochemical machining.* Journal of Materials Processing Technology, 2016. **234**: p. 95-101. https://doi.org/10.1016/j.jmatprotec.2016.01.010

[6] 6. Bhattacharyya, B., *Electrochemical micromachining for nanofabrication, MEMS and nanotechnology*. 2015: William Andrew. https://books.google.com.eg/books?id=xDBAAAQBAJ&lpg=PP1&ots=YSROR-aXNp&lr&hl=ar&pg=PP1#v=onepage&q&f=false

[7] 7. Pattavanitch, J. and S. Hinduja, *Machining of turbulated cooling channel holes in turbine blades.* CIRP annals, 2012. **61**(1): p. 199-202. https://doi.org/10.1016/j.cirp.2012.03.086

[8] 8. Wang, G.Q., D. Zhu, and H.S. Li, *Fabrication of semi-circular micro-groove on titanium alloy surface by through-mask electrochemical micromachining.* Journal of Materials Processing Technology, 2018. **258**: p. 22-28. https://doi.org/10.1016/j.jmatprotec.2018.03.015

[9] 9. Guoqian, W., et al., *Improvement of machining consistency during through-mask electrochemical large-area machining.* Chinese Journal of Aeronautics, 2019. **32**(4): p. 1051-1058. https://doi.org/10.1016/j.cja.2018.06.006

[10] 10. Zhu, D., et al., *Electrochemical micromachining of microstructures of micro hole and dimple array.* CIRP annals, 2009. **58**(1): p. 177-180. https://doi.org/10.1016/j.cirp.2009.03.004

[11] 11. Choi, W.-K., et al., *Quadrilateral micro-hole array machining on Invar thin film: Wet etching and electrochemical fusion machining.* Materials, 2018. **11**(1): p. 160. https://doi.org/10.3390/ma11010160

[12] 12. Rathod, V., B. Doloi, and B. Bhattacharyya, *Electrochemical Micromachining (EMM): Fundamentals and Applications.* Non-traditional Micromachining Processes: Fundamentals and Applications, 2017: p. 275-335.

[13] 13. Liu, Y., W.L. Zeng, and Z.L. Wang. *Duplication error and repeated error analysis of micro-hole array fabrication by EMM*. Trans Tech Publ. https://doi.org/10.4028/www.scientific.net/AMR.113-116.1914

[14] 14. Mallick, U., *Estimation of MRR using U-shape electrode in electrochemical machining.* 2009. https://core.ac.uk/download/pdf/53187119.pdf

[15] 15. Leese, R.J. and A. Ivanov, *Electrochemical micromachining: An*

introduction. Advances in Mechanical Engineering, 2016. **8**(1): p. 1687814015626860. https://doi.org/10.1177/1687814015626860

[16] 16. Paul, L., J. Babu, and J. Paulo Davim, *Non-conventional micro-machining processes.* Materials Forming, Machining and Post Processing, 2020: p. 109-139. https://citations.springernature.com/item?doi=10.1007/978-3-030-18854-2_5

[17] 17. Rajurkar, K.P., et al., *New developments in electro-chemical machining.* CIRP annals, 1999. **48**(2): p. 567-579. https://doi.org/10.1016/S0007-8506(07)63235-1Get rights and content.

[18] 18. Sundaram, M.M. and K.P. Rajurkar, *Electrical and electrochemical processes.* Intelligent Energy Field Manufacturing and Interdisciplinary Process Innovations, 2010: p. 173-212. https://books.google.com.eg/books?id=grE1yfWhHCAC&lpg=PA173&ots=0IzGRin4rB&dq=Sundaram%20MM%2C%20Rajurkar%20KP%20(2010)%20Electrical%20and%20electrochemical%20processes.%20Intelligent%20Energy%20Field%20Manufacturing%20and%20Interdisciplinary%20Process%20Innovations%3A%20173-212.&lr&hl=ar&pg=PA173#v=onepage&q&f=false

[19] 19. G.A.El-Awadi, *A novel approach to electrochemical machining etching using solar energyat a low cost for steel, stainless steel, and aluminum sheets with differentelectrolyte concentrations.* European Chemical Bulletin, 2023. **12**(10): p. 10702-10719. doi: 10.48047/ecb/2023.12.10.759

[20] 20. Mahamood, R.M. and E.T. Akinlabi, *Advanced Noncontact Cutting and Joining Technologies*. 2018: Springer. https://link.springer.com/content/pdf/10.1007/978-3-319-75118-4.pdf

[21] 21. Kumar, J., S. Mandal, and N. Mahato, *Study of Electro Chemical Machining Etching Effect on Surface Roughness and Variation with Chemical Etching Process.* http://www.copen.ac.in/proceedings/copen10/copen/150.pdf

[22] 22. Snoeys, R., F. Staelens, and W. Dekeyser, *Current trends in non-conventional material removal processes.* CIRP annals, 1986. **35**(2): p. 467-480. https://doi.org/10.1016/S0007-8506(07)60195-4

[23] 23. Arab, J., et al., *Fabrication of multiple through-holes in non-conductive materials by Electrochemical Discharge Machining for RF MEMS Packaging.* Journal of Materials Processing Technology, 2019. **271**: p. 542-553. https://doi.org/10.1016/j.jmatprotec.2019.04.032

[24] 24. Hyacinth Suganthi, X., U. Natarajan, and N. Ramasubbu, *A review of accuracy enhancement in microdrilling operations.* The International Journal of Advanced Manufacturing Technology, 2015. **81**(1-4): p. 199-217. https://link.springer.com/article/10.1007/s00170-015-6900-1

[25] 25. Datta, M., *Microfabrication by electrochemical metal removal.* IBM Journal of Research and Development, 1998. **42**(5): p. 655-670. **DOI:** 10.1147/rd.425.0655

[26] 26. Madore, C., O. Piotrowski, and D. Landolt, *Through-mask electrochemical micromachining of titanium.* Journal of the Electrochemical Society, 1999. **146**(7): p. 2526. **DOI** 10.1149/1.1391966

[27] 27. Jin, D.-s., K.-h. Chun, and E.-s. Lee, *Analysis of the current density characteristics in through-mask electrochemical micromachining (TMEMM) for fabrication of micro-hole arrays on invar alloy film.* Chinese Journal of Aeronautics, 2017. **30**(3): p. 1231-1241. https://doi.org/10.1016/j.cja.2016.10.021

[28] 28. Tsai, T.H., M.Y. Lin, and W.L. Huang, *The optimization of parameters using Taguchi-method in through-mask electrochemical machining.* Sādhanā, 2021. **46**: p. 1-7. https://link.springer.com/article/10.1007/s12046-021-01606-3

[29] 29. Jin, D.-s., K.-h. Chun, and E.-s. Lee, *Analysis of the current density characteristics.* 2016. https://doi.org/10.1016/j.cja.2016.10.021

[30] 30. Ryu, H.-Y., et al., *Fabrication of stainless steel metal mask with electrochemical fabrication method and its*

improvement in dimensional uniformity. Electronic Materials Letters, 2019. **15**: p. 7-17. https://link.springer.com/article/10.1007/s13391-018-0096-0

[31] 31. Liao, Z., et al., *Surface integrity in metal machining-Part I: Fundamentals of surface characteristics and formation mechanisms.* International Journal of Machine Tools and Manufacture, 2021. **162**: p. 103687. https://doi.org/10.1016/j.ijmachtools.2020.103687

[32] 32. Datta, M., *Micromachining by electrochemical dissolution.* Micromach. Eng. Mater, 2002: p. 239-276. https://books.google.com.eg/books?id=Jv3BpQNfb_oC&lpg=PA239&ots=hII-oFaRZ0&dq=Datta%20M%20(2002)%20Micromachining%20by%20electrochemical%20dissolution.%20Micromach%20Eng%20Mater%3A%20239-276.&lr&hl=ar&pg=PA239#v=onepage&q&f=false

[33] 33. Zhang, H., et al., *Advances in precision micro/nano-electroforming: A state-of-the-art review.* Journal of Micromechanics and Microengineering, 2020. **30**(10): p. 103002. **DOI** 10.1088/1361-6439/aba017

Jouf University Science and Engineering Journal (JUSEJ) 2023; 10(2): 68- 75
Published online: Dec. 2023 (https://www.ju.edu.sa/en/jouf-university-science-and-engineering-journal-jusej/home/)
Print ISSN: 1658-6670 ***Electronic ISSN:1658-9173 (1443/5074)***

Design and Implementation of solar Powered Engine for a Prototype Vehicle

Ali S. Al-Shahrany[1*], and Ahmed S. A. Hassan [1*]

[1] Mechanical Engineering Department, Jazan University, KSA, P. O. Box 706, Jazan 45142

***Corresponding author**

Ali S. Al-Shahrany

Email address:

aalshahrany@jazanu.edu.sa

Submission Date: *Sept. 28, 2023*
Accepted Date: *Oct. 20, 2023*

Environmental pollution from car exhaust has become a problem affecting the whole world. As well known, Combustion processes in reciprocating engines (SI & CI Engines) are commonly regarded as one of the most significant sources of hydrocarbon emissions. So, in order to maintain a decent healthy environment for communities while obtaining appropriate sustainable energy, an alternative must be considered to power such engines with clean and renewable solar energy. In this research, a vehicle completely powered by energy stored in lead-acid batteries was designed and manufactured. These batteries are charged while the car is in the sun, using an array of solar panels with photovoltaic cells that convert sunlight into electrical energy. Which completely eliminates dependence on fossil fuels and is non-polluting to the environment because it does not produce gas emissions. The car is designed to accommodate a passenger, and operate at different speeds up to 60 km/h. The principles of force, motion and aerodynamics were defined and implemented for a fully functioning prototype car. It was found that the solar panels used in this model create the same amount of power as the battery bank and the MPPT charge controller works to "boost" the current of the solar system. The maximum input voltage is specified such that the PV array is capable of generating a voltage or current that exceeds the input voltage and the rated current of the DC charge controller is at least 125% of the PV output short circuit current.

Keywords: *vehicle; batteries, solar panels; photovoltaic cell; fossil fuels, gas emissions*

1. INTRODUCTION AND LITERATURE REVIEW

Recently, the world has been living with problems of high environmental pollution and a significant rise in atmospheric temperature. Most of these problems come from the car exhaust that uses fossil fuels. Therefore, many researchers are trying to find alternatives to these cars and replace them with those that run on electricity or solar energy. It is one of the solutions to protect the environment from pollution. In the next few years, the use of clean energy will increase to reach a carbon-free zone (Ali, et al. 2023, Kamran, et al. 2023, Ahmed, et al. 2022, and Ahmed et al. 2021). Photovoltaic modules, solar tube batteries, and BLDC are the main components of mechanical construction for solar-powered vehicles (Vijay, and Bhoop 2021). El-Sharkawy et al. (2015) developed the solar car to reach a speed of 30 kilometers per hour on a single charge, which takes about 18 hours. Alnunu et al. (2012) develops a BLDC motor car that uses high-efficiency, small-area solar panels. A viable commercial solar car prototype is being developed by Ahmed et al. (2014), Ashrafee et al. (2014), Kkan et al (2014), and Yesef et al. (2013). Also, Ashrafee (2014) designed a DC motor with a power of 15 horsepower, 3200 revolutions per minute, and 72 volts, and he chose a battery that

consisted of a series of eight 8-volt lead-acid batteries, with a total of 64 volts. Vincent, and Kamalakkannan (2013) constructed a solar car engine and uses batteries, brakes, and sensors to provide care, stability and safety.

But before preparing the basic components of the solar car, calculations of the power, torque and voltage required to choose the motor and batteries, which are two of the most important components of the electrical system, must be completed (Niranjan et al. 2023, Piera 2013, Al-Shahri et al. 2020, Alabdali, et al. 2020, Mohd et al. 2013, and Weis et al. 2014). Smart charging for electric vehicle owners cuts costs by up to 60% (Valipour et al. 2022) and EV batteries play an active role in charging and storing energy for injection into the power grid. The method of charging these electric vehicles is one-way or two-way with EV batteries (Umoren and Shakir 2020), it requires multi-directional electricity and exchanges power between the grid and the battery (He et al. 2021, Amjad et al. 2018, Sadeghian et al. 2022, Kumar et al. 2021, Subramaniam et al 2020). It is injected from the grid into the EV, called G2V, requires one-way electric chargers. G2V, has higher reliability and is easier to control.

2. VEHICLE DESIGN AND MATHEMATICAL ANALYSIS

Due to the desire to produce a highly efficient solar car, the structure was made of lightweight materials with a high level of safety and simplicity in design. During the assembly of the current space frame car body and the welding work of the series of basic and small parts, gaps were left between each element to unite and form a larger frame. To give the whole body structure stability and rigidity, a pair of longitudinally extended channels and several cross members were made into the bodywork. The basic structure is constructed with a rectangular tube-like fiberglass backbone connecting the front and rear axles together so that the space inside the frame is utilized to house the drive shaft and each end of the frame is connected to the drive train, engine and suspension. The tubes are placed in different directions to give mechanical strength against a variety of forces. Welded together and positioned in different directions with a robust frame behind the two doors, these tubes form an intricate structure to provide the strength required by high-speed sport utility vehicles. The current car body was designed using the Solid Work program. In the current work, the sum of the loads on the front axle was considered equal to the sum of the loads on the front wheels, and the weight on the rear axle was considered to be equal to the sum of the weights on the two rear wheels, and thus the entire weight of the car is distributed over both axles, and the distance between the two axles is the wheelbase. The control unit for this vehicle is designed to manage and transmit the required current and voltage to the engine when the electric accelerator pedal is pressed to give the required current from the batteries that are charged by solar panels, which in turn feed the engine shaft via a motor to move the wheels.

It must be noted here that the power required for drive the present vehicle is depending on three factors. Those are the rolling resistance, Fr in Newton, which can calculate as Cr∗m∗a. Where, Cr is coefficient of rolling resistance, m is mass of vehicle in (kg), and a is acceleration of gravity in (m/s), which estimated as 95.05 N. The torture is estimated as 45 km\h, and the power as 1188.12Watts. On the other hand, the gradient resistance, F_g (F_g=$m \times a \times \sin\theta$), where, a, is acceleration of gravity in (m/s), θ is angle of inclination. Then the radiant power is evaluated by 382.3 W. The aerodynamic drag force, (F_d, =$12\times\rho_a\times V_2\times C_a\times A_f$), where ρ is the air density, V is vehicle velocity, C_a is air resistance coefficient, Then, the aerodynamic power required is estimated at 755.5 W, and the vehicle total required power is about 4000W. The driving gear is the gear that the prime mover rotates, whereas the driven gear is the gear that the driving gear

pushes (or drives) into rotation. The connection between the speed of the driving and driven gears in a gear set is known as a gear ratio. The correlation between the driving speed and the driven gears in the gear set is known as the gear ratio which was taken as 4.9 with engine speed equal 4300 rpm. Finally, two motor bases were installed. The DC output power of the solar modules used in the motor test conditions was calculated to be approximately 365 watts, which is obtained from several solar modules in addition to a storage battery and an inverter.

3. CALCULATING THE VEHICLE'S ENERGY NEEDS FROM SOLAR PANELS

To provide the amount of energy needed to operate the vehicle for 5.5 hours of charging per day and average daily solar radiation in the Jazan region. It turns out that this cart needs 2 solar panels with a capacity of 250w, a type of polysilicon, with a weight 17.8 kg and dimensions 1640 x 992 x 35 mm. The voltage must be 60 volts so that the panels are connected in series with the control unit to prevent the array from overcharging the batteries, or through a research charging regulator that can control the maximum input voltage, so that the photovoltaic array is not able to generate a voltage or current that exceeds the input voltage, and that it The rated current of the DC charge controller is at least 125% of the PV circuit output current. Figure 1 shows the methodology of present solar powered car. The vehicle battery charger consists of three stages: constant current, constant voltage, and floating charge to extend the life of the device. Here, lead-acid batteries (Seal\Gel\Flooded) were used, where the MPPT charge controller works to "boost" the current of the solar system, as the solar panels produce the same amount of energy generated by the battery bank, and we must mention here that the voltage generated by the solar unit must be reduced to a level that can charge the battery stably.

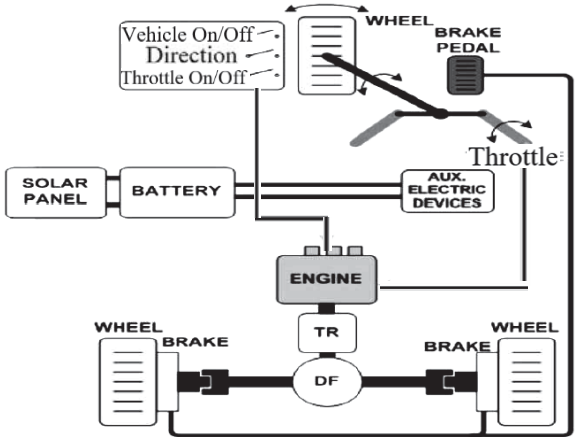

Fig. 1. Methodology layout of present solar powered vehicle

The electrical voltage produced by two solar panels is calculated as follows: Number of panels x volatile organic compounds x safety rate = 2 x 37.84 x 1.25 = 94.6 volts, and the current intensity is the power generated by the breadboard in volts = 50048 = 10.41 amps. So the battery capacity is as follows: Power of one panel x number of panels = 250 x 2 = 500 watts. The charging is as follows: safety x charging current = 2 x 1.25 x 10.42 = 26.04 ≃ 30 amps. Figure 2 shows two motors to move the vehicle with a power of 2 Kw, 12 voltages, 75 Ah, 22.7kg weight and size of 25cm x 16.7cm x 22.9cm.

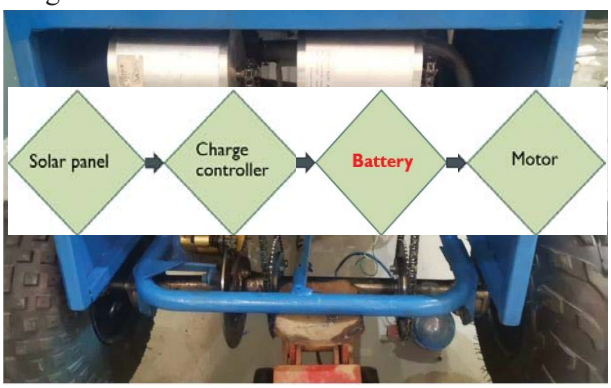

Fig.2. Back view of the vehicle: two motors were used

4. SOLAR PANEL SPECIFICATION

In this work, the three batteries were connected in series, where the voltage (Vamp) is collected, the current (Imp) remains constant, and the vehicle receives a voltage of 60 volts. A technology has been developed for the battery to

prevent its charge from draining or discharging by connecting it to a charge control device such as a charge regulator or battery regulator. The maximum input voltage for charge controllers is specified so that the PV array is capable of generating a voltage or current exceeding the input voltage and limits are made on the charge controller such that the input current or output current is not less than 125% of the PV short circuit output current.

Because the MPPT controller is not expected to be 100% efficient, but closer to 92-95%, therefore, if the V_{mp} of the solar system in use exceeds (battery bank voltage), the current boost is proportional to the voltage difference. Therefore, as shown in Fig. 3, the voltage generated by the solar module must be reduced to a level that can charge the battery in a stable manner, while the current is increased in proportion to the decrease. Figure 4 show the last design of a complete present vehicle. The total cost of the vehicle was calculated and was estimated at approximately 20 thousand Saudi riyals to complete the project well.

Fig. 3. Battery arrangement with MPPT controller

Fig.4. Present solar powered vehicle (final view)

5. RESULTS AND DISCUSSIONS

The vehicle was tested in the laboratory, and the engine speed was represented as a function of the rate of energy consumption, as shown in Figure 5 which indicates remarkable increase in the energy consumed by increasing the speed of the vehicle. Figure 6 represent effect of motor speed on battery time which is clearly show that at motor speed of 800 rpm gives the best battery time. The higher the energy consumption, the shorter time it takes to drive the motor, and so the solar panels will be used to charge the battery. The higher the energy consumption, the shorter time it takes to drive the motor, and so the solar panels will be used to charge the battery. It is observed that the volt is high and the current is low in the morning owing to the effect of heat. The current is higher and the volt is lower as the temperature rises as shown in Fig. 7. Figure 8 shows the watt obtained from sunshine will rise in the early hours of the day, resulting in better and faster battery charging. The rate of consumption of electrical energy in the batteries by the motor.

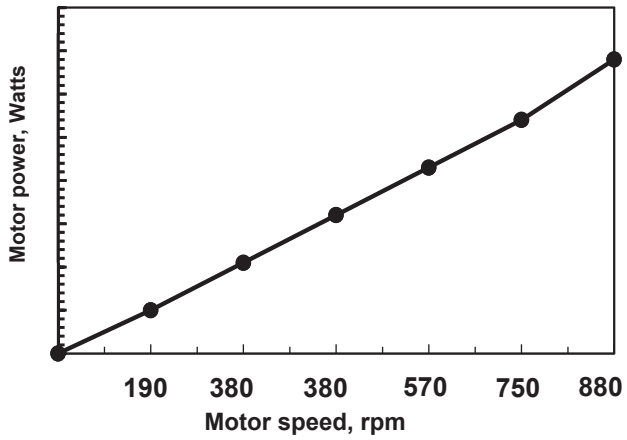

Fig. 5. Effect of motor speed on power

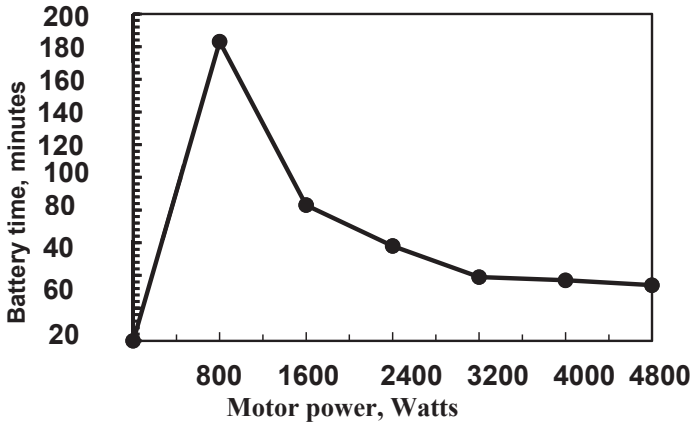

Fig. 6. Effect of motor speed on battery time

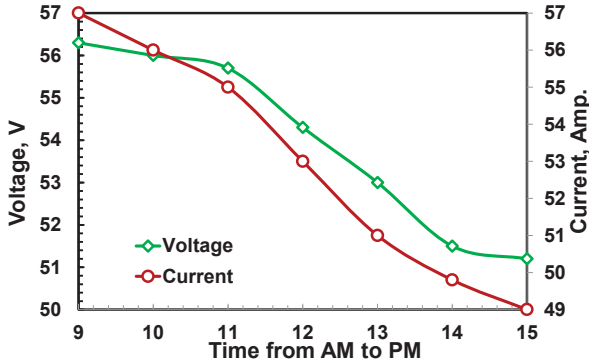

Fig. 7. Effect of time on current and voltage

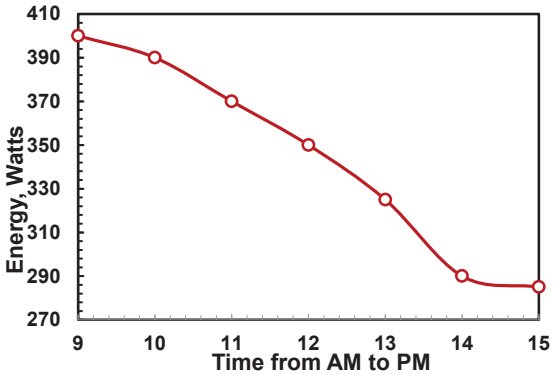

Fig.8. Effect of time on battery energy

6. CONCLUSIONS

A study to investigate how to use sustainable, clean solar energy to power a vehicle engine with standard appropriate design has been done. A fully solar-powered car was designed, fabricated, and tested. All design criteria that have to be done to produce a solar-powered motor have been considered. This car passed all technical and security tests. In this design, lead-acid batteries were used instead of lithium due to the high temperatures in the Jazan region in southern Saudi Arabia, to ensure the safety of the product. Thermal insulators have been used for lithium batteries to secure the product and increase its efficiency in the future by reducing the weight of the batteries and improving their efficiency.

7. REFERENCES

[1] Ali A., Mohamed S., Khalid Y., Mahmoud M., & Mohamad K., (2023). A Comprehensive Review of Electric Vehicle Charging Stations with Solar Photovoltaic System Considering Market, Technical Requirements, Network Implications, and Future Challenges, MDPI, 15(10), 1-26, doi.org/10.3390/su15108122.

[2] Kamran T., As'ad A., Mohsen G., & Sayyad N. (2023). A Comprehensive Review of Electric Vehicles in Energy Systems: Integration with Renewable Energy Sources, Charging Levels, Different Types, and Standards, 16(2), 630; https://doi.org/10.3390/en16020630.

[3] Ahmad T., Gamal H., Salem Z., & Saeed A. (2022). Optimal design and techno-economic analysis of a hybrid solar-wind power resource: a case study at Al Baha University, KSA, International Journal of Energy Production and Management, 5(4):13-34, doi: 10.2495/EQ-V7-N1-13-34, Vol. 7, March 2022.

[4] Ahmad F. (2021). Design and Implementation of Solar Powered Electric Vehicle for On-Campus University Applications, International Journal of Engineering Research and Technology, ISSN, 9(14), 0920-927, doi: 10.17577/IJERTV10IS100132.

[5] Vijay P., & Bhoop S. (2021). A Review on Solar Powered Electric Vehicle", International Journal of Innovative Research in Technology, ISSN: 2349-6002, 8(4), 4-9, https://ijirt.org/master/publishedpaper/IJIRT152663_PAPER.pdf.

[6] El-Sharkawy R., Mourad A., Salem M., & Youssef M. (2015). Construction of an Electric Vehicle Implemented in Egypt. International Journal of Eng. Research and Applications, 1(2), 92-10, https://ijera.com/papers/vol%201%20issue%202/012092101H.pdf.

[7] Alnunu N., Said S., Al-Sharman S., Al-Ibrahimi A., AbdulAziz A., Al Hellabi M., & Benammar M. (2012), Design of Qatar University's first solar car for Shell Eco-marathon competition, 1st International Conf. on Renewable Energies and Vehicular Technology, 49-54. IEEE, doi:10.1109/REVET.2012.6195247.

[8] Ahmed S., Zenan H., & Rahman M. (2014). A two-seater light-weight solar powered clean car: Preliminary design and economic analysis, 3rd International Conf. on the Developments in Renewable Energy Technology, 1-7, IEEE, doi:10.1109/ICDRET.2014.6861646.

[9] Ashrafee F., Morsalin S., & Rezwan A., (2014). Design and fabrication of a solar powered toy car", IEEE, International Conference on Elect. Eng. and Information & Communication Technology, 1-6.

[10] Khan A., Rahman S., Afgani K., & Fahim E., (2014). Solar car", Doc. dissertation, BRAC University, doi:10.13140/RG.2.2.10894.31046.

[11] Yesil E., Onol O., Icke A., & Atabay O., (2013). Strategy optimization of a solar car for a long-distance race using Big Bang-Big Crunch optimization, IEEE 14th Int. Symp. on Computational Intelligence and Informatics (CINTI) (521-526).

[12] Vincent V., & Kamalakkannan S., (2013). Advanced hybrid system for solar car, International Conference on Computation of Power, IEEE, Energy, Information and Communication (ICCPEIC), 21-32, doi: 10.1109/ICCPEIC.2013.6778515.7

[13] Niranjan D., Tara C. & Bhim S., (2023). A review of renewable energy based power supply options for telecom towers, 3rd International Conference on the Developments in Renewable Energy Technology, 1-7,

https://link.springer.com/article/10.1007/s10668-023-02917-7.

[14] Piera J., (2013). Improving the Global Energy Industry by Integrating Macro-Technologies: Challenges and Opportunities for Corporations, Energy and Power Engineering, 5(10), 604-621, doi: 10.4236/epe.2013.510067.

[15] Al-Shahri A., Ismail B., Hannan A., Lip H., Al-Shetwi Q., Begum, R., & Soujeri E., (2020). Solar photovoltaic energy optimization methods", challenges and issues: A comprehensive review, Journal of Cleaner Production, 15(18), 13916, doi.org/10.3390/su151813916.

[16] Alabdali Q., Bajawi A., & Nahhas M., 2020, "2014Review of Recent Advances of Shading Effect on PV Solar Cells Generation", Sustainable Energy 8(1):1-15, doi: 10.12691/rse-8-1-1.

[17] Mohd S., Santosh W., Suvarna L., Pooja F., & Anil T., (2017). A review paper on electricity generation from solar energy, International Journal for Research in Applied Science & Engineering Technology (IJRASET), ISSN: 2321-9653; 8(v):1775, doi: 10.22214/ijraset.2020.5286.

[18] Weis, Allison & Jaramillo, Paulina & Michalek, J., (2014). Estimating the potential of controlled plug-in hybrid electric vehicle charging to reduce operational and capacity expansion costs for electric power systems with high wind penetration, Applied Energy, Elsevier, 115(C), 190-204, doi: 10.1016/j.apenergy.2013.10.017.

[19] Valipour E., Nourollahi R., Taghizad-Tavana K., Nojavan S., & Alizadeh A., (2022). Risk Assessment of Industrial Energy Hubs and Peer-to-Peer Heat and Power Transaction in the Presence of EVs, Energies 15(23), 8920; https://doi.org/10.3390/en15238920.

[20] Umoren A., & Shakir Z., (2022). Electric Vehicle as a Service (EVaaS): Applications, Challenges and Enablers, Energies, MDPI, 15(19), 1-23, doi.org/10.3390/en15197207.

[21] He T., Lu D., Wu M., Yang Q., Li T., & Liu Q., (2021). Four-Quadrant Operations of Bidirectional Chargers for EVs in Smart Car Parks: G2v, V2g, and V4g", Energies 14(1):181, doi: 10.3390/en14010181.

[22] Amjad M., Ahmad A., Rehmani M., & Umer T., (2018). A Review of EVs Charging: From the Perspective of Energy Optimization, Optimization Approaches, and Charging Techniques, Transp. Res. Part D Transp. Environ., 62(9):386-417, doi: 10.1016/j.trd.2018.03.006.

[23] Sadeghian O., Oshnoei A., Mohammadi-ivatloo B., Vahidinasab V., & Anvari-Moghaddam A., (2022). Comprehensive Review on EVs Smart Charging: Solutions, Strategies, Technologies, and Challenges, Journal of Energy Storage, 54, 105241, doi.org/10.1016/j.est.2022.105241.

[24] Kumar S., Usman A., & Rajpurohit, S., (2021). Battery Charging Topology, Infrastructure, and Standards for Electric Vehicle Applications: A Comprehensive Review, IET Energy System, Integr., 3, 381-396, doi.org/10.1049/esi2.12038.

[25] Subramaniam M., Solomon M., Nadanakumar V., Anaimuthu S., & Sathyamurthy R. (2020). Experimental Investigation on Performance,

Combustion and Emission Characteristics of DI Diesel Engine Using Algae as a Biodiesel, Energy, 6, 1382-1392. doi:10.1088/1757-899X/1130/1/012083.

[26] Abid M., Tabaa M., Chakir A., & Hachimi H., (2022). Routing and Charging of EVs: Literature Review, Energy Rep., 8, 556–578. doi.org/10.1016/j.egyr.2022.07.089.

Jouf University Science and Engineering Journal (JUSEJ) 2023; 10(2): 76- 84
Published online: Dec. 2023 (https://www.ju.edu.sa/en/jouf-university-science-and-engineering-journal-jusej/home/)
Print ISSN: 1658-6670 ***Electronic ISSN:1658-9173 (1443/5074)***

Potentiometric and thermodynamic studies of N, N'-bis(1H-pyrrol-2-ylmethylene) diethylenetriamine (BPDT) and its Cu^{2+} , Ni^{2+} and Co^{2+} complexes

Aly A. A. Soliman[1*] and K.F. Hassan [1]

[1] Chemistry Department, College of Science, Jazan University, P. O. Box 706, Jazan 45142, Kingdom of Saudi Arabia

***Corresponding author**

Aly A. A. Soliman

Email address:

asoliman@jazanu.edu.sa

Submission Date: *Oct. 09, 2023*
Accepted Date: *Oct. 19, 2023*

The protonation constants of BPDT and the stability constants of a number of transition metal complexes have been studied potentiometrically at 20, 25, 30, and 40°C, in water solution at 0.1 M ionic strength (KNO_3), using the mole ratios (1:1) and (2:1), (L:M), where M = Cu^{2+}, Ni^{2+}, and Co^{2+}. The calculations are performed by operating the computer program SUPERQUAD. From the values of the stability constants of the complexes at the different four temperatures, the thermodynamic functions ΔG, ΔH, and ΔS were evaluated. The order of stability of the complexes is in agreement with the Irving - Williams order. (ML) complexes species in the case of Cu(II) and Ni(II) and (ML_2) in the case of Co(II) were found to be the most sTABLE complexes species. This may be attributed to their large positive entropy values observed, more over their large negative ΔG values.

Keywords: *Potentiometric Titrations – Stability Constants – Complexes – Schiff bases*

1. INTRODUCTION

Schiff-base ligands have performed a significant role in the evolution of contemporary coordination chemistry, Because of their importance in a variety of interdisciplinary study domains [1], particularly as corrosion inhibitors [2], catalysts for activation of small molecules [3], and in biological systems [4-11]. These wide applications of Schiff bases have generated a great deal of interest in metal complexes, kinetics of formation and hydrolysis as well as electronic spectra and acidity constants. Tetradentate Schiff bases, 'Salen' (salen, N,N′-bis(salicyldene)ethylenediamine) or 'salen-type' ligands and their complexes have received continuous and intensive attention in many fields of research. Contrarily, there is little information available regarding the ligand behavior of comparable compounds produced from pyrrole 2-carboxaldehyde and the characteristics of their complexes [12-13].

The present work reports the results of potentiometric investigation on BPDT and its complexes of Cu^{2+}, Ni^{2+} and Co^{2+}. The potentiometric method is used to determine the protonation constants of the free ligand as well as the stoichiometries and the stability of its complexes in the appropriate solutions and with the two mole ratios, (1:1) and (2:1), (L:M). The computer program SUPERQUAD is used to evaluate these constants. The stability constants of these complexes are calculated at four different temperatures 20, 25, 30 and 40°C in order to investigate the effect of temperature on their stability, and from the data obtained, the thermodynamic functions ΔG, ΔH and ΔS are evaluated.

2. EXPERIMENTAL

2.1. MATERIALS AND SOLUTIONS.

Pyrrole-2-carboxaldehyde was purchased from Koch Light Laboratories LTD-England and was recrystallized from hexane before use. (M.P. = 43 - 46°C) and Diethylenetriamine (dien) was purchased from Merck, dried over potassium hydroxide, and distilled before use (105-106°C/8 mm). All other reagents used were of analytical grade (Merck, Darmstadt, Germany). Carbonate-free KOH was prepared in double-distilled water, and standardized potentiometrically with potassium hydrogen phthalate solution. 1M KNO_3 solution was prepared in double-distilled water. Stock solutions of the metal salts, were prepared in double-distilled water and standardized by complexometric EDTA titration [14]. Stock solutions of BPDT (0.01 M) were prepared by dissolving an appropriate amount of a given ligand in double-distilled water.

2.2 PREPARATION OF THE LIGAND N,N'-BIS(1H-PYRROL-2-YLMETHYLENE) DIETHYLENETRIAMINE (BPDT).

BPDT was prepared by the following method which is different from that already described [15], a solution of 1.902 g (20 mmol) of pyrrole-2-carboxaldehyde in 50 ml of chloroform was added dropwise with constant stirring to 1 ml (10 mmol) of dien in 50 ml of chloroform over 1.5 hour at room temperature. The solution was stirred for some hours turning from pale yellow to dark yellow. Then the solvent was removed under reduced pressure using a rotatory evaporator to give a yellow solid ligand, which was recrystallized from benzene to give a fluffy pale pink solid of BPDT m.p. 120-121°C. Found: C, 65.85; H, 7.44; N, 26.78; Calculated for $C_{14}H_{19}N_5$: C, 65.34; H, 7.44; N, 27.21%; molecular ion in the mass spectrum, m/e: Found 257.15; Calculated 257.30.

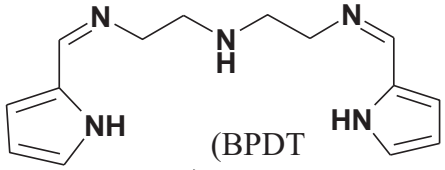

(BPDT

2.3 INSTRUMENTS.

The potentiometric measurements were performed with Metrohm 702 SM Titrino, Metrohm Ltd. CH-9101 Herisou, Switzerland. The titrino was supplied by 727-titration stand, with a built-in magnetic stirrer. The electrode, combined pH glass electrode, was calibrated using aqueous standard buffers of pH 4.0 and 7.0. The titrations were performed in a double-wall glass cell through the outer jacket of which water circulated from a controlled temperature

bath. The temperature was controlled with the thermostat Digiterm100, J. P. Selecta, S. A., Barcelona, Spain, with a temperature uncertainty of (0.1 °C).

2.4. COMPUTER PROGRAMS.

VESUV, Verification Support for Validation, is PC software for Metrohm titrators allowing the optimal cooperation between the titrino and PC. SUPERQUAD 91, the calculations on the pH-metric data were performed with the aid of the SUPERQUAD [16] computer program.

2.5. POTENTIOMETRIC MEASUREMENTS.

The following mixtures were prepared to measure the protonation constants of BPDT and titrated against standard CO_2-free potassium hydroxide (0.090 M) solution. (i) (2 X 10^{-2}) M HNO_3 + (4 X 10^{-3} M) L, (ii) (1.5 X 10^{-2} M) HNO_3 + (3 X 10^{-3} M) L, (iii) (1 X 10^{-2} M) HNO_3 + (2 X 10^{-3} M) L and (iv) (0.5 X 10^{-2} M) HNO_3 + (1 X 10^{-3} M) L. The total volume was kept at 50 ml in each case and the temperature was adjusted at the desired temperature. In order to determine the stability constants of the BPDT metal complexes, the following mixtures were prepared and titrated against standard CO_2-free potassium hydroxide (0.094 M) solution. For the mole ratio (1:1) ligand-metal (L-M*). (a) (1 X 10^{-2} M) HNO_3, (b) (1 X 10^{-2} M) HNO_3 + (2 X 10^{-3} M) L and (c) (1 X 10^{-2} M) HNO_3 + (2 X 10^{-3} M) L + (2 X 10^{-3} M) M*. For the mole ratio (2:1), ligand-metal. (d) (2 X 10^{-2} M) HNO_3, (e) (2 X 10^{-2} M) HNO_3 + (4 X 10^{-3} M) L, (f) (2 X 10^{-2} M) HNO_3 + (4X 10^{-3} M) L + (2 X 10^{-3} M) M*. The total volume was adjusted to 50 ml by adding double-distilled water in each case. The titration curve obtained from (a) or (d) is a calibration curve for the electrode system; it provides data used to calculate the standard electrode potential, E_o, and the dissociation constant for water. These values were used to calculate the hydrogen ion concentration from potential readings [17].

3. RESULTS AND DISCUSSION

3.1 PROTON – LIGAND (BPDT) EQUILIBRIA.

BPDT is titrated mainly as triprotic acid (H_3L) and offered the buffer regions, pH (2.7-5.6) and pH (8.1-10.2) obviously due to the deportation of the two imino-groups and the amino–group. The protonation constants are reported in TABLE 1, where the highest values were found to be at 20°C indicating that the protonation reactions are favorable at low temperatures. FIGURE 1 shows a representative plot for the titration curves of BPDT at 25°C and by using different concentrations. The obtained values for these constants of BPDT are in consistence with that reported by Lomozik [18], as shown in TABLE 2, for diethylenetriamine using the SUPERQUAD program for the calculations and under similar experimental conditions as that stated in the experimental part in the present work. It is worth mentioning that diethylenetriamine is used as a starting material in the preparation of the ligand used in the present work by condensation with pyrrole-2-aldehyde.

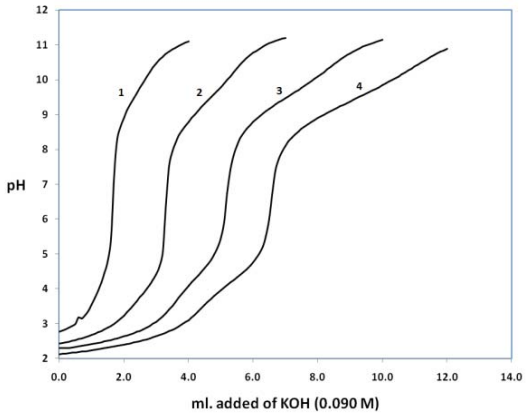

FIG. 1. Potentiometric Titration Curves of H^+/BPDT System at 25°C: (1) BPDT (0.005M), (2) BPDT (0.01M), (3) BPDT (0.015M), (4) BPDT(0.02M)

TABLE 1 Protonation constants (log β's) of BPDT.

	H:L	*20°C*	*25°C*	*30°C*	*40°C*
The mean values of log β's	HL	10.257(0.021)	9.751(0.027)	9.719(0.021)	9.668(0.011)
	H_2L	19.535(0.026)	18.610(0.030)	18.490(0.029)	18.364(0.015)
	H_3L	24.369(0.023)	22.947(0.042)	22.665(0.037)	22.459(0.018)
	H_4L	26.963(0.038)			
	H_5L	30.353(0.022)			

*(Standard deviations are given in parentheses)

TABLE 2: *The protonation constants of diethylenetriamine.*

	log β
HL	9.94
H_2L	19.04
H_3L	23.34

The equilibrium reactions for protonation constants are proposed by the following equation (charges are omitted for simplicity):

$$L + nH = H_nL, \qquad \beta_n = (H_nL) / (L)(H)^n \qquad (1)$$

Differences between the various log β values give the stepwise protonation constants K_n^H defined by equations (2 - 4)

$$H^+ + L^{2-} \rightleftharpoons HL^{-1} \quad K_1^H = (HL^{-1})/(H^+)(L^{2-}) \qquad (2)$$

$$H^+ + HL^{-1} \rightleftharpoons H_2L \quad K_2^H = (H_2L)/(H^+)(HL^{-1}) \qquad (3)$$

$$H^+ + H_2L \rightleftharpoons H_3L^+ \quad K_3^H = (H_3L^+)/(H^+)(H_2L) \qquad (4)$$

The concentration distribution of various species formed in solution (formation %) as a function of pH was obtained by the use of the SUPERQUAD 91 program throughout the present work. The distribution diagram for the system H^+/L^{3-} based on fitted equilibrium constants is depicted in FIGUREs 2-5. For the distribution diagrams at 25, 30 and 40ºC, the predominant species at lower pH values are H_3L and H_2L^-, the concentration of H_2L^- increases rapidly, attains a maximum value (≈ 100%) at pH ≈ 6.9 and decreases beyond this pH. At pH ≈ 6.9 the species HL^{2-} starts and then increases with increasing of the pH reaches a maximum (≈ 60%) at pH ≈ 9.3 and then decreases with the increasing of L^{3-} species which started at pH ≈ 6.9. For the distribution diagram at 20ºC, the predominant species at lower pH values are H_2L^{3-}, H_3L^{2-}, H_4L^- and H_5L. The concentration of H_3L^{2-} increases reached a maximum (≈ 88.5%) at pH ≈ 3.93 and decreases beyond this pH with the appearance of the H_2L^{3-} species. The concentration of H_2L^{3-} increases slowly with the increasing of pH till pH ≈ 3.9 then it increases rapidly and attains a maximum (≈ 99%) at pH ≈ 7.01 and then it decreases gradually. The concentration of HL^{4-} which appears at pH ≈ 7.01 starts to increase gradually until pH ≈ 9.80 it reaches its maximum value (≈57%), after which it starts to decrease. The species L^{5-} starts at pH ≈ 8.89 and then it gradually increases with the increasing of the pH value.

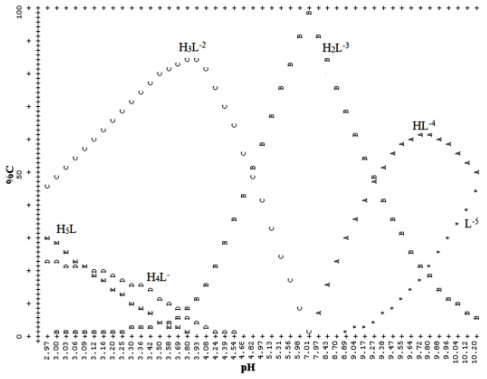

FIG. 2. Distribution diagram for the system H^+-L^{-5} at 20ºC.

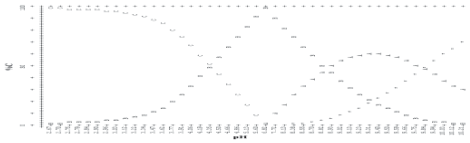

FIG. 3. Distribution diagram for the system H^+-L^{-3} at 25ºC.

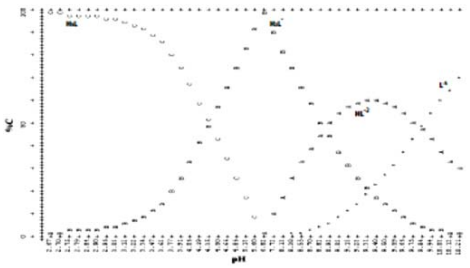

FIG. 4. Distribution diagram for the system H+-L-3 at 30ºC

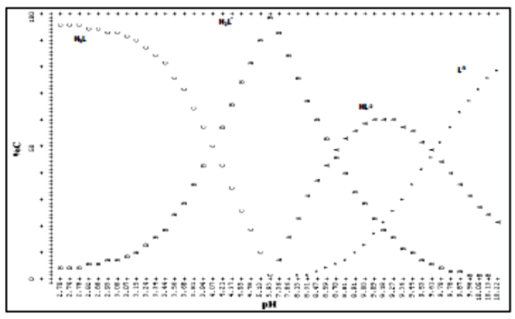

FIG. 5. Distribution diagram for the system H+-L-3 at 40ºC

3.2 STABILITY CONSTANTS OF THE COMPLEXES.

The stoichiometries and stability constants of M – BPDT complexes, using the molar ratios 1:1 and 2:1, (L:M), at the four different temperatures 20, 25, 30, and 40ºC and under the conditions described in the experimental part are reported in TABLE 3. A number of models were examined in sequence using the SUPERQUAD program and the reported stability constants are for the best models examined. A displacement was noticed in each curve of the titration curves for M– ligand mixtures, FIGUREs 6-8, compared with that for the free ligand. This indicates the release of protons, which in turn depends on the reaction between the ligand and M ion.

TABLE 3: *The stoichiometries and stability constants (log β'$_s$) for the metal complexes.*

Stoichiometry (L:M:H)	***Stability Constants (logβ'$_s$)***			
	20 ºC	***25 ºC***	***30 ºC***	***40 ºC***
Copper(II) complexes				
1:1:1	19.202 (0.85)	18.842(0.080)	18.136(0.046)	18.120(0.045)
1:1:0	15.714(0.022)	15.763(0.015)	15.455(0.005)	15.448(0.007)
1:1:-1	6.574(0.141)	6.967(0.040)	6.663(0.016)	6.780(0.016)
2:1:3	42.282(0.072)	41.234(0.053)	40.677(0.064)	40.645(0.072)
2:1:1	29.971(0.038)	29.440(0.037)	28.559(0.056)	28.386(0.041)
2:1:0	20.919(0.069)	21.011(0.036)	20.458(0.047)	20.245(0.033)
2:1:-1	11.650(0.107)	11.849(0.081)	11.273(0.130)	10.702(0.096)
Nickel(II) complexes				
1:1:1	15.022(0.114)	14.935(0.094)	15.405(0.082)	15.291(0.099)
1:1:0	8.778(0.018)	8.906(0.034)	9.221(0.061)	9.574(0.076)
1:1:-2	-5.351(0.032)	-4.622(0.049)	-3.979(0.056)	-3.269(0.086)
2:1:3	38.319(0.042)	36.692(0.041)	36.892(0.031)	35.899(0.056)
2:1:1	24.624(0.053)	23.905(0.047)	24.485(0.028)	23.799(0.044)
2:1:0	16.579(0.156)	------	------	------
2:1:-2	------	1.888(0.099)	2.796(0.073)	3.463(0.024)
Cobalt(II) complexes				
1:1:3	----------	------	25.474(0.069)	------
1:1:2	21.806(0.065)	20.814(0.037)	20.638 (0.119)	------
1:1:0	8.376(0.021)	8.290(0.010)	8.122(0.022)	7.864(0.14)
1:1:-1	-1.775(0.047)	-1.376(0.033)	-1.372(0.146	-0.823(0.162)
2:1:4	------	------	41.871(0.160)	43.810(0.120)
2:1:2	29.412(0.170)	28.454(0.094)	29.242(0.142)	30.717(0.106
2:1:1	22.910(0.016)	22.317(0.014)	21.985(0.106)	23.098(0.092)
2:1:0	14.724(0.023)	14.531(0.020)	14. 233(0.067)	15.191(0.098)

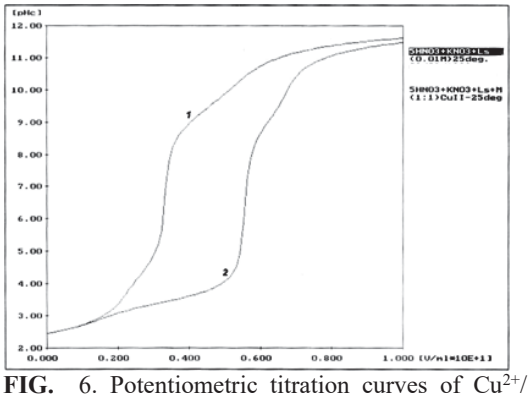

FIG. 6. Potentiometric titration curves of Cu^{2+}/ BPDT system at 25ºC: (1) BPDT, (2) Cu^{2+}/ BPDT complex

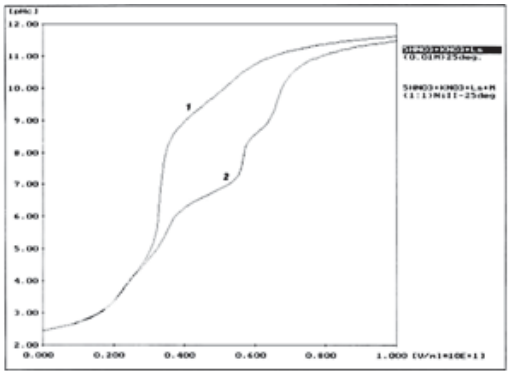

FIG. 7. Potentiometric titration curves of Ni^{2+}/BPDT system at 25ºC: (1) BPDT, (2) Ni^{2+}/BPDT complex

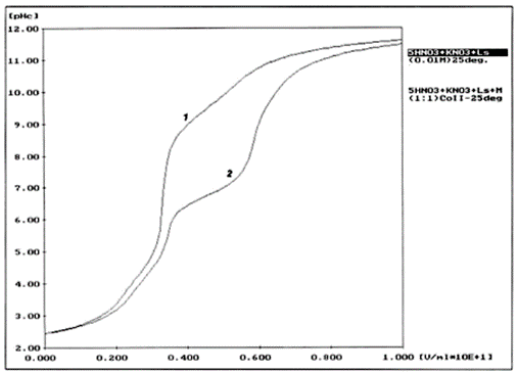

FIG. 8. Potentiometric titration curves of Co^{2+}/BPDT system at 25ºC: (1) BPDT, (2) Co^{2+}/BPDT complex

The concentration distribution of various complex species formed in solution (formation %) as a function of pH was obtained by means of the SUPERQUAD 91 program. The distribution diagrams for the systems M / BPDT and M / 2BPDT based on fitted stability constants at the four different temperatures are depicted in FIGUREs 9- 14.

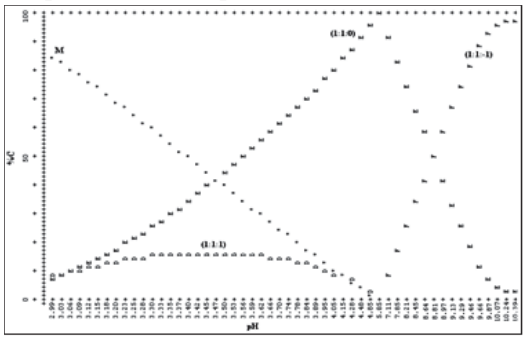

FIG. 9. Distribution diagram for the system Cu^{2+}/BPDT at 25ºC

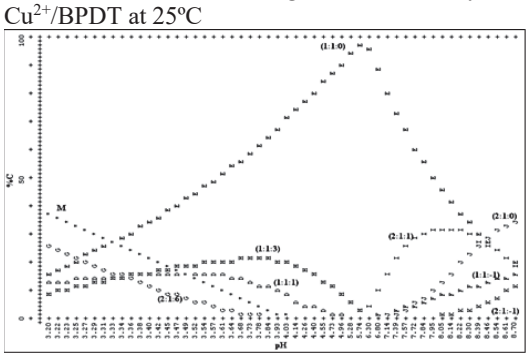

FIG. 10. Distribution diagram for the system Cu^{2+}/2BPDT at 25ºC

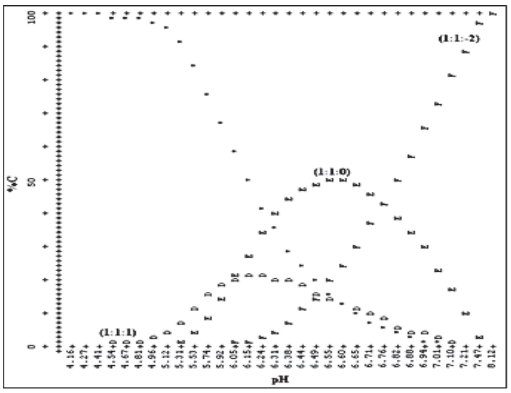

FIG. 11. Distribution diagram for the system Ni^{2+}/BPDT at 25ºC

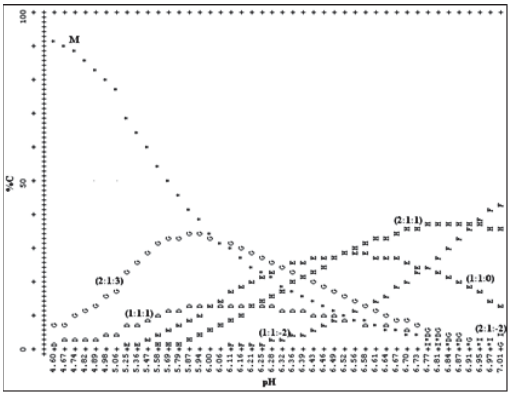

FIG. 12. Distribution diagram for the system Ni^{2+}/2BPDT at 25ºC

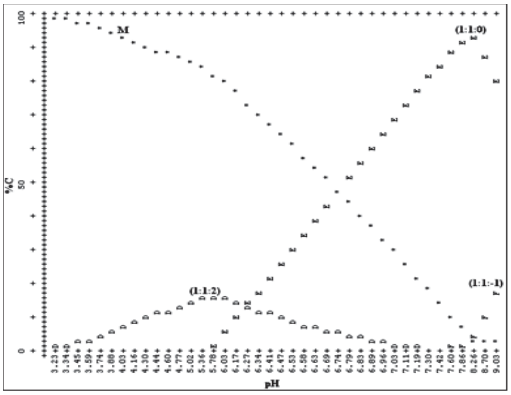

FIG. 13. Distribution diagram for the system Co^{2+}/BPDT at 25ºC

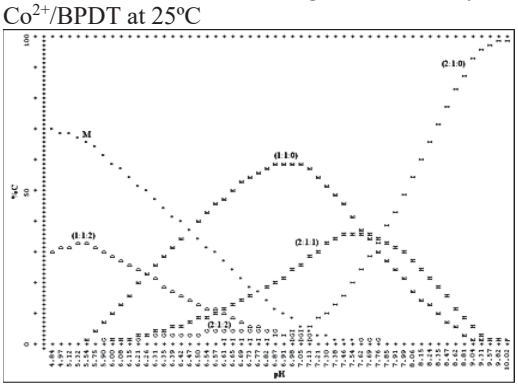

FIG. 14. Distribution diagram for the system Co^{2+}/2BPDT at 25ºC

3.3 ENTHALPIES AND ENTROPIES OF PROTONATION OF BPDT

From Arrhenius plots of $logK_1$, $logK_2$, and $logK_3$, TABLE 4, (K represents the protonation constant) vs. 1/T (°K), FIGURE 15, the stepwise enthalpy changes $\Delta H'_S$ were deduced, and these are given in TABLE 4. The free energy changes $\Delta G'_S$ were also evaluated at 25°C using the expression,

$$-\Delta G = 2.303RT \log K \quad (1)$$

Similarly, the entropy changes $\Delta S'_S$ were evaluated using the following relationships,

$$\Delta S = (\Delta H - \Delta G)/ T \quad (2)$$

$$-RT \ln K = \Delta H - T\Delta S \quad (3)$$

TABLE 4

	Temperature(°C)			
	20	*25*	*30*	*40*
$logK_1$	10.257	9.751	9.719	9.668
$logK_2$	9.278	8.859	8.771	8.696
$logK_3$	4.834	4.337	4.175	4.095

	ΔH (kcal/mole)	ΔG (kcal/mole)	ΔS(g) (cal/mole)	ΔS(C) (cal/mole)
$logK_1$	-10.61	-14.08	11.19	11.65
$logK_2$	-10.99	-12.73	5.40	5.87
$logK_3$	-14.24	-6.64	-26.09	-25.52

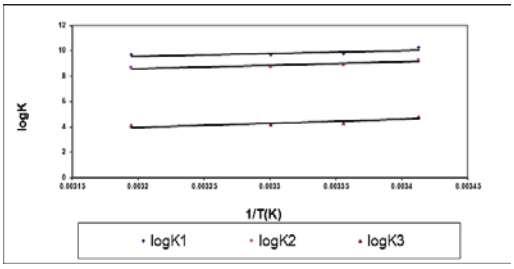

FIG. 15. Relationship between logk and 1/T

The stepwise entropy changes for BPDT were evaluated from equation (2), ΔS(C) and from the slope of TlogK vs. T plots, ΔS(g), FIGURE 16. The values of ΔS calculated by the two methods are in good agreement, TABLE 4.

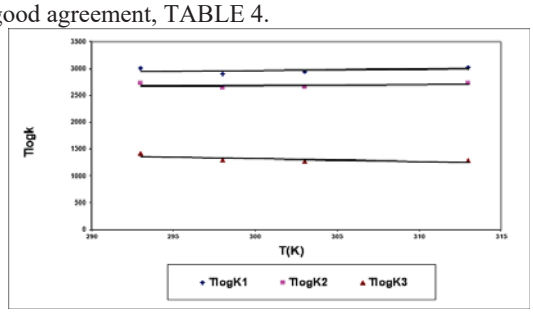

FIG. 16. Relationship between TlogK and T

The negative values of $\Delta H'_S$ indicate that the protonation reactions of BPDT are exothermic, i.e., the reaction is enhanced with decreasing temperature. It is evident from TABLE (4) that the heat required for the first and the second protonation reactions are very similar and they are less than that required for the third one. The large negative values of ΔG for the first and the second protonation reactions also indicate that these reactions proceed more spontaneously than the third one as supported by the values of $\Delta S'_S$. This latter value is positive for the first two reactions and it has a negative value for the third one.

3.4 ENTHALPIES AND ENTROPIES OF CHELATION OF BPDT WITH METAL CATIONS

The stepwise thermodynamic functions ΔG, ΔH, and ΔS for the M / BPDT complexes were calculated from the stepwise stability constants obtained at the four different temperatures used, TABLE 5. The values of these thermodynamic functions of the complexes are summarized in TABLE 5.

TABLE 5: *The stepwise stability constants (logK's) and the values of the thermodynamic functions ΔH, ΔG and ΔS of the complexes of Cu(II), Ni(II) and Co(II)*

	Cu(II)				Ni(II)				Co(II)			
	20°C	*25°C*	*30°C*	*40°C*	*20°C*	*25°C*	*30°C*	*40°C*	*20°C*	*25°C*	*30°C*	*40°C*
logKML	15.714	15.763	15.455	15.448	8.778	8.906	9.221	9.574	8.376	8.291	8.122	7.964
logKMHL	3.488	3.079	2.681	2.672	6.244	6.029	6.184	5.717	---	---	7.714	7.960
logKMH₂	---	---	---	---	---	---	---	---	13.43	12.523	12.514	------
logKML₂	20.918	21.01	20.458	20.245	---	---	---	---	14.724	14.531	14.233	15.191
logKMHL	9.052	8.43	8.101	8.141	---	---	---	---	8.186	7.786	7.752	7.907
logKMH₂	12.312	11.794	12.118	12.259	---	---	---	---	6.503	6.137	7.258	7.619
logKMH₃	---	---	---	---	13.695	12.787	12.407	12.100	---	---	---	---
	ΔH (kcal/mole	*ΔG (kcal/mol*	*ΔS(g) (cal/mole.*	*ΔS(C) (cal/moled*	*ΔH (kcal/mol*	*ΔG (kcal/mol*	*ΔS(g) (cal/mole.d*	*ΔS(C) (cal/mole.d)*	*ΔH (kcal/mol*	*ΔG (kcal/mol*	*ΔS(g) (cal/mole.d*	*ΔS(C) (cal/mole.d)*
logKML	-6.796	-21.636	49.438	49.798	17.473	-12.224	99.971	99.656	-8.980	-11.380	8.007	8.053
logKMHL	-16.931	-4.226	-41.247	-42.633	-9.999	-8.275	-5.733	-5.783	---	---	---	---
logKMH₂	---	---	---	---	---	---	---	---	-37.659	-17.189	-65.980	-68.690
logKML₂	-16.426	-28.838	40.617	41.651	---	---	---	---	10.057	-19.945	103.069	100.677
logKMHL	-17.872	-11.571	-18.800	-21.146	---	---	---	---	-4.390	-10.687	22.970	21.131
logKMH₂	1.980	-16.188	63.421	60.966	---	---	---	---	28.725	-8.424	127.330	124.661
logKMH₃	---	---	---	---	-31.522	-17.551	-44.086	-46.880	---	---	---	---

For the Cu(II) complexes the large negative values of ΔG obtained for the species [ML], [ML_2], and [MH_3L_2] indicate that the formation reaction of these species proceed spontaneously more than the other species even they have negative ΔG values, but lower than that of the former species. It is obvious from the concentration distribution curves that the species [ML] is the most stable species of the complexes formed in the case of both molar ratios used. This may be attributed to its large positive entropy value observed, more over its large negative ΔG value, and it is well known that the chelate effect is mainly an entropy effect [19].

For the Ni(II) complexes, the species [ML] is more stable than the species [MHL] in the systems of the mole ratio (1:1), and from the concentration distribution curves, it is observed that this species, [ML], is present in the systems of the mole ratio (2:1) with a relatively high concentration. This can be attributed to its high positive value of ΔS. Also, as it has a positive ΔH value, its concentration increases as the temperatures rise.

In the case of Co(II) complexes, the large negative value of ΔG of the species [ML_2] indicates that its formation reaction proceeds spontaneously, and it is the more stable species, although it has a positive enthalpy change, but it was outweighed by the large positive ΔS value which is favorable to chelation. The species [MH_2L], [ML] and [MHL_2], come after the species [ML_2] in the stability according their ΔG values.

4. CONCLUSION

From the obtained results, it can be concluded that the order of stability of the complexes formed between BPDT and transition ions, Cu^{2+}, Ni^{2+} and Co^{2+} investigated in this study is in the expected Irving - Williams order [20]: $Cu^{2+} > Ni^{2+} > Co^{2+}$.

5. REFERENCES

[1] Soroceanu, A., Bargan, A. Advanced and Biomedical Applications of Schiff-Base Ligands and Their Metal Complexes: A Review. *Crystals* 2022, 12, 1436.

[2] Betti, N., Al-Amiery, A.A., Al-Azzawi, W.K. et al. Corrosion inhibition properties of Schiff base derivative against mild steel in HCl environment complemented with DFT investigations. *Sci Rep* 13, 8979, 2023. https://doi.org/10.1038/s41598-023-36064-w

[3] Kuchtanin, V., Kleščíková, L., Šoral, M., Fischer, R., Růžičková, Z., Rakovský, E., Moncoľ, J., Segľa, P., Nickel(II) Schiff base complexes: Synthesis, characterization and catalytic activity in Kumada–Corriu cross-coupling reactions, *Polyhedron*, 117, 2016, 90-96, ISSN 0277-5387, https://doi.org/10.1016/j.poly.2016.05.037.

[4] Puccetti, L., Fasoils, G., Vullo, D., Chohan, Z. H.; Scozzafava, A., Supuran, C. T. Carbonic anhydrase inhibitors. Inhibition of cytosolic/tumor-associated carbonic anhydrase isozymes I, II, IX, and XII with Schiff's bases incorporating chromone and aromatic sulfonamide moieties, and their zinc complexes, *Bioorg. Med. Chem. Lett*. 2005, 15, 3096-3101.

[5] Brown, L.S., Gat, Y., Sheves, M.; Yamazaki, Y., Maeda, A., Needleman, R., Lanyi, J. K. The Retinal Schiff Base-Counterion Complex of Bacteriorhodopsin: Changed Geometry during the Photocycle Is a Cause of Proton Transfer to Aspartate 85, *Biochemistry*, 1994, 33, 12001-12011.

[6] Fishkin, N. E., Sparrow, J. R., Allikmets, R.; Nakanishi, K. Isolation and characterization of a retinal pigment epithelial cell fluorophore: An all-trans-retinal dimer conjugate, *Proc. Natl. Acad. Sci. USA,* 2005, 102, 7091-7096.

[7] Bieschke, J.; Zhang, Q.; Powers, E. T.; Lerner, R. A.; Kelly, J. W. Oxidative Metabolites Accelerate Alzheimer's Amyloidogenesis by a Two-Step Mechanism, Eliminating the Requirement for Nucleation, *Biochemistry*, 2005, 44, 4977-4983.

[8] Mure, M., Brown, D. E., Saysell, C., Rogers, M. S., Wilmot, C. M., Kurtis, C. R.; McPherson. M. J., Phillips, S. E. V., Knowles, P. F., Dooley, D. M. Role of the Interactions between the Active Site Base and the Substrate Schiff Base in Amine Oxidase Catalysis. Evidence from Structural and Spectroscopic Studies of the 2-Hydrazinopyridine Adduct of Escherichia coli Amine Oxidase, *Biochemistry,* 2005, 44, 1568-1582.

[9] Toyota, E., Sekizaki, H., Takahashi, Y., Itoh, K., Tanizawa, K. Amidino-Containing Schiff Base Copper(II) and Iron(III) Chelates as a Thrombin Inhibitor, *Chem. Pharm. Bull.* 2005, 53, 22-26.

[10] Ahmed, Z., Ravandi, A., Maguire, G. F., Kuksis, A., Connelly, P. W., Formation of apolipoprotein AI–phosphatidylcholine core aldehyde Schiff base adducts promotes uptake by THP-1 macrophages, *Cardiovasc. Res.* 2003, 58, 712-720.

[11] Ul-Hassan, M., Scozzafava, A., Chohan, Z. H., Supuran, C. T. Carbonic Anhydrase Inhibitors: Metal Complexes of a Sulfanilamide Derived Schiff base and their Interaction with Isozymes I, II and IV, *J Enzyme Inhib.* 2001, 16, 499-505.

[12] Tyagi, P., Chandra, S., Saraswat, B.S., Sharma, D., Design, spectral characterization, DFT and biological studies of transition metal complexes of Schiff base derived from 2-aminobenzamide, pyrrole and furan aldehyde, *Spectrochimica Acta Part A: Molecular and Biomolecular Spectroscopy*, 43, 2015, 1-11, https://doi.org/10.1016/j.saa. 2015, 02.027

[13] Bacchi A., Carcelli M., Gabba L., Ianelli S., Pelagatti P., Pelizzi G., Rogolino D., Syntheses, characterization and X-ray structure of palladium(II) and nickel(II) complexes of tetradentate pyrrole containing ligands, *Inorganica Chimica Acta* 342, 2003, 229-235. https://doi.org/10.1016/S0020-1693(02)01077-0

[14] Welcher, F. J. *"The Analytical Uses of EDTA"*, Van. Nostrand, New York, 1957.

[15] Kwiatkowski E., Kwiatkowski M., Olechnowicz A., Bandoli G., Coordination of Schiff-bases derived from pyrrole-2-carboxaldehyde and triamines to copper(II) And nickel(II) Ions - crystal-structures of $[Cu(C_{15}H_{20}N_5)]NO_3$ and $[NI(C_{15}H_{20}N_5)]ClO_4$, *Journal of Chemical Crystallography* Vol. 23, No. 6, 1993, 473-480. DOI10.1007/BF01182521

[16] Gans, P., Sabatini, A., Vacca, A. A. SUPERQUAD: An Improved General Program for Computation of Formation Constants from Potentiometric Data. *J. Chem. Soc. Dalton Trans.* 1985, 1195-1200.

[17] Anderegg, G., Kholief, K., Extrapolation of molar equilibrium constants to zero ionic strength and parameters dependent on it. Copper(II), nickel(II), hydrogen(I) complexes with glycinate ion and calcium(II), hydrogen(I) complexes with nitrilotriacetate ion, *Talanta*, 1995, 42, 1067-79.

[18] Lomozik, L., Bolewski, L., Bregier-Jarzebowska, R., Stability and structure of copper(II) complexes with polyamines and related ligands In aqueous solution, *Polish J. Chem.* 1995, 69, 197.

[19] Cotton, F. A., "Advanced Inorganic Chemistry", Wiley-Interscience, New York, 157, 1972.

[20] Irving, H., Williams, R. J. P. Order of Stability of Metal Complexes, *Nature*, 1948, 162, 746.

Jouf University Science and Engineering Journal (JUSEJ) 2023; 10(2): 85- 91
Published online: Dec. 2023 (https://www.ju.edu.sa/en/jouf-university-science-and-engineering-journal-jusej/home/)
Print ISSN: 1658-6670 ***Electronic ISSN:1658-9173 (1443/5074)***

Studies on the isotherm, kinetic, and thermos-sorption aspects of the Cr (VI) uptake onto commercial bentonite

Mubarak A. Eldoma [1*]

[1] Chemical Engineering Department, College of Engineering, Jazan University, Jazan, Saudi Arabia

***Corresponding author**

Mubarak A. Eldoma

Email address:

madam@jazanu.edu.sa

Submission Date: *Oct. 03, 2023*
Accepted Date: *Oct. 22, 2023*

The capacity of Khulais, Saudi Arabia bentonite (CB) to adsorb and remove Cr(III) from the aqueous system was investigated. The bunch adsorption process examined a number of parameters, including pH, starting attention, sorbent dosage, and interaction time. Bentonite was examined using SEM. Maximum uptake capability ever measured was 58 mg/g at pH 2 for 60 minutes. This process fits a second-order pseudo-model and a Redlich-Peterson isotherm, per kinetic and equilibrium analyses. The Van't Hoff equation was applied to assess the temperature-related variables, and the results showed that the process was an endothermic chemical process.

Keywords: *Adsorption; Isotherm; Kinetic; Thermodynamic; Bentonite*

1. INTRODUCTION

Excessive use of the heavy metal chromium is harmful to both the environment and human health. Chromium-containing wastewater must be treated before its discharge into the surroundings in order to lessen pollution and associated concerns [1, 2]. In addition to inhalation, drinking water exposure to high concentrations of Cr(VI) may cause a variety of health problems, including lung cancer, respiratory problems, and skin irritation[3, 4]. Chromium contamination of water bodies and contaminated sediment can affect aquatic ecosystems and animals. Additionally, it might affect crops and result in decreased harvests [5, 6]. The kind and amount of chromium in the effluent, the resources that are available, and the regulations that must be followed all influence the approach that is used [7]. There are numerous ways to remove chromium from wastewater, involving precipitation [8], ion exchange [9], sorption [10, 11], membrane techniques [12], biological treatment [13], and electrocoagulation [14]. The wastewater's unique properties, as well as environmental and governmental considerations, should be taken into account while selecting a procedure. In order to remove the proper amount of chromium and meet discharge limits, a mix of techniques may frequently be required. Before being released into the environment, the treated wastewater must also pass tests to confirm that it complies with legal criteria. The elimination of Cr(VI) from liquid feed was examined in this work using bentonite obtained from Khulais, Saudi Arabia. Using a batch method for the studies, variables e.g. interaction time, temperature, pH, beginning metal ion attentiveness, and sorbent dosage were used to study Cr(VI) uptake. Also, Thermodynamic, isothermal, and kinetic aspects were studied.

2. RESOURCES AND TECHNIQUES

2.1 BENTONITE PREPARATION

A planetary ball mill (model no. 56742 Germany) was used to grind the bentonite sample (Khulais, Saudi Arabia) after it had been heated in a vacuum oven for 48 hours at 150 C, cooled in a desiccator. Additionally, a sieve shaker (IRIS FTL-0400) was used to further process the bentonite material.

2.2 CR(VI) STOCK SOLUTION PREPARATION

To create a base solution containing 1000 mg/l Cr(VI), dissolve the specified amount of $K_2Cr_2O_7$ (Sigma-Aldrich Company) in a watery system and dilute to the desired concentration. The pH was altered by 0.1N of NaOH and HCl. All of the substances were AR grade and originated from the German company Sigma-Aldrich.

2.3 BATCH EXPERIMENT

Batch studies were used to optimize a number of adsorption limitations, including contact time, temperature, pH, sorbent dose, and principal metal focus. 100 ml of Cr(VI) preparations with starting attentiveness (120 - 840 mg/L) with pH ranges (1.5-8) should be added to Erlenmeyer flasks with the necessary quantity of bentonite. The solution was agitated at 150 rpm for varied periods of time at temperatures that varied (30-45°C) in a thermostat-shaken water bath. After sample separation and a four-minute, 5000 rpm centrifugation. The final Cr(VI) content was detected using a UV spectrophotometer (Perkin Elmer, A 800).

Adsorption capacity (q) was explained as follows:

$$q = \frac{C_i - C_e}{S} \times L \qquad (1)$$

Where

C_i = *initial attentiveness of Cr(VI) (mg/L)*
C_e = *attentiveness of Cr(VI) at steadiness (mg/L)*
L = *liquid sample of Cr(VI) (L)*
S = *sorbent dosage of (LC-AC) (g)*

The reduction % (Re) is calculated using the subsequent equation:

$$R_e\,(\%) = \frac{C_i - C_e}{C_i} \times 100 \qquad (2)$$

3. RESULTS AND ANALYSIS

3.1 ASPECTS OF BENTONITE

Figure 1(a) displays a SEM picture of bentonite prior to adsorption. It looks like the surface is porous, rough, and randomly formed. These traits suggest that the surface has a large surface area and multiple fissures, which may allow for efficient adsorption between Cr(VI) and bentonite. The ions have numerous opportunities to interact with the bentonite through roughness and porosity, potentially leading to effective adsorption. Based on the bentonite's loss of porosity and increased surface roughness (Fig. 1(b)), the adsorption process may have led to certain changes in the bentonite. It's possible that the Cr(VI) ions connected to the surface, blocking the pores and filling in the flaws. The presence of this modification may indicate that the target molecules were successfully adsorbed onto

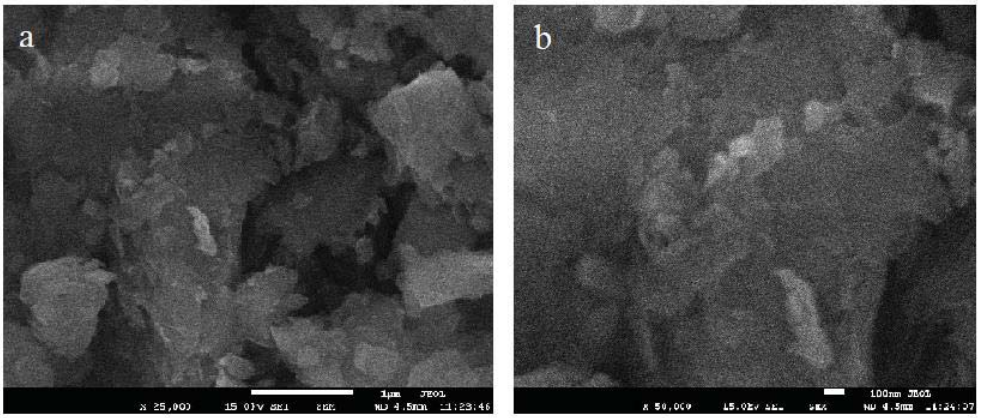

Fig. 1 Raw, unprocessed bentonite in a SEM picture before (a), and after adsorption (b).

3.2 ADSORPTION INVESTIGATIONS.

3.2.1 RESULT OF PH:

By adjusting the pH between 1.5 and 8 at 30°C, 635.5 mg/l, 0.2 g of bentonite, 150 rpm of stirring, and 60 minutes, the contribution of pH was investigated (**Fig. 2**). At pH values between 1.5 and 2, the effectiveness of ions' removal increased. As the pH increased inside this limit, more Cr(VI) ions were shown to be attracted to the bentonite, according to this data. The optimal capacity was reached at pH 2. This indicates that at this particular pH, bentonite has the highest affinity for ions. The efficiency of Cr(VI) removal decreased at lower pH values (lower 2). This can be due to rivalry among H^+ ions and Cr(VI) ions for spots of adsorption on the bentonite. This rivalry reduced the number of Cr(VI) ions that could be eliminated from the solution [7, 15]. Above a pH of 2, the ability to remove metal was lowered. This reduction in efficacy is brought about by the breakdown of matter, a chemical event in which water molecules are destroyed as a result of an increase in hydroxide ions (-OH) when the pH increases [11,16].

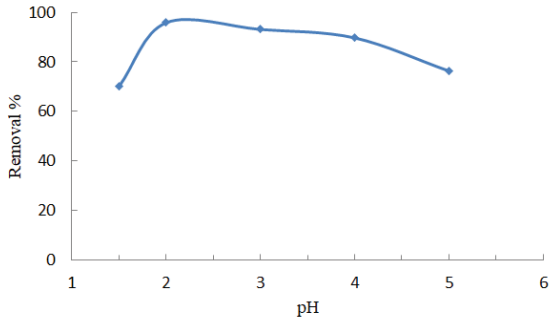

Fig. 2. pH's impact on Cr (VI) ion binding to bentonite

3.2.2 INTERACTION TIME'S IMPACT:

The length of period it takes for the bentonite to absorb the most Cr(VI) adsorptive depends in large part on the contact time. The greater the contact time, the more times the uptake operation must occur. Under the specified conditions of temperature 30°C, pH 2, and bentonite dose (0.2g), equilibrium is reached after 60 minutes. Cr(VI) ion uptake increases as the contact period lengthens (**Fig. 3**). It's crucial to give a system enough time to attain equilibrium in a variety of chemical and physical processes [17]. When the rates of forward and backward processes are equal and there is no net change in the system's attributes over time (equilibrium). For precise measurements and a thorough understanding of the behavior of the system being studied, equilibrium must be attained. Reaching equilibrium is essential for accurate investigations, and kinetic representations like pseudo-first-order, pseudo-second-order, Elovich, and intraparticle distribution are valuable nonlinear tools for understanding and characterizing adsorption processes in various applications, such as environmental remediation, wastewater treatment, and material science.

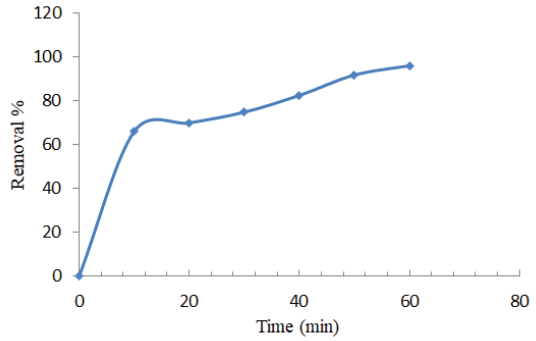

Fig. 3. Effectiveness of interaction time

The pseudo-first-order model [18]:

$$\log(q_e - q_t) = \log q_e - \frac{k_1}{2.303}t \qquad (3)$$

The Pseudo-second-order model [15]:

$$\frac{t}{q_t} = \frac{1}{k_2 q_e^2} + \frac{1}{q_e}t \qquad (4)$$

The Elovich model [19]:

$$q_t = \frac{1}{\beta}\ln(\alpha\beta) + \frac{1}{\beta}\ln(t) \qquad (5)$$

The intraparticle diffusion model [19]:

$$\log R_e = \log K_{id} + a\log(t) \qquad (6)$$

K_1 and K_2 are the kinetic factors wherever q_e and q_t are the adhesive capabilities in mg/g at stabilization and t, respectively. The Elovich factors are β & α. The Intraparticle constant is called K_{id}. By calculating a correlation factor (R^2) and chi-square analysis ($\chi 2$) the outcomes of the study were tested for rate-dependent suitability [17].

According to **Table 1** and **Fig. 4**, the greater R^2 and lowest χ^2 readily demonstrated that the Cr(V1) adsorption rates closely match the pseudo-second-order model. As a result, it became apparent that chemical-adsorption is essential for bentonite to take in Cr(V1) [20].

Table 1: *Kinetic limits values.*

Experimental q_e	Kinetic models	Values
	Pseudo-first-order	
	q_e (mg/g)	**56.552**
	K_1 (L/min)	**0.11161**
	R^2	**0.9954**
	$\chi 2$	**1.7633**
58	**Pseudo-second-order**	
	q_e (mg/g)	**62.82908**
	K_2 (g/mg.min)	**0.00277**
	R^2	**0.9997**
	$\chi 2$	**0.11418**
	Elovich	
	α (mg/g.min)	**1.15128**
	β (g/mg)	**8.96528**
	R^2	**0.96376**
	$\chi 2$	**2.39176**
	Intraparticle	
	K_P	**8.09107**
	R^2	**0.74517**
	$\chi 2$	**97.7017**

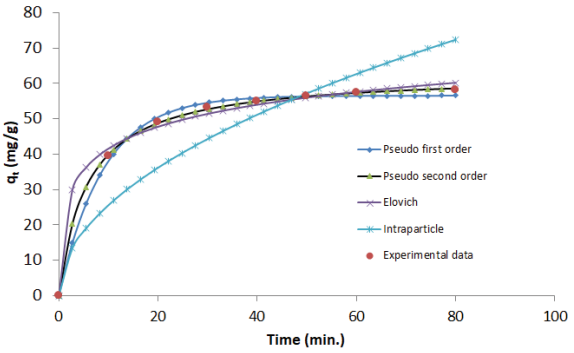

Fig. 4. Kinetic models for the adsorption process.

3.2.3 INITIAL CR(VI) CONCENTRATIONS' RESULTS:

The results showed that at 30°C, 0.2 g bentonite dosage, 60 min, and pH 2, the bonding capabilities increased from 11.58 to 58 mg/g as the preliminary attentiveness upsurge began from 120 to 840 mg/L **(Fig.5)** . This shows that even though the initial concentration was higher, more Cr(VI) ions were able to be trapped by the bentonite. Further evidence that the adsorbent was less successful at removing Cr(VI) from the solution at greater initial concentrations was provided by the fact that the removal efficacy fell as the starting Cr(VI) content increased, and the open adsorption sites on the bentonite became saturated [13]. This demonstrates that as more Cr(VI) ions are introduced to the solution, the accessible sites on the bentonite are filled up, and eventually no more adsorption can occur due to the adsorbent's finite capacity [12].

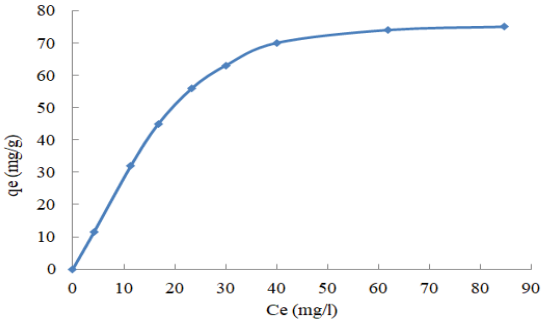

Fig. 5. Role of beginning Cr(VI) ratios

The equilibrium uptake of Cr(VI) on bentonite was explained by different isotherm models and the isotherm parameters were determined via nonlinear systems [21]. These data are needed to design and enhance adsorption techniques for use in water treatment, pollution control, and other environmental applications.

LANGMUIR MODEL

The following equations [22] describe this isotherm:

$$q_e = (Q_L K_L C_e) /(1 + K_L C_e \quad (7)$$

Where C_e is the equilibrium Cr(VI) concentration (mg/L). The Langmuir isotherm has two constants: Q_L (mg/g) and K_L (L/mg).

FREUNDLICH MODEL

This isotherm [23] uses the following equation:

$$q_e = K_F C_e^{1/n} \quad (8)$$

The Freundlich constant is K_F (mg/g), and n is a measure of how strongly Cr(VI) adsorbs on bentonite.

REDLICH-PETERSON MODEL

This isotherm [17] uses the following equation:

$$q_e = K_{RP} Ce/(1+ AC_e{}^{\beta}) \quad (9)$$

K_{RP} and A are constants. The advocate for the binding energy is represented by the item β.

JOVANOVIC MODEL

This isotherm is represented by the eq. [24] below:

$$q_e = q_{max} (1- e^{KJ\ Ce}) \quad (10)$$

Where K_J and q_{max} are constant.

The Redlich-Peterson isotherm most accurately represents the experimental data, as seen in **Tables 2** and **Fig. 6**. In this instance, the adhesion process's coefficient of determination (R^2) reached its greatest value (0.999). The smallest result (0.992) was obtained for $\chi 2$, on the other hand, demonstrating that the model is well-fitted. The R-P isotherm model displayed parameter β values close to 1.0, proving that the Langmuir isotherm is equally effective as the R-P isotherm at simulating experimental data. Therefore, it may be said that the surfaces of the analyzed bentonite formed a monolayer of Cr(VI) (monolayer adsorption principle)*[23]*.

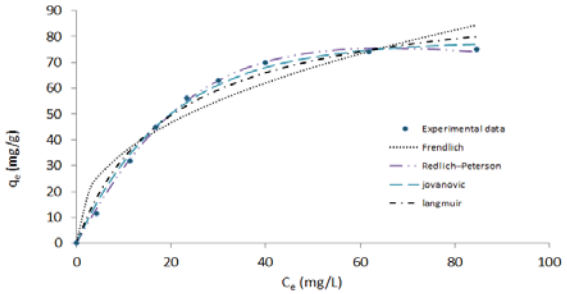

Fig. 6 Isotherms of *Cr(VI)* adsorption of process

Table 2. *The adsorption isotherm's constants.*

Isotherms	Values
Langmuir	
Q_L (mg/g)	**98.70**
K_L (L/mg)	**0.05014**
R^2	**0.979**
$\chi 2$	**15.83098**
Freundlich	
K_F ($mg^{(1-1/n)}L^{1/n}g^{-1}$)	**13.603**
n	**2.429**
R^2	**0.915**
$\chi 2$	**64.80987**
Redlich-Peterson	
K_P(L/g)	**3.19604**
A(L./mg)$^{\beta}$	**0.00256**
β	**1.564**
R^2	**0.999**
$\chi 2$	**0.992**
Jovanovic	
K_J (L/mg)	**0.05142**
q_{max}	**77.99**
R^2	**0.994**
$\chi 2$	**4.789**

3.2.4 THE IMPACT OF ADSORBENT DOSAGE:

The experiment employed several doses of bentonite (0.2-1.0g) at pH 2 and 30°C for 60 minutes. The elimination aptitude of Cr(VI) improved as the adsorbent dose increased beginning 0.2g to 1.0g **(Fig. 7)**. The presence of more energetic places on the bentonite may be the result of an increase in adsorbent doses' improved removal efficiency. There are more active sites for the Cr(VI) ions to bind to and be pulled out of the solution when there is more bentonite present. This is most likely a result of the surface area increase with larger bentonite dosages [16, 25].

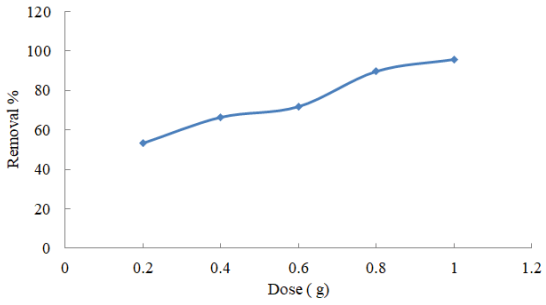

Fig. 7. Efficacy of the bentonite dosage on the Re % of Cr(VI).

3.4 STUDIES OF THERMODYNAMICS

Among 30 and 60°C, the temperature influence on Cr(VI) uptake was studied. It became clear that removing Cr(VI) ions was less efficient as the temperature increased. Estimates were made for enthalpy (ΔH°), entropy (ΔS°), and Gibbs free energy (ΔG°) using the diffusion coefficient (K_D) by the following equations [22, 26].

$$\mathrm{Ln}K_D = \frac{\Delta S^\circ}{R} - \frac{\Delta H^\circ}{RT} \quad (11)$$

$$K_D = \frac{q}{Ce} \quad (12)$$

$$\Delta G^\circ = \Delta H^\circ - T\,\Delta S^\circ \quad (13)$$

The minus sign of ΔG makes it abundantly evident that the sorption reaction is spontaneous. At various temperatures **(Table 3)**. Additionally, a decline in the negative value of ΔG° with temperature increases shows that the sorption process was more advantageous at higher temperatures. The results showed that the values of ΔH° and ΔS° were respectively 54.606 kJ mol^{-1} and 0.1802 kJ mol^{-1} K^{-1} **(Fig. 8)**. Adsorption is endothermic, as indicated by the +ve ΔH°. The growing unpredictability throughout the uptake phase is indicated by the +ve ΔS° [27, 28].

Table 3: Temperature-dependent variables.

Temperature K	ΔG° kJ mol^{-1}	ΔH° kJ mol^{-1}	ΔS° kJ $K^{-1}mol^{-1}$
303	-0.0215	54.606	**0.1802**
308	-0.8956		
313	-1.7966		
318	-2.9676		

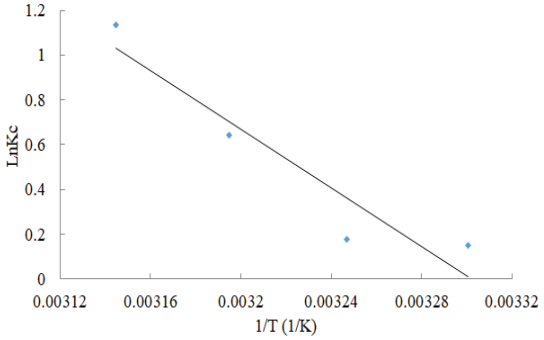

Fig. 8. The Van't Hoff scheme.

4. CONCLUSIONS

The analysis of bentonite showed that it has an attractive possibility for removing Cr(VI) from water-based solutions. The highest ability to adsorb (q_e) ever measured being 58 mg/g at pH 2, and 60 min. The findings of the kinetic and equilibrium calculations show that the binding process matches the Redlich-Peterson isotherm and the pseudo-second-order. Additionally, according to thermodynamic research, the uptake process is endothermic and immediate chemical adsorption.

5. REFERENCES

[1] C.-C. Wang, X.-D. Du, J. Li, X.-X. Guo, P. Wang, J. Zhang, Photocatalytic Cr(VI) reduction in metal-organic frameworks: a mini-review, Appl. Catal. B: Environ. 193 (2016) 198–216.

[2] Z. Shi, Z. Chen, Y. Zhang, X. Wang, T. Lu, Q. Wang, Z. Zhan, P. Zhang, COF TzDa/Ag/AgBr Z-scheme heterojunction photocatalyst for efficient visible light driven elimination of antibiotics tetracycline and heavy metal ion Cr(VI), Sep. Purif. Technol. 288 (2022) 120717.

[3] S. Bao, W. Yang, Y. Wang, Y. Yu, Y. Sun, K. Li, PEI grafted amino-functionalized graphene oxide nanosheets for ultrafast and high selectivity removal of Cr(VI) from aqueous solutions by adsorption combined with reduction: behaviors and mechanisms, Chem. Eng. J. 399 (2020) 125762.

[4] C.C. Wang, X. Ren, P. Wang, C. Chang, The state of the art review on photocatalytic Cr(VI) reduction over MOFs-based photocatalysts: from batch experiment to continuous operation, Chemosphere 303 (2022) 134949.

[5] Y.H. Li, X.H. Yi, Y.X. Li, C.C. Wang, P. Wang, C. Zhao, W. Zheng, Robust Cr(VI) reduction over hydroxyl modified UiO-66 photocatalyst constructed from mixed ligands: Performances and mechanism insight with or without tartaric acid, Environ. Res. 201 (2021) 111596.

[6] X.-H. Yi, Y. Gao, C.-C. Wang, Y.-H. Li, H.-Y. Chu, P. Wang, Photocatalytic Cr(VI) reduction over MIL-88A(Fe) on polyurethane sponge: From batch to continuous-flow operation, Chin. Chem. Lett. 108029 (2022).

[7] L. Li, H. Gao, G. Liu, S. Wang, Z. Yi, X. Wu, H. Yang, Synthesis of carnation flower-like Bi2O2CO3 photocatalyst and its promising application for photoreduction of Cr(VI), Adv. Powder Technol. 33 (2022) 103481.

[8] K.J. Min, H.J. An, A.H. Lee, H.-G. Shin, K.Y. Park, Electrodialysis with a channeled stack for high strength cadmium removal from wastewater, Membr, Water Treat. 14 (2023) 47–54.

[9] F. Bahador, R. Foroutan, H. Esmaeili, B. Ramavandi, Enhancement of the chromium removal behavior of Moringa oleifera activated carbon by chitosan and iron oxide nanoparticles from water, Carbohydr. Polym. 251 (2021) 117085. [10] Q. Zhao, X.-H. Yi, C.-C. Wang, P. Wang, W. Zheng, Photocatalytic Cr(VI) reduction over MIL-101(Fe)–NH2 immobilized on alumina substrate: from batch test to continuous operation, Chem. Eng. J. 429 (2022) 132497.

[11] C. Kim, S.S. Lee, A. Ghosh, J. Lee, J.D. Fortner, Cetyltrimethylammonium bromide – oleic acid (CTAB-OA) bilayer coated iron oxide nanocrystals for enhanced chromium (VI) photoreduction via ligand-to-metal charge transfer mechanism, Chem. Eng. J. 431 (2022) 133938.

[12] S. Karthick, R. Palani, D. Sivakumar, N. Meyyappan, Biosorption of Cr(VI) ions by Ficus religiosa barks: batch and continuous study, Memb. Water Treat. 13 (2022) 209–217.

[13] P. Li, J.T. Damron, G.M. Veith, V.S. Bryantsev, S.M. Mahurin, I. Popovs, S. Jansone-Popova, Bifunctional ionic covalent organic networks for enhanced simultaneous removal of chromium(VI) and arsenic(V) oxoanions via synergetic ion exchange and redox process, Small 17 (2021) e2104703.

[14] Z.Q. Huang, W. Cai, Z. Zhang, Modification and acidification of polysulfone as effective strategies to enhance adsorptive ability of chromium(VI) and separation properties of ultrafiltration membrane, J. Appl. Polym. Sci. 139 (2022) 52127.

[15] C. Wang, G. Yang, W. Shi, K. Matras-Postolek, P. Yang, Construction of 2D/2D MoS2/g-C3N4 heterostructures for photoreduction of Cr(VI), Langmuir 37 (2021) 6337–6346.

[16] A. Raja, P. Rajasekaran, B. Vishnu, K. Selvakumar, J. Yeon Do, M. Swaminathan, M. Kang, Fabrication of effective visiblelight-driven ternary Z-scheme ZnO-Ag-BiVO4 heterostructured photocatalyst for hexavalent chromium reduction, Sep. Purif. Technol. 252 (2020) 117446.

[17] A. Shawky, N. Alahmadi, R.M. Mohamed, Z.I. Zaki, Bi2S3- sensitized TiO2 nanostructures prepared by solution process for highly efficient photoreduction of hexavalent chromium ions in water under visible light, Opt. Mater. 124 (2022) 111964.

[18] E. Zhou, N. Sun, Y. Jiang, Q. Wang, Y. Xiao, Y. Liu, W. Zhang, H. Xu, Z. Liu, Conductive polypyrrole encapsulating Cd0.5Zn0.5S to enhance hydrophilicity and charge separation towards robust photodegradation of tetracycline hydrochloride and photoreduction of Cr(VI), Appl. Surf. Sci. 580 (2022) 152286.

[19] N. Wang, L. Zhu, K. Deng, Y. She, Y. Yu, H. Tang, Visible light photocatalytic reduction of Cr(VI) on TiO2 in situ modified with small molecular weight organic acids, Appl. Catal. B: Environ. 95 (2010) 400–407.

[20] N. Alias, Z. Hussain, W.K. Tan, G. Kawamura, H. Muto, A. Matsuda, Z. Lockman, Nanoporous anodic Nb2O5 with porein-pore structure formation and its application for the photoreduction of Cr(VI), Chemosphere 283 (2021) 131231.

[21] B.A. Marinho, R.O. Cristo´va˜o, R. Djellabi, J.M. Loureiro, R.A. R. Boaventura, V.J.P. Vilar, Photocatalytic reduction of Cr(VI) over TiO2-coated cellulose acetate monolithic structures using solar light, Appl. Catal. B: Environ. 203 (2017) 18–30.

[22] M.-H. Li, Y.-M. Di, Y.-W. Wang, M.-H. You, M.-J. Lin, In-situ construction of novel

naphthalenediimide/metal-iodide hybrid heterostructures for enhanced photoreduction of Cr(VI), Dyes Pigm. 187 (2021) 109146.
[23] S. Luo, S. Li, S. Zhang, Z. Cheng, T.T. Nguyen, M. Guo, Visible-light-driven Z-scheme protonated g-C3N4/wood flour biochar/BiVO4 photocatalyst with biochar as charge-transfer channel for enhanced RhB degradation and Cr(VI) reduction, Sci. Total Environ. 806 (2022) 150662.
[24] S. Jana, S. Pramanik, B. Show, A. Mondal, S. Mukhopadhyay, A new strategy to fabricate SnS-SnO2 heterostructure with excellent photoresponse and charge transport properties: efficient photocatalyst for fast photoreduction of Cr(VI), Mater. Sci. Engi. B 275 (2022) 115520.
[25] L. Wang, N. Wang, L. Zhu, H. Yu, H. Tang, Photocatalytic reduction of Cr(VI) over different TiO2 photocatalysts and the effects of dissolved organic species, J. Hazard. Mater. 152 (2008) 93–99.
[26] H. Shen, F. Fu, W. Xue, X. Yang, S. Ajmal, Y. Zhen, L. Guo, D. Wang, R. Chi, In situ fabrication of Bi2MoO6/Bi2MoO6-x homojunction photocatalyst for simultaneous photocatalytic phenol degradation and Cr(VI) reduction, J. Colloid. Interface Sci. 599 (2021) 741–751.
[27] H. Li, F. Deng, Y. Zheng, L. Hua, C. Qu, X. Luo, Visible-lightdriven Z-scheme rGO/Bi2S3–BiOBr heterojunctions with tunable exposed BiOBr(102) facets for efficient synchronous photocatalytic degradation of 2-nitrophenol and Cr(VI) reduction, Environ. Sci. Nano 6 (2019) 3670–3683.
[28] B. Yan, J. Peng, F. Deng, L. Liu, X. Li, P. Shao, J. Zou, S. Zhang, J. Wang, X. Luo, Novel ZnFe2O4/Bi2S3 high-low junctions for boosting tetracycline degradation and Cr(VI) reduction, Chem. Eng. J. 452 (2023) 139353.

جامعة الجوف
Jouf University

Aljouf – SAKAKA 2014 – KSA
Tel.: 046252271 – Fax: 046247183
email: AJBSE@ju.edu.sa
Website: http://vrgs.ju.edu.sa/jer.aspx
https://www.ju.edu.sa/en/jouf-university-science-and-engineering-journal-jusej/home/